DEVELOPMENT AND IMPLEMENTATION OF A TESTING FACILITY FOR REAL-TIME HYBRID SIMULATION WITH A NONLINEAR SPECIMEN

by

Edwin Dielmig Patino Reyes

A Thesis

Submitted to the Faculty of Purdue University

In Partial Fulfillment of the Requirements for the degree of

Master of Science in Civil Engineering

Lyles School of Civil Engineering

West Lafayette, Indiana

December 2022

THE PURDUE UNIVERSITY GRADUATE SCHOOL
STATEMENT OF COMMITTEE APPROVAL

Dr. Shirley J. Dyke, Chair

Department of Mechanical Engineering and Lyles School of Civil Engineering

Dr. Julio A. Ramirez

Lyles School of Civil Engineering

Dr. Arun Prakash

Lyles School of Civil Engineering

Approved by:

Dr. Dulcy Abraham

To my family and friends.

ACKNOWLEDGMENTS

First, I would like to thank Dr. Shirley Dyke for welcoming me as part of her research group and for her guidance, invaluable support, and encouragement throughout my research. I want to thank Dr. Julio Ramirez and Dr. Arun Prakash for serving as my committee members and for their support throughout my graduate studies.

I want to thank Ingrid Elizabeth Madera and Manuel Alejandro Rojas for their guidance, invaluable knowledge, and judgment in developing this project. I want to especially thank my research colleague Manuel Iván Salmerón Becerra, whose experience, knowledge, and support were essential pillars throughout all stages of the project. I want to thank Johnny Condori Uribe and the entire RTHS team at the IISL for their knowledge and support during this project.

I want to express my gratitude towards my family and friends who always believed in me and always provided their guidance and support. In addition, I would like to thank everyone at the Lyles School of Civil Engineering, Research Machining Services, and Bowen Laboratory for their invaluable assistance whenever I required it.

I want to acknowledge the funding received by the National Science Foundation grant number NSF-1661621, the Multi-Hazard Engineering Collaboratory for Hybrid Simulation (MECHS), and the National Secretariat of Science, Technology, and Innovation of the Republic of Panama (SENACYT) for their support and funding in the development of this project.

TABLE OF CONTENTS

LIST OF TABLES

LIST OF FIGURES

ABSTRACT

Real-time hybrid simulation (RTHS) has demonstrated certain advantages over conventional large-scale testing. In an RTHS, the system that is under study is partitioned into a numerical and a physical substructure, where the numerical part is comprised of those elements that are easier to model mathematically, while the physical part consists of those that present a complex behavior difficult to capture in a numerical model. The most complex part of this study is the isolation system, a technology used to protect structures against earthquakes by modifying how they respond to ground motions. Unbonded Fiber Reinforced Elastomeric Isolators (UFREIs) are devices that can accomplish this task and have gained attention in recent years because of their modest but valuable features that make them suitable for implementation in low-rise buildings and in developing countries because of their low cost. Our end goal for this work is to enable the testing of scaled versions of these elastomeric isolators to understand their behavior under shear tests and realistic loading.

A testing instrument was designed and constructed to apply a uniaxial compressive force up to 22kN and a shear force of 8kN simultaneously to the specimens. A testing program was conducted where four primary sources of signal distortion were identified as caused by the servo-hydraulic system. From these results, a mechanics-based model was developed to understand better the dynamics that the sliding table can introduce to the measured signals accounting for inertial and dissipative forces. Two Bouc-Wen models were implemented to simulate the behavior of the UFREIs. The first only accounts for the hysteretic behavior of the isolator, and the second accounts for the additional nonlinearities found in the isolator's behavior. These models were assembled in a virtual RTHS which is available to users interested in learning the applications of RTHS of a base-isolated structure with a nonlinear component.

An RTHS experiment was conducted in the IISL where the control system comprised a delay compensator and a proportional-integral controller, which exhibited a good tracking performance with minimal delay and low RMSE. However, it can increase the distortion of the oil-column resonance in the measured signals. The simulation captures the behavior of the isolated structure for small displacements. However, it underestimates the displacement of the full-scale specimen for large displacements. The RTHS showed a better approximation of the displacement of the full-scale structure than the theoretical behavior approximated by the Bouc-Wen models.

1. INTRODUCTION

Hybrid simulations performed in real-time has shown to offer certain advantages over conventional large-scale testing. In an RTHS, the system that is under study is broken into a numerical substructure and a physical substructure, where the numerical part is comprised of those elements that are easier to be modeled mathematically, while the physical part is comprised of those elements that present a complex behavior difficult to capture in a numerical model (Wang, Wang, Jin, Chi, & Zhang, 2011). Some of the advantages that this testing technology provides include being cost-effective since large resources are typically required for large-scale testing. Its versatility is a major advantage since both numerical and physical substructures can be modified with relative ease to test new configurations or modifications to the specimens. RTHS also allows capturing rate effects, inertial effects, and loading the specimens at rates equal to the generated velocities and accelerations during the tests. Also, it allows to perform tests at speeds faster than real-time if specimens of reduced size are tested since scaling laws need to be considered, especially those related to time (Schellenberg, Becker, & Mahin, 2017).

This work adopts a particular type of RTHS called hybrid shake table testing (Horiuchi, Inoue, & Konno, 2000). The same concepts from an RTHS are applied to a shake table, and in the case of a non-destructive test, the less understood portion of a system could be tested experimentally against different numerical substructures (Schellenberg, Becker, & Mahin, 2017). The less understood part in this study is the isolation system, which can comprise active damping technologies such as magnetorheological dampers (Rabiee & Chae, 2022) and hydraulic actuators (Asai, Chang, & Spencer, 2015); or passive systems such as triple friction pendulum bearings (Scheaua, 2020), which show a high loading rate dependency; bonded elastomeric isolators, which presents material nonlinearities; or unbonded rubber isolators which introduces a new geometric nonlinearity due to the variation in the effective area in contact during its deformation due to lateral displacements.

Since its development, researchers on RTHS have dedicated their efforts to counteract the time delay inherently present in these simulations and to generate integration routines that are well-suited for real-time applications (Chen & Ricles, 2008; Huang, Guo, Chen, & Chen, 2018). Delay compensation methods are required to correct the phase difference between the input and the output signals and that could be introduced by a the transfer, control or data acquisition systems

(Horiuchi T. , Inoue, Konno, & Namita, 1999). For a transfer system with a sliding table or similar, the control and correction of errors is more difficult because of the payload placed on the shake table during the experiment and more frictional resistance due to the railing system. Therefore, it is more difficult for these setups to achieve a good tracking of the inputs without any delay.

For slow loading rates, it is necessary that physical substructure do not present any load-rate-dependent behavior that are not compensated in the computational portion of the tests. The motion of the actuator should also be uninterrupted to avoid developing any static frictional resistance between the carriages and the rails and between the actuator rod and seals (Schellenberg, Becker, & Mahin, 2017).

For rapid loading rates, it is important that the inertial forces generated both from the test specimen and the transfer system, which is in motion during the RTHS and is not part of the physical test specimen, are accurately accounted for during the design of the physical part of the experiment. This way the measurements from the load cells are free from these dynamics and can represent the true response of the test specimen. If they are not accounted for, they will need to be compensated in the computational portion of the simulation with filters or estimators. Some of these distortions could be due to the inertial forces from a sliding table that holds the specimens or force feedback from large dynamic actuators, especially if large and heavy setups are involved (Schellenberg, Becker, & Mahin, 2017).

Major research efforts have been devoted to implement different configurations of the sliding seismic tables. Some of these, place a sliding table on top of a seismic isolation system along with a vertical force to simulate the effect of a seismic load and the compressive load of the building, respectively. Some have placed a shake table on top of a physical substructure to simulate numerically the top portion of a building and study its effect on its physical portion below (Schellenberg, Becker, & Mahin, 2017). Others have combined a sliding table with dynamic actuators to simulate the interaction between a physical portion of a building with numerical substructures placed above and below the specimen (Eem, Jung, & Koo, 2013).

A seismic isolation bearing is a protective device that is typically installed between the building structure and foundation, although it can also be installed at mid-height or in other parts of the structure. This isolation is done to suppress the propagation of high-frequency seismic waves to the building, this occurs since they increase the flexibility of the structure, therefore, increasing its natural period (Cheng, 2008; Warn & Ryan, 2012). These isolators aid in seismic energy

dissipation by concentrating the relative displacements (between the ground motion and the response of the structure on top of the isolation layer) in the isolation system, thus enhancing the dynamic behavior of the structure and aiding in reducing the relative deformations and damage of structural elements. (Al-Anany, Moustafa, & Tait, 2018).

Mid-level isolation has been implemented over the last decade thanks to its potential in reducing structural demands and construction costs, and the flexibility that it provides to buildings that have transitions in them, such as multi-use buildings or when new stories are added to an existing structure without increasing seismic load. Studies of midlevel isolation focus on the interaction between the superstructure, the substructure, and the isolation system. Therefore, testing of multiple configurations of these structures it would be ideal to understand these interactions (Schellenberg, Becker, & Mahin, 2017; Zhang, Phillips, Taniguchi, Ikenaga, & Ikago, 2017).

Base isolation of a structure is a technology that is commonly used to protect it against earthquakes by modifying the way it vibrates or responds to a ground motion (Mitu, Sireteanu, & Daniel, 2010). One type of device that is used to achieve this base isolation are elastomeric isolators. However, before they are ready to be installed under a building, they need to undergo a series of testing to make sure that their design is appropriate for the building and that it effectively modifies its response to ground motions in the way that it is expected.

Unbonded Fiber Reinforced Elastomeric Isolators (UFREIs) has gained attention in recent years since they possess modest but valuable features that make them suitable for implementation in low-rise buildings and developing countries due to their low cost (Habieb, Milani, Tavio, & Milani, 2017) when compared with other types of isolators, such as bonded isolators, lead-core isolators, or steel-reinforced rubber isolators (Toopchi-Nezhad, Tait, & Drysdale, 2009). Some of their key advantages are their lower manufacturing cost and their simple implementation on the construction site. One of the reasons behind the lower cost of these isolators is the substitution of the steel layers for carbon or polyester fibers. Much research attention is now being focused on the fabrication of these isolators with different types of rubber or rubber-like materials, such as recycled rubber from tires or natural rubber (Calabrese, Spizzuoco, Serino, Della Corte, & Maddaloni, 2015). One of the features that this work focuses on is their unbonded nature since they are not fixed either to the superstructure or foundation. This feature introduces a new contact nonlinearity that the bonded case lack, hence the interest in running this type of isolator through a

real-time hybrid simulation which makes it possible to try different types of superstructures and test different isolators in a more versatile way. This could enable researchers to further their investigations into these types of isolation technologies, reducing the cost and resources.

These unbonded isolators could be implemented on low-rise masonry buildings since they could increase the period of the structure and allow for moderate horizontal deformations during an earthquake, while reducing the relative deformation between structural members and damage to non-structural elements in the superstructure. However, they are not suited for high-rise construction due to the large deformations generated in these scenarios by the superstructure alone, which can induce other structural issues such as moat impact for base isolated buildings.

One possibility to test the behavior of these isolators, under similar conditions that they would experience when they are placed under a building; is to build a real or, most likely, scaled version of the building and install an isolation layer under the structure, and send a ground motion signal to the shake table and capture the isolator response. Losanno et al, built a single-story frame on a shake table and performed a series of tests to understand the behavior of the isolators (Losanno, Sierra, Spizzuoco, Marulanda, & Thomson, 2020). This type of testing, however, is time-consuming since it involves a lot of planning, preparation, and construction, and it is also costly since we would need a facility that big and a lot of materials to build that experimental setup. If we test with standard methods, it becomes impractical and expensive. That's where hybrid simulation becomes an efficient solution for this task.

Since we are only interested in the behavior of the isolators, our objective in this scenario would be to build a smaller test setup, namely a transfer system, capable of applying on the isolator the same loading that it would experience under the structure, that way the isolator would respond accordingly. Here we wouldn't need to build a full-scale test specimen to have a good approximation of the behavior of the isolator. The dynamic behavior of the frame could be approximated by mass-damper-spring models with the same properties of a full-scale specimen.

One of the first steps taken to create this hybrid simulation is to define a numerical, a physical substructure, and a transfer system. In this case, the entire frame can become the numerical substructure, which could be modeled in software such as OpenSees, MATLAB, Simulink, Python, etc. The test specimen will become the physical substructure. And the transfer system should be designed to apply the same type of loading to the isolator as if it was being loaded by the full-scale specimen. In the case of isolator bearings, the transfer system should be able to apply a constant

vertical load on top of the specimen that comes from the superstructure and a horizontal displacement to simulate the relative motion that occurs between the superstructure and its foundation. Therefore, when we impose a ground motion to the RTHS system, the numerical substructure is going to displace and send this displacement to the transfer system, which will transmit this displacement to the physical specimen, which will respond with a restoring force that is sent back to the numerical substructure to compute the next iteration.

Our end goal for this complete work is to be able to test scaled versions of these elastomeric isolators to understand their behavior and learn the considerations when implementing a real-time hybrid simulation of this type. To this end a series of specific objectives are listed to meet the end goals, including to:

1) Design and develop a testing instrument that allows for simultaneous shear and uniaxial compressive testing of elastomeric isolator prototypes.
2) Collect data from isolator prototypes test and determine their elastic and dissipative properties from their hysteretic behavior.
3) Contribute experimental data from the isolator prototypes to the RTHS community in order to assess the tracking control of a real-time hybrid simulation with these types of nonlinear specimens.
4) Develop a real-time hybrid test that aims to emulate a full-scale physical experiment to test the feasibility of building a full-scale testing structure versus the advantages of an RTHS experiment.
5) Construct a virtual model of the RTHS experiment to facilitate the implementation of different controlling systems before deploying them in the laboratory.
6) Compare the results between a theoretical behavior of the isolators, the experimental results obtained in the laboratory, and the results from a full-scale testing structure.

2. DESCRIPTION OF THE RTHS ARCHITECTURE

This chapter is devoted to describing the architecture of the structural system being studied. Section 2.1 explains the assumptions adopted and the equations of motions of the numerical substructure. Section 2.2, explains the process of partitioning and the considerations taken to ensure that the partition is stable enough to be implemented in an RTHS. Section 2.3 describes the physical substructure and Section 2.4 describes the experimental setup constructed for this experiment.

2.1 Model definition

A case study of a planar structural frame of three stories and one bay is presented in this section to formulate the equations that were used in the substructuring process. A frame with 18 degrees of freedom (DOF), as shown in Figure 2.1a, is rigidly fixed to the ground. Thus, several assumptions can be made to reduce the total number of degrees of freedom in the model. These assumptions also aid in making the substructuring process more straightforward, reducing the complexity of the problem, making the model easier to implement in a real-time testing scenario, and avoiding any instabilities that additional degrees of freedom with small inertia could introduce in the system. The structure is idealized as a shear building. The additional assumptions adopted are listed below:

1) The motion of a 3D frame structure is analyzed as a planar frame in one direction.
2) Masses are assumed to be lumped in the middle of the spans, discretizing the degrees of freedom of the structure.
3) Beams are assumed to be infinitely rigid, relative to that of the columns, and both ends of the beams are attached to a rigid diaphragm, i.e., they remain horizontal during motion. They do not experience shortening or elongation and the connections between beams and columns are fixed against rotation.
4) Columns are assumed to be axially stiff, therefore the vertical translations of all nodes are neglected, making the deformation of the model independent of the axial forces present in the columns.

5) Rocking motion is assumed to be much smaller than the horizontal motion due to the vertical-to-horizontal stiffness design ratios of the isolators (Losanno, Sierra, Spizzuoco, Marulanda, & Thomson, 2020). Therefore, it is neglected.
6) The displacement of the upper face of the isolator is assumed to be equal to the displacement of the bottom face of the base slab, thus relative slipping at this interface is neglected.

After applying these assumptions, a planar three-story building of 18-DOFs can be modeled dynamically as a three-degrees-of-freedom system as shown in Figure 2.1b. The equations of motion that describe the dynamics of the system are:

$$\begin{aligned} M_1\ddot{u}_1 + C_1(\dot{u}_1 - \dot{x}_g) + C_2(\dot{u}_1 - \dot{u}_2) + K_1(u_1 - x_g) + K_2(u_1 - u_2) = 0 \\ M_2\ddot{u}_2 + C_2(\dot{u}_2 - \dot{u}_1) + C_3(\dot{u}_2 - \dot{u}_3) + K_2(u_2 - u_1) + K_3(u_2 - u_3) = 0 \\ M_3\ddot{u}_3 + C_3(\dot{u}_3 - \dot{u}_2) + K_3(u_3 - u_2) = 0 \end{aligned} \tag{2.1}$$

where, M_i, K_i, C_i denote the mass, damping, and stiffness values for each degree of freedom (at each floor), respectively (Chen, Dong, Chen, & Nakata, 2020). The vectors $\ddot{u}_i$, $\dot{u}_i$ and u_i correspond to the absolute acceleration, absolute velocity, and absolute displacement of each story, respectively. The variables $\dot{x}_g$ and x_g are the ground velocity and ground displacements, respectively. By expressing the motion described in Equation (2.1) relative to the ground and arranging it into a matrix notation we get:

$$[M]\{\ddot{x}_i\} + [C]\{\dot{x}_i\} + [K]\{x_i\} = -[M]\{I\}\{\ddot{x}_g\}. \tag{2.2}$$

The vectors $\ddot{x}_i$, $\dot{x}_i$ and x_i correspond to the acceleration, velocity and displacement of each story relative to the ground, respectively. The vector *I* is a column vector of ones and $\ddot{x}_g$ is the ground acceleration disturbance to the structure.

The matrices in Equation (2.2) can then be arranged to include more levels above the base slab:

$$\begin{aligned} &\begin{bmatrix} M_1 & 0 \\ 0 & M_s \end{bmatrix}\begin{Bmatrix} \ddot{x}_1 \\ \ddot{x}_s \end{Bmatrix} + \begin{bmatrix} C_1 + \{I\}^T[C_s]\{I\} & -\{I\}^T[C_s] \\ -[C_s]\{I\} & C_s \end{bmatrix}\begin{Bmatrix} \dot{x}_1 \\ \dot{x}_s \end{Bmatrix} \\ &\qquad + \begin{bmatrix} K_1 + \{I\}^T[K_s]\{I\} & -\{I\}^T[K_s] \\ -[K_s]\{I\} & K_s \end{bmatrix}\begin{Bmatrix} x_1 \\ x_s \end{Bmatrix} = -\begin{bmatrix} M_1 & 0 \\ 0 & M_s \end{bmatrix}\{I\} \cdot \ddot{x} \end{aligned} \tag{2.3}$$

where:

$$M_s = \begin{bmatrix} M_2 & 0 \\ 0 & M_3 \end{bmatrix},\ C_s = \begin{bmatrix} C_2 + C_3 & -C_3 \\ -C_3 & C_3 \end{bmatrix} \text{ and } K_s = \begin{bmatrix} K_2 + K_3 & -K_3 \\ -K_3 & K_3 \end{bmatrix}. \quad (2.4)$$

The subscript $[\dots]_1$ indicates the DOF that corresponds to the base slab and the subscript $[\dots]_s$ indicates the parameters that correspond to the superstructure above the base slab as if it were rigidly fixed to the ground, as shown in Equation (2.4).

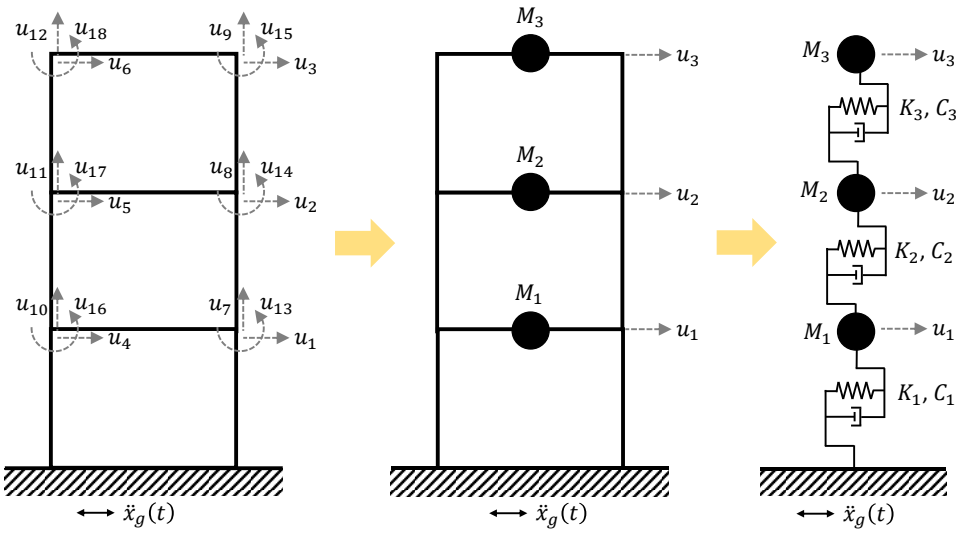

Figure 2.1. a) 18-DOFs planar three-story building (left), b) Lumped mass system (center), and c) 3-DOFs model (right).

For the present experiment, a 2-DOF system was chosen for the reference model. Therefore, the superstructure will be a single-degree-of-freedom spring-mass-damper system. Hence, the matrices in Equation (2.4) reduce to: $M_s = M_2$, $C_s = C_2$, and $K_s = K_2$. The values for these parameters are listed in Table 2.1 and correspond to the ones identified experimentally for the same type of frame built at the University of Naples Federico II (Magliulo, et al., 2012). The parameter C_2 is assumed to be equal to: $2\zeta\omega M_2$, where ζ is the damping ratio identified for the natural vibration mode of the superstructure and equal to 1%; ω is the natural frequency in radians per second, when considering the superstructure as a fixed-base structure; and M_2 is the mass of the top slab of the structure. A modal analysis was also performed to the superstructure system and its natural frequency was found to be 3.81 Hz.

Table 2.1. Values for the dynamic parameters of the SDOF.

$M_1(kg)$	$M_2(kg)$	$K_2(N/m)$	$C_2(N \cdot s/m)$	$f_n(Hz)$	n_i (isolators)
3570	4155	2.38×10^6	1.99×10^3	3.81	4

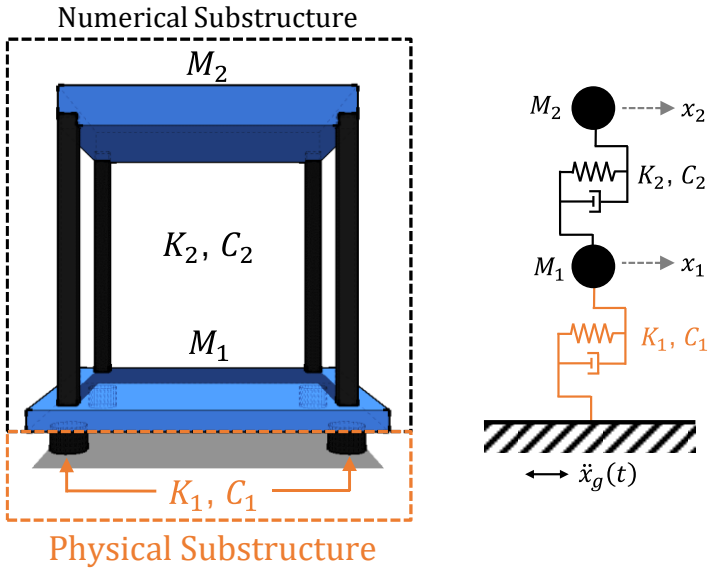

Figure 2.2. a) Schematic of the experimental 3D frame (left) and b) 2-DOF reference model considered for the hybrid simulation (right).

2.1.1 Numerical substructuring

The next step is the substructuring process, where we will classify each component of Equation (2.3) into three components: numerical, transfer system, and physical or experimental. An RTHS is developed from the assumption that the mathematical formulation of the response of the reference model to an excitation (given by Equation (2.2) and shown in Figure 2.1c), can be represented as the sum of a numerical and an experimental part as shown in Equation (2.5), where the subscripts $[\dots]_n$ and $[\dots]_e$ represent a numerical and experimental component, respectively. It is important to note that the whole mass of the base slab will be considered as a numerical component, thus, there will be no experimental contribution to the inertial force of the system represented in these following equations:

$$[M_n + M_e]\{\ddot{x}_i\} + [C_n + C_e]\{\dot{x}_i\} + [K_n + K_e]\{x_i\} = -[M_n + M_e]\{\Gamma\}\{\ddot{x}_g\} \tag{2.5}$$

Equation (2.5) simplifies into Equation (2.6), where the subscript $[\dots]_r$ represents a reference model component. The experimental contribution that will act on the numerical system is given by $f_e(t)$ and has been moved to the right-hand side of the equation.

$$[M_r]\{\ddot{x}_i\} + [C_n]\{\dot{x}_i\} + [K_n]\{x_i\} = -[M_r]\{\Gamma\}\{\ddot{x}_g\} - \underbrace{([K_e]\{x_i\} + [C_e]\{\dot{x}_i\})}_{f_e(t)} \tag{2.6}$$

If we compare Equation (2.6) against Figure 2.2b it is evident that the experimental components in our system correspond to only K_1 and C_1 and that the contribution of the isolation layer to the system is given by:

$$f_e(t) = K_1 x_1 + C_1 \dot{x}_1 \tag{2.7}$$

where, K_1 and C_1 are the linear elastic and dissipative force contributions from the isolation layer to the first degree of freedom of the system, x_1. Assuming that $f_e(t)$ is the contribution of just one isolator, we can arrange Equation (2.6) for a 2-DOF system as:

$$[M_r]\{\ddot{x}_i\} + [C_n]\{\dot{x}_i\} + [K_n]\{x_i\} = -[M_r]\{\Gamma\}\{\ddot{x}_g\} - n_i\{\gamma\} f_e(t) \tag{2.8}$$

with:

$$M_r = \begin{bmatrix} M_1 & 0 \\ 0 & M_2 \end{bmatrix},\ C_n = \begin{bmatrix} C_2 & -C_2 \\ -C_2 & C_2 \end{bmatrix} \text{ and } K_n = \begin{bmatrix} K_2 & -K_2 \\ -K_2 & K_2 \end{bmatrix} \tag{2.9}$$

where, n_i is the number of isolators in the isolation layer (as given in Table 2.1); Γ is an influence vector that describes the inertial effects of the excitation on the masses of the system, in our case, this is a column vector with a value of one for each row element corresponding to any mass in the system that develops an inertial effect due to ground acceleration; and the vector, γ is a column vector which elements take a value of one at the degree of freedom where the experimental restoring force is acting, *i.e.*, $\gamma = [1, 0]^T$.

The reference model can be represented in a state-space notation as:

$$\begin{aligned} \dot{z} &= A \cdot z + B \cdot F(t) \\ y &= C \cdot z + D \cdot F(t). \end{aligned} \tag{2.10}$$

The matrices A, B, C, and D are given by:

$$A = \begin{bmatrix} \mathbb{O}_{2\times2} & \mathbb{I}_{2\times2} \\ -M_r^{-1}K_n & -M_r^{-1}C_n \end{bmatrix} \quad B = \begin{bmatrix} \mathbb{O}_{2\times1} & \mathbb{O}_{2\times1} \\ -\Gamma & -M_r^{-1}\gamma \end{bmatrix}$$
$$C = \begin{bmatrix} \mathbb{I}_{2\times2} & \mathbb{O}_{2\times2} \\ \mathbb{O}_{2\times2} & \mathbb{I}_{2\times2} \\ -M_r^{-1}K_n & -M_r^{-1}C_n \end{bmatrix} \quad D = \begin{bmatrix} \mathbb{O}_{2\times1} & \mathbb{O}_{2\times1} \\ \mathbb{O}_{2\times1} & \mathbb{O}_{2\times1} \\ -\Gamma & -M_r^{-1}\gamma \end{bmatrix} \tag{2.11}$$

where, $\mathbb{O}_{n\times m}$ and $\mathbb{I}_{n\times n}$ denote a zero and identity matrices, respectively. The state vector, z, is defined by the position (x_i) and velocity ($\dot{x}_i$) of the system; the output vector, y, will be comprised of the position (x_i), velocity ($\dot{x}_i$), and acceleration ($\ddot{x}_i$) of the system. The input vector, $F(t)$, is given by the ground acceleration, $\ddot{x}_g(t)$, and the experimental restoring force, $f_e(t)$. Symbolically:

$$\dot{z} = \begin{bmatrix} \dot{x} \\ \ddot{x} \end{bmatrix}, \quad z = \begin{bmatrix} x \\ \dot{x} \end{bmatrix}, \quad y = \begin{bmatrix} x \\ \dot{x} \\ \ddot{x} \end{bmatrix}, \quad F(t) = \begin{bmatrix} \ddot{x}_g(t) \\ f_e(t) \end{bmatrix}. \tag{2.12}$$

The restoring force from the isolation layer in the reference model, $f_e(t)$, shows hysteretic behavior because of the nature of the isolator, hence, it can be modeled through multiple methods that exist in literature. It is important to note that this force acts instantaneously on the numerical structure as it would in a real-world scenario. The integration of the differential equations of the numerical substructure, in their state-space form, is done using an implicit extrapolation numerical integration algorithm (ode14x), through a Simulink model with a fixed time step of $1/4096\ sec$.

2.2 Partitioning

The partitioning of the system is stated implicitly in Section 2.1.1, where the numerical and experimental components of the system have been separated. The stability and feasibility of other partitioning options should be thoroughly investigated before their implementation a simulation or at the testing setup. In this section, we will describe the partitioned simulation model and address some of the considerations that were taken to ensure the stability of the partitioned system and its integration with the transfer system.

2.2.1 Hybrid system definition

In a RTHS, the restoring force will originate in the experimental substructure, *i.e.*, the isolators. In our simulation, it is assumed that the response of one single isolator will be the same as that of all isolators in the isolation layer, as given in Equation (2.8).

After the system has been partitioned, the ground motion, $\ddot{x}_g$, enters the numerical substructure as shown in Figure 2.3 and Figure 2.4, where the target (or desired) base slab displacement relative to the ground, $x_n^{(1)}$, is computed. This relative displacement enters the control system where the commanded displacement, x_c, is calculated to compensate for the inherent dynamics of the transfer system and enforce the desired numerical displacement of the base slab.

The control plant (which is formed of the transfer system coupled with the experimental substructure, *i.e.*, the isolator) reacts to the commanded displacement and the sliding table experiences a displacement, x_m, which is measured by the actuator's integrated linear variable differential transformer (LVDT) transducer. In the control plant, a reaction force is also generated and measured by the load transducer, which is fed back to the numerical substructure as an input, along with the ground motion at the next integration time step to generate the subsequent desired displacement. The measured displacement of the sliding table is also fed back to the control system to calculate the commanded displacement for the next time step.

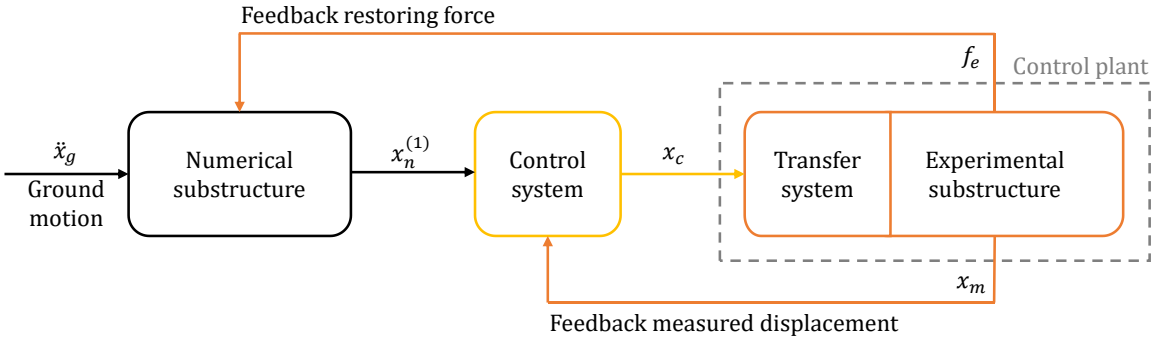

Figure 2.3. Flow-diagram of the RTHS system.

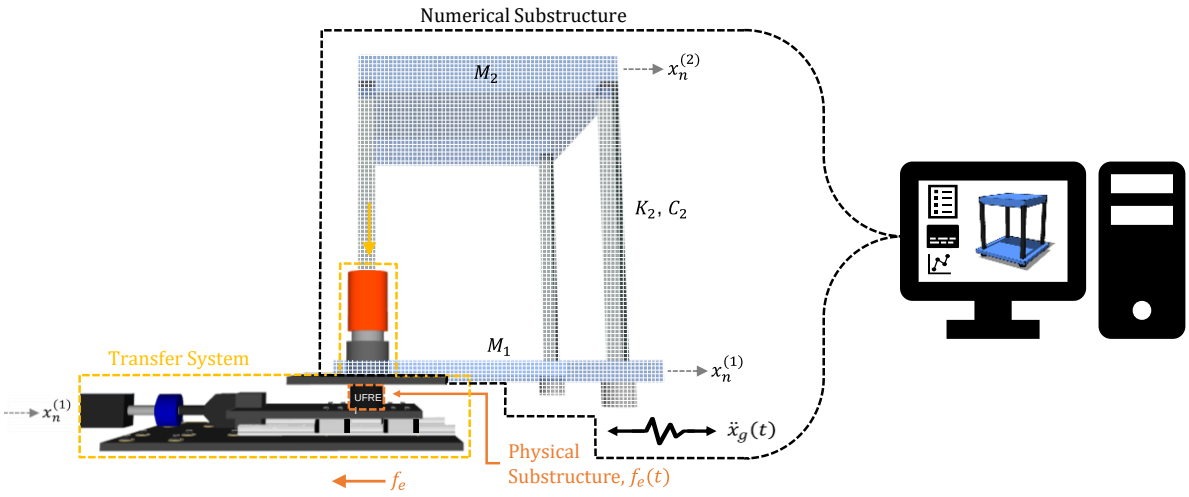

Figure 2.4. Schematic of the RTHS system and its elements.

2.2.2 Considerations for stability

Some considerations were taken to ensure the stability of the partitioning choice, as described next:

1) As mentioned in Section 2.1.1, for this partitioning case, the mass of the base slab will be considered as a numerical component. Therefore, the physical mass of the sliding table will not be included in the reference equations of motion, Equations (2.8) and (2.9). This means that there will be no experimental contribution to the inertial force of the reference structure. In the same way, the damping generated by the friction in the bearings of the sliding table will not be included as part of the reference substructure. Therefore, the experimental dissipative contribution will come only from the damping of the isolators and there will be no experimental dissipative contribution from the damping of the sliding table bearings to the reference structure.

2) To ensure that [K] and [C] in Equation (2.9) are well-conditioned matrices and avoid any related instabilities we assume a small linear contribution given by the term: $k_1 x_1$, which can be assumed as an initial stiffness that acts on the system of equations (2.8) in the form: $n_i k_1 x_1$. The same can be assumed for a small linear damping contribution, $n_i c_1 \dot{x}_1$:

$$K_n = \begin{bmatrix} n_i k_1 x_1 + K_2 & -K_2 \\ -K_2 & K_2 \end{bmatrix} \text{ and } C_n = \begin{bmatrix} n_i c_1 \dot{x}_1 + C_2 & -C_2 \\ -C_2 & C_2 \end{bmatrix}. \quad (2.13)$$

These contributions must be added as well to the right-hand side of Equation (2.8), specifically to the restoring force measured from the isolators. This equation will then become:

$$[M_r]\{\ddot{x}_i\} + [C_n]\{\dot{x}_i\} + [K_n]\{x_i\} = -[M_r]\{\Gamma\}\{\ddot{x}_g\} - n_i\{\gamma\}(f_e(t) - k_1 x_1 - c_1 \dot{x}_1) \quad (2.14)$$

It is worth noting that since these contributions are being added on both sides of Equation (2.8), the actual values of coefficients k_1 and c_1 can be set arbitrarily as long as their order of magnitude is consistent with the other parameters in the system. In this experiment they are taken as the average stiffness and effective viscous damping that were found through experimental testing.

3) A lag in the application of the experimental restoring force is known to cause an increase in the displacement of the overall system due to the effective negative damping it introduces (Horiuchi, Inoue, Konno, & Namita, 1999). For this reason, a stability analysis was done to determine the amount of lag that would make the partitioned system either change from a stable to an unstable state, or exceed the stroke limit of the sliding table, whichever case occurs first.

   For this analysis, a pure time delay was introduced between the superstructure and the isolation layer, as shown in Figure 2.5, and was increased until either of the previously discussed limits were met. This amount of delay is referred to as a critical time delay (Maghareh, Dyke, Rabieniaharatbar, & Prakash, 2017).

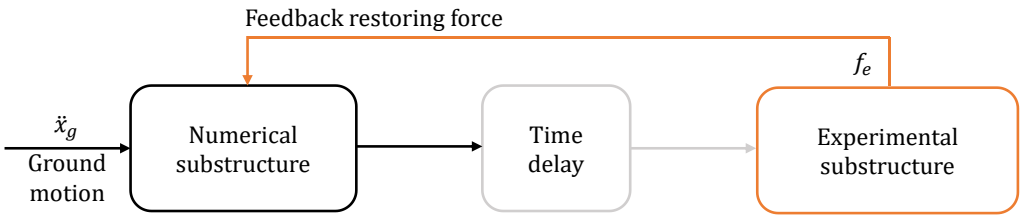

Figure 2.5. Introduction of a fictitious delay to the partitioned system for stability analysis.

A ±50% variation of the mass, stiffness, and damping of the numerical substructure (from those shown in Table 2.1) was also introduced as an additional parameter in the analysis to determine the sensitivity in the critical time delay. Each parameter was varied individually, and the other parameters remained constant, while the amount of delay in the system was increased. Figure 2.6 shows the critical time delay variation as a function of M_1, M_2, K_2 and ζ, respectively. The analysis shows that, for a system with the parameters given in Table 2.1, the critical time delay is 35 ms, which is greater than the experimental delay identified in the laboratory for the sliding table.

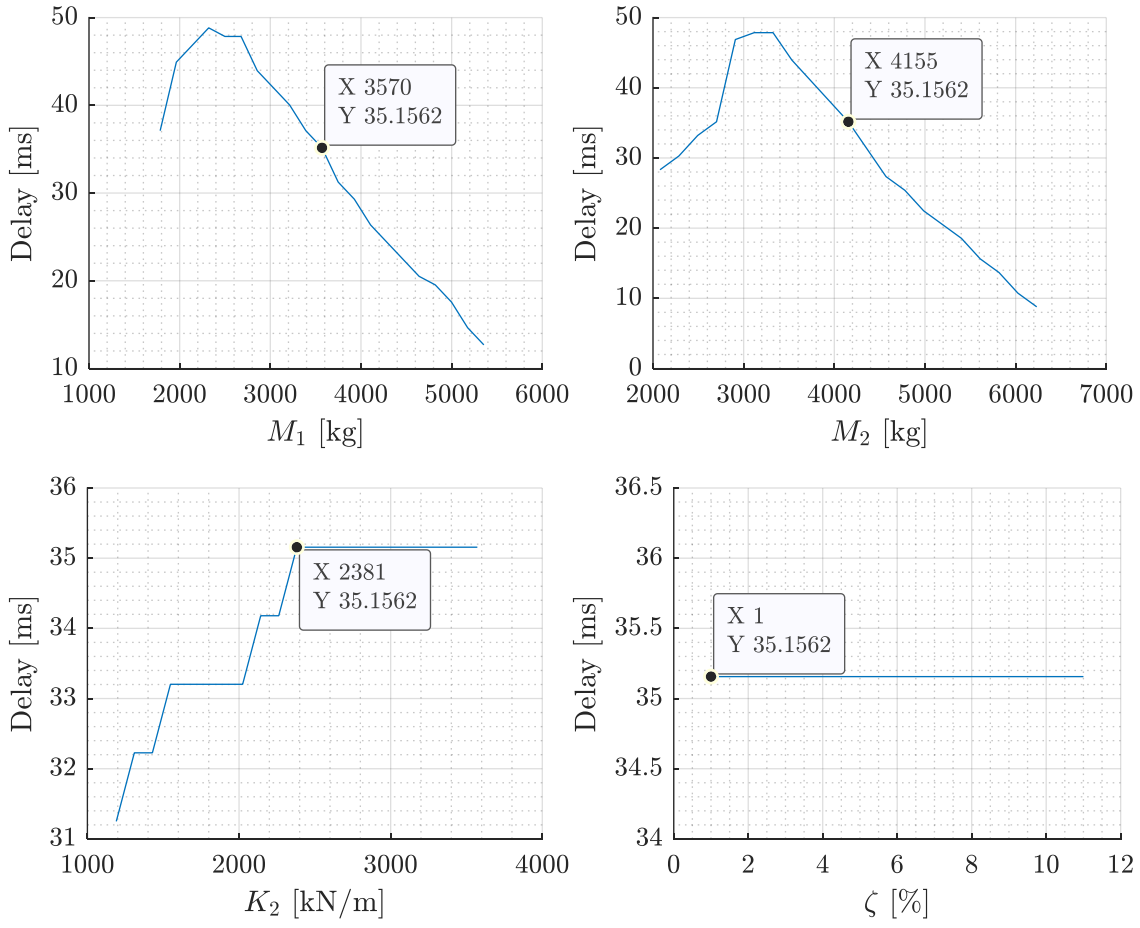

Figure 2.6. Variation of the critical time delay as a function of M_1 (top-left), M_2 (top-right), K_2 (bottom-left), and ζ (bottom-right).

Figure 2.6 shows that the system stability is affected primarily by the mass of each degree of freedom, such that an increase in the stiffness of the superstructure causes an increase in the critical time delay; and an increase in the damping ratio of the superstructure does not seem to have a significant effect on the critical delay of the system. The effect of the variation of K_2 and ζ on the system could be attributed to the system becoming more rigid and exhibiting rigid body motion, which is a desirable effect in a base-isolated system. On the other hand, the variation of M_1 or M_2 could drive the system to an unstable state since by increasing the masses, greater displacements are going to take place due to an increase in the inertial restoring forces.

2.3 Physical substructure

Unbonded fiber-reinforced elastomeric isolators were selected as the physical substructure that will form the isolation layer. This family of isolators is made from an elastomeric material and a material that serves as a reinforcement. In earlier years, rubber was selected as the elastomeric material, and thin sheets of steel formed the reinforcement. This reinforcement was necessary to keep the rubber from bulging radially while a compressive force was acting on it. The manufacturing cost of these isolators tends to be high due to the steel reinforcement and the top and bottom steel plates that were attached to the top and bottom faces of the isolator to transmit the load between the superstructures. Over the years, different types of geometry and materials have been tested with the objective of reducing manufacturing costs and bringing them closer to an application in residential and midlevel constructions. In recent years, researchers have focused their attention on unbonded isolators, which eliminate the need for the top and bottom plates; different types of fibers such as carbon, polyester, and flax fibers; and other sources for the rubber matrix, such as recycled rubber from discarded tires.

The range of specimens that were part of the study can be classified into three large groups: unbonded carbon-fiber reinforced natural rubber isolators (NC), unbonded polyester-fiber reinforced natural rubber isolators (NP), and unbonded polyester fiber reinforced recycled rubber isolators (RP), a cross-sectional view of the carbon and polyester fiber reinforced isolators is shown in Figure 2.7. The polyester-fiber reinforced isolators further classify into different batches. The qualitative differences between these batches are given in Table 2.2 and were provided by the manufacturing entities.

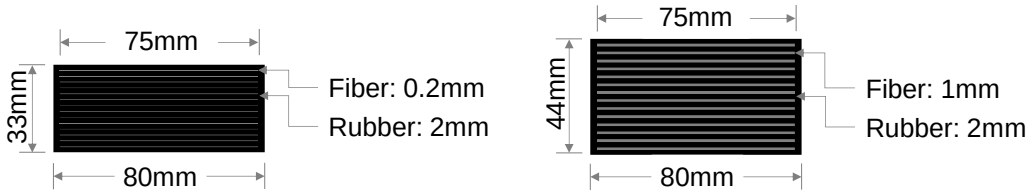

Figure 2.7. Cross section of the a) carbon (left) and b) polyester (right) fiber reinforced isolators.

A portion of these isolators was previously experimentally tested in Italy under bidirectional seismic excitation (Losanno, Sierra, Spizzuoco, Marulanda, & Thomson, 2019). The excitation was sent to a base-isolated one-story steel frame that was built for this purpose. The base-isolated frame was mounted on a sliding table and vertical and horizontal displacements, and accelerations were measured to obtain the forces generated during the experiment. These isolators were first tested under compressive, and shear loading applied simultaneously to assess their elastic and dissipative properties and compare them to the ones obtained from the full-scale test (Losanno, Sierra, Spizzuoco, Marulanda, & Thomson, 2020).

Table 2.2. Subclassification of the polyester-fiber reinforced isolators.

Type of rubber	Batch label	Description
Natural	A	This batch was previously tested in Italy.
	B	This batch had the same type of mixture of Natural rubber Batch A, but it had not been tested previous to this work.
Recycled	A	Mixture containing more coarse rubber aggregate. The mixture was done with a good manufacturing process. This batch was previously tested in Italy.
	B	This mixture had a balanced proportioning of coarse and fine rubber aggregates, but were created following a poor manufacturing process.
	C	This third batch was manufactured with a balanced proportioning of coarse and fine rubber aggregates and with a good manufacturing process.

The testing procedure starts with the preloading of the isolators with a compressive vertical force of 19kN the isolator is then subjected to a displacement protocol required by ASCE 7-16 SEC. 17.8.2.2-2.a. which is shown in Figure 2.8. The effective lateral stiffness, K_h, was calculated for each isolator based on the peak values of force and displacement values for each hysteretic loop, symbolically:

$$K_h = \frac{F_{max} - F_{min}}{D_{max} - D_{min}} \tag{2.15}$$

here, F_{max} and D_{max} represents the maximum force and displacement reached in each deformation cycle. In the same way, F_{min} and D_{min} are the minimum force and displacement reached in the cycle. The effective viscous damping ratio is calculated as the dissipated area, E_D, from each deformation cycle divided by the effective lateral stiffness and the maximum displacement, symbolically:

$$\beta = \frac{E_D}{2\pi K_h D_{max}^2} \tag{2.16}$$

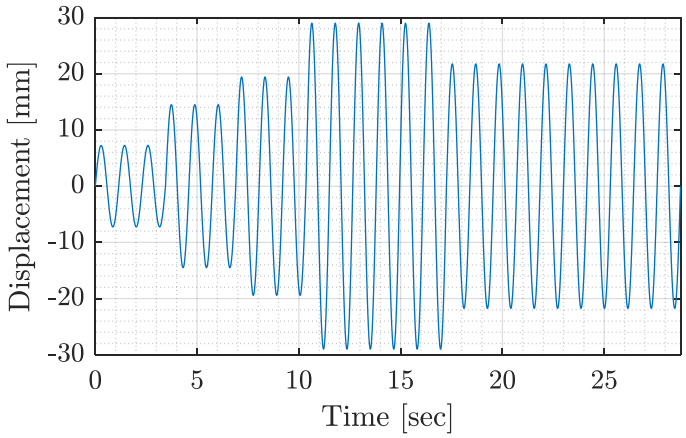

Figure 2.8. ASCE 7-16 displacement protocol used for the shear tests.

The batch label is added to the group label (NC, NP, RP) to form the name of the isolator, after the batch label a number was added at the end to keep track of each isolator that belongs to each group and/or batch. Figures 2.9 through 2.14 shows the hysteretic behavior of the three main isolator groups.

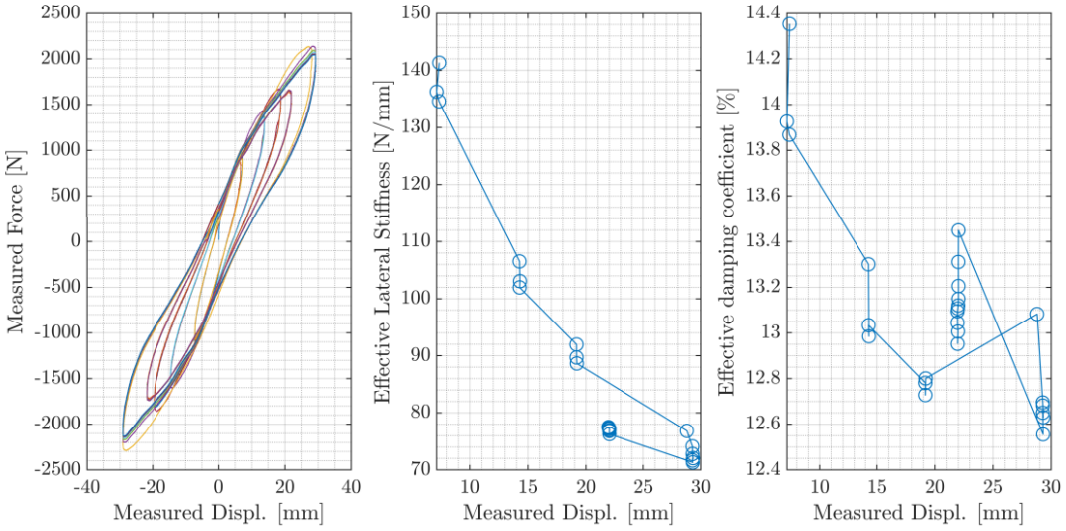

Figure 2.9. a) Hysteretic behavior of the carbon-fiber reinforced natural-rubber isolator (NCA1) (left) b) Effective lateral stiffness, K_h, as a function of displacement (center). c) Effective viscous damping, β, as a function of displacement (right).

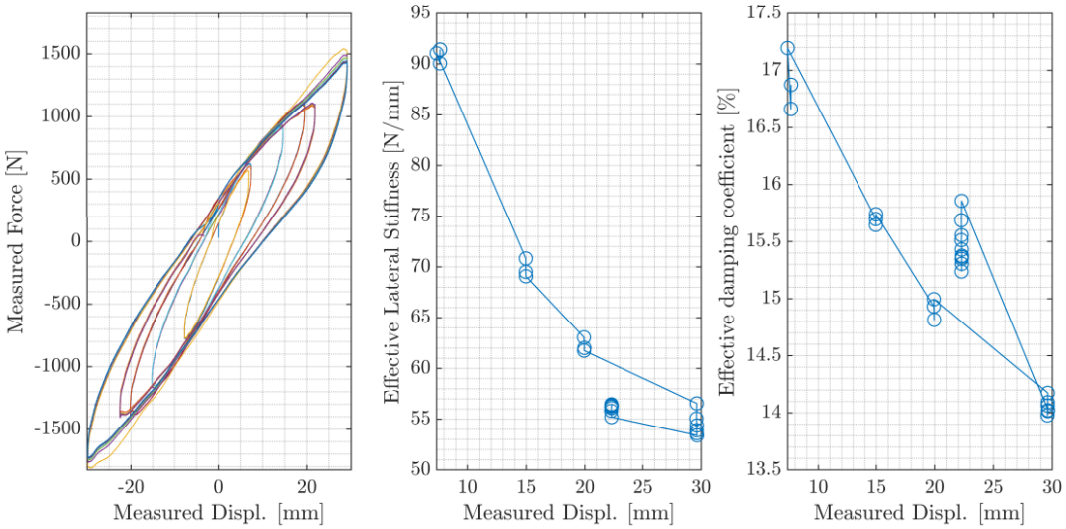

Figure 2.10. a) Hysteretic behavior of the polyester-fiber reinforced natural-rubber isolator batch A (NPA1) (left) b) Effective lateral stiffness, K_h, as a function of displacement (center). c) Effective viscous damping, β, as a function of displacement (right).

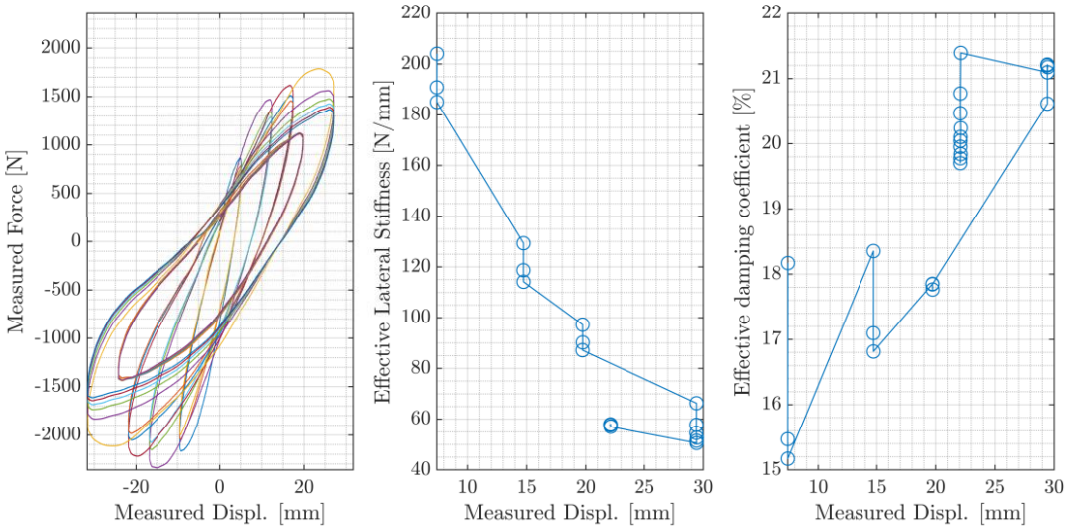

Figure 2.11. a) Hysteretic behavior of the polyester-fiber reinforced natural-rubber isolator batch B (NPB8) (left) b) Effective lateral stiffness, K_h, as a function of displacement (center). c) Effective viscous damping, β, as a function of displacement (right).

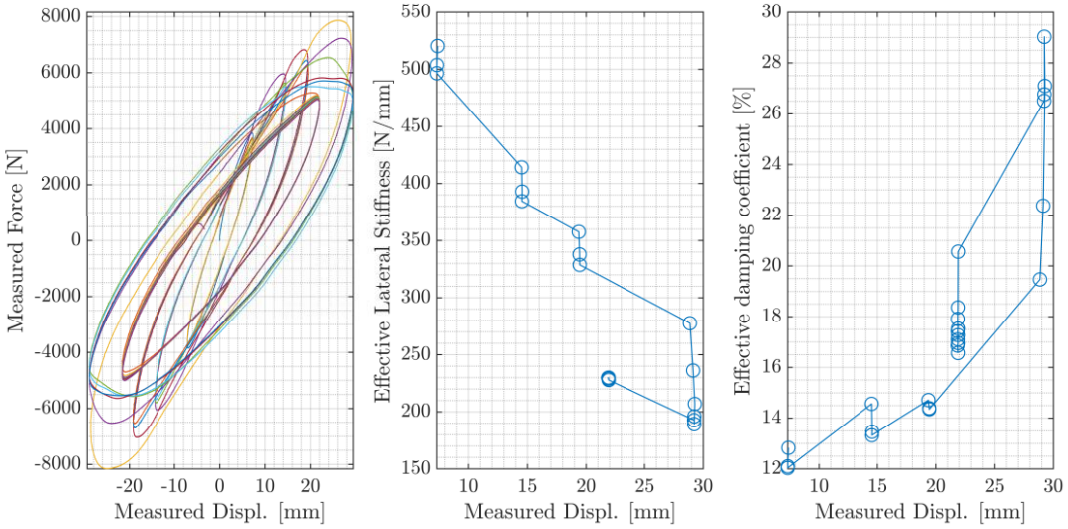

Figure 2.12. a) Hysteretic behavior of the polyester-fiber reinforced recycled-rubber isolator batch A (RPA1) (left) b) Effective lateral stiffness, K_h, as a function of displacement (center). c) Effective viscous damping, β, as a function of displacement (right).

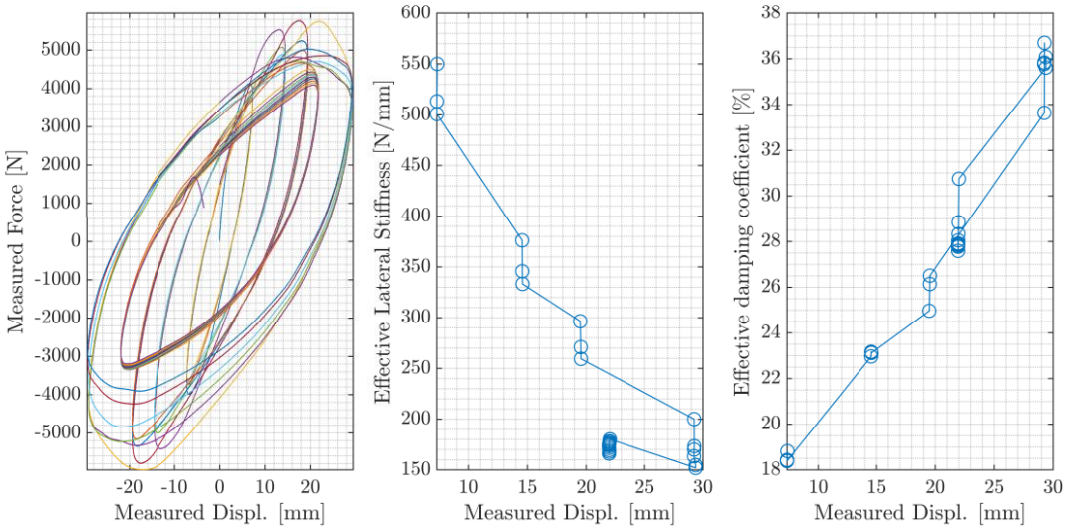

Figure 2.13. a) Hysteretic behavior of the polyester-fiber reinforced recycled-rubber isolator batch B (RPB2) (left) b) Effective lateral stiffness, K_h, as a function of displacement (center). c) Effective viscous damping, β, as a function of displacement (right).

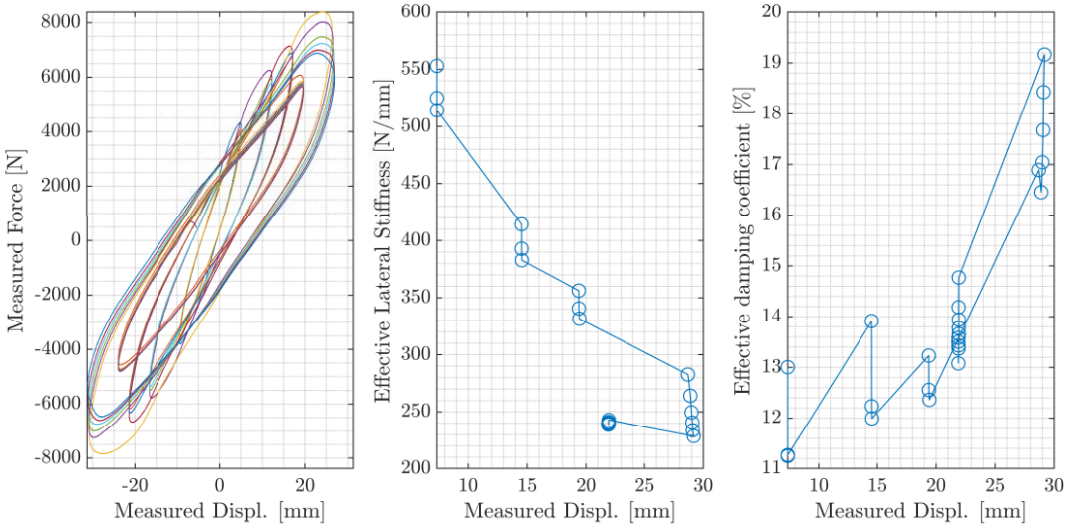

Figure 2.14. a) Hysteretic behavior of the polyester-fiber reinforced recycled-rubber isolator batch C (RPC9) (left) b) Effective lateral stiffness, K_h, as a function of displacement (center). c) Effective viscous damping, β, as a function of displacement (right).

Figures 2.9 through 2.14 shows that stiffness degradation was present in all hysteretic responses as the slope of the loops starts to decrease when the deformation increases. All isolators presented a softening and a hardening behavior at different intensity levels during the test. These effects are more noticeable in the case of the NCA isolators, presented in Figure 2.9, where a clear decrease in the instantaneous stiffness appears when the isolator has displaced 5 mm, followed by an increase when the isolator has displaced beyond 20 mm. This behavior is present also in the hysteretic responses of isolators NPA, NPB, and RPC, however, the decreases and increases of stiffness are subtler, particularly at greater amplitudes. We speculate that these softening and hardening behaviors produce a pinching effect near the origin, as shown in Figure 2.9 (Aloisio, Alaggio, Köhler, & Fragiacomo, 2020; Han, Dong, Du, Sun, & Huang, 2014; Pelliciari, et al., 2018), this effect is still present in Figure 2.10 for the NPA isolator, but are barely visible for the NPB isolators in Figure 2.11. This change in behavior is attributed to some change in the rubber mixture or in the manufacturing process. This change in the manufacturing process made the NPB isolators stiffer. This increase in rigidity made it difficult for the isolator to deform under the horizontal load and develop softening and hardening behaviors. The same is true for the RPC isolators in Figure 2.14, the most evident indicator of this loss of flexibility is due the fact that the isolators made with recycled rubber developed higher lateral forces when compared to the NCA or NPA isolators. Figures 2.12 through 2.14 exemplifies this effect, isolators RPA and RPB show to be more rigid than the RPC isolators in which some softening and hardening is seen even in the largest deformation cycles.

The variation in effective lateral stiffness of the NCA isolators is similar to that of the ones tested in Italy for the case of the natural rubber, which validates the implemented testing procedure. The isolators that were previously tested (e.g., NPA) have shown so far, an overall degradation in their effective horizontal stiffness, since the variation in horizontal stiffness is lower than the ones previously tested. The effective viscous damping obtained for all the tested isolators presented an increase with the lateral displacement, this being is the opposite for the isolators tested in Italy or for a set of aged isolators (Losanno, Sierra, Spizzuoco, Marulanda, & Thomson, 2019).

An average lateral stiffness was obtained for the isolator NPA1 from the shear tests with a value of 62.29 N/mm and an effective viscous damping ratio of 15%. These values, along with the two DOF system presented in Section 2.1, are used to perform a modal analysis and the natural frequencies were calculated to be $1.79\ Hz$ and $6.02\ Hz$ for the first and second mode, respectively.

The mode shapes are shown in Figure 2.15. Although this type of analysis is not applicable to these types of systems, since the damping of the system is non-classical due to the significant difference between the damping of the structure and the damping of the isolation layer, it is a tool that gives an idea of the magnitude of the frequencies that can be expected from the system.

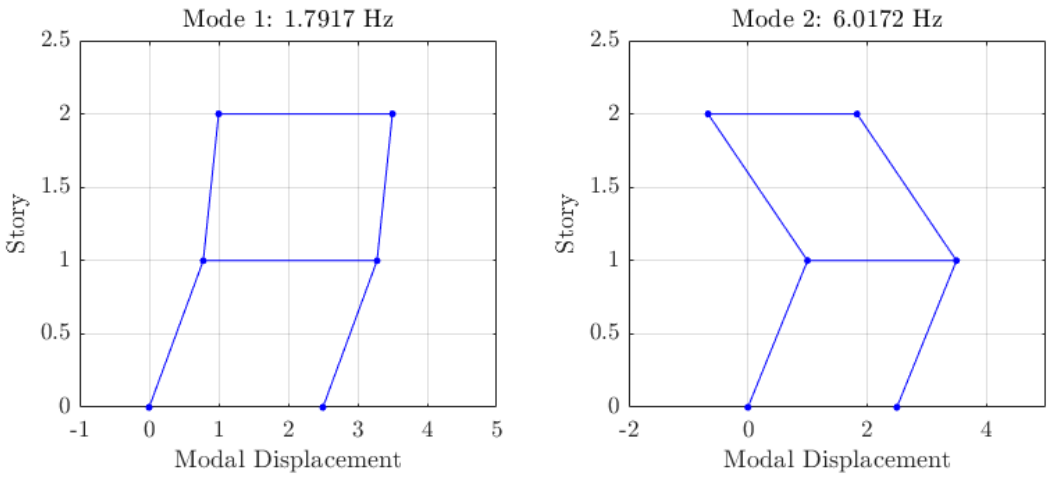

Figure 2.15. Stick figures of the approximate mode shapes of the isolated structure normalized at their maximum modal displacement.

2.4 Experimental setup

A new testing frame was recently built in the Intelligent Infrastructure Systems Laboratory (IISL) at Purdue University with the aim of testing small-scale structural specimens and including axial loading when necessary. This facility is a moment-resisting steel frame mounted on a concrete pad. It was designed to apply up to 22kN of compressive vertical force on a specimen to represent the weight of the superstructure inside the testing area through a hydraulic jack while the specimen is subjected to a variable horizontal force of ±8.8kN, applied by a hydraulic actuator as shown in Figure 2.16.

For this experiment, the specimens under study are fiber-reinforced elastomeric isolators which should be subjected to a constant vertical force and variable horizontal force. To achieve these conditions, one 609.6mm x 406.4mm x 19.05mm, hot-rolled low carbon steel plate is used to act as the vertical loading plane on top of the isolator; this loading is applied on the plate by a hydraulic jack, with a rated capacity of 294kN. The vertical loading is measured through a load

cell transducer with a rated capacity of 88.9kN placed between the top plate and the hydraulic jack. The vertical displacement of the top plate is measured by an LVDT transducer with a stroke of ±76.2mm.

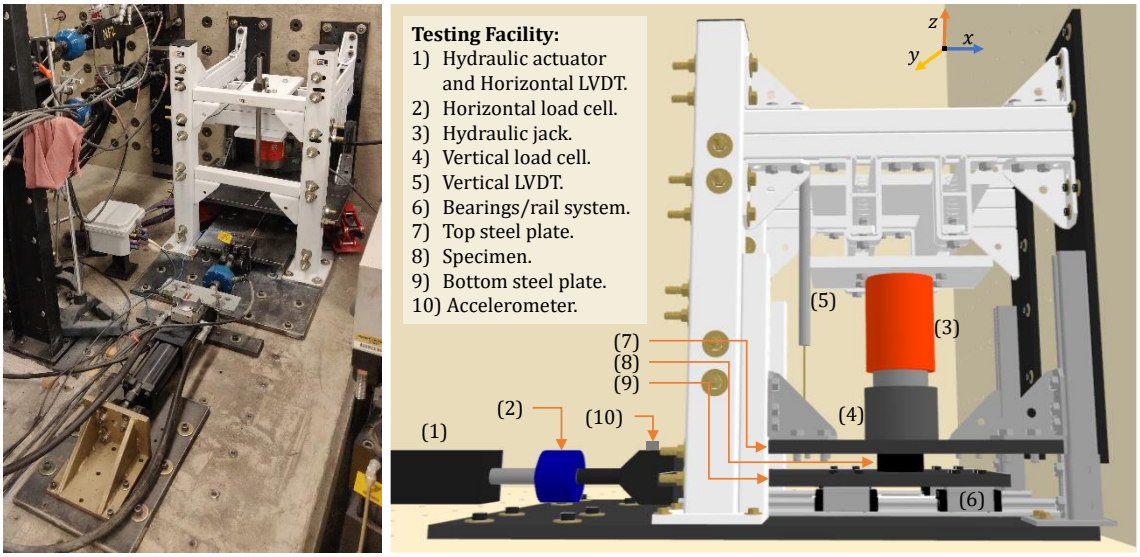

Figure 2.16. Testing facility at the IISL (left) and render of the facility listing its components (right).

A linear, double-ended servo-hydraulic actuator (Shore Western, 910D series) with a maximum rated force of 9.78kN and a stroke of ±60 mm, is used to apply the horizontal displacement on the specimen. Built into the actuator, an LVDT transducer measures the displacement of the actuator's rod. The actuator is connected to a second 558.8mm x 330.2mm x 19.05mm hot-rolled low carbon steel plate which is attached to four high-loading capacity ball bearing carriages sliding on low-friction linear guide rails. A low-profile load cell (Interface, 1000 series) with a maximum rated force of 11.1kN is connected between the actuator and the steel plate to provide the horizontal force measurement of the sliding table. Finally, a piezoelectric accelerometer is used to capture the acceleration signal of the sliding table in the direction of motion.

A 5 mm by 5 mm grid pattern was imprinted on the top and bottom steel plates to improve the contact friction between the plates and the isolators. This was required specifically for the more rigid isolators made from recycled rubber which lacked the proper grip that the isolators made from natural rubber had.

2.4.1 Modal analysis and signal distortions

A set of tests were performed to obtain modal information from the new testing facility. Four piezoelectric accelerometers were used as part of the instrumentation to obtain the acceleration data from the tests. The location of the accelerometers is shown in Figure 2.17. One accelerometer was located on each column at 16 inches from their base to capture the horizontal motion of the frame along the direction of the sliding table motion. One accelerometer was located on the right column at 30 inches from its base to measure the lateral motion of the frame perpendicular to the motion of the sliding table. The last accelerometer was located 5 inches from the edge of the top loading plate towards its center to measure the vertical motion that it experiences during the test.

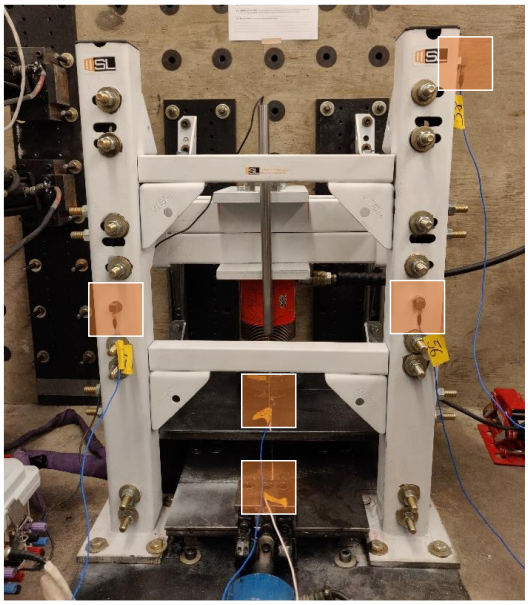

Figure 2.17. Location of the piezoelectric accelerometers during the modal identification tests.

A band-limited white noise (BLWN) signal was sent to the bare sliding table, and the Fast Fourier Transform was taken to obtain the frequency behavior of the frame. The spectra for the vertical motion of the top plate and the horizontal and lateral motion of the columns are shown in Figure 2.18. The spectra for the left and right columns appear to contain a similar frequency content with three prominent peaks at 129.6 Hz, 168.1 Hz, and 210.7 Hz, which could be associated with the horizontal motion of the frame. However, the 129.6 Hz appeared with a larger magnitude in the lateral motion spectrum of the right column suggesting that this peak could correspond to a lateral mode of the frame. The vertical motion spectrum of the top plate shows peaks with a larger

spectral density at 55 Hz, 94 Hz, and 110.8 Hz that are attributed to the vertical motion of the plate during the tests since they only were captured by the accelerometer located on top.

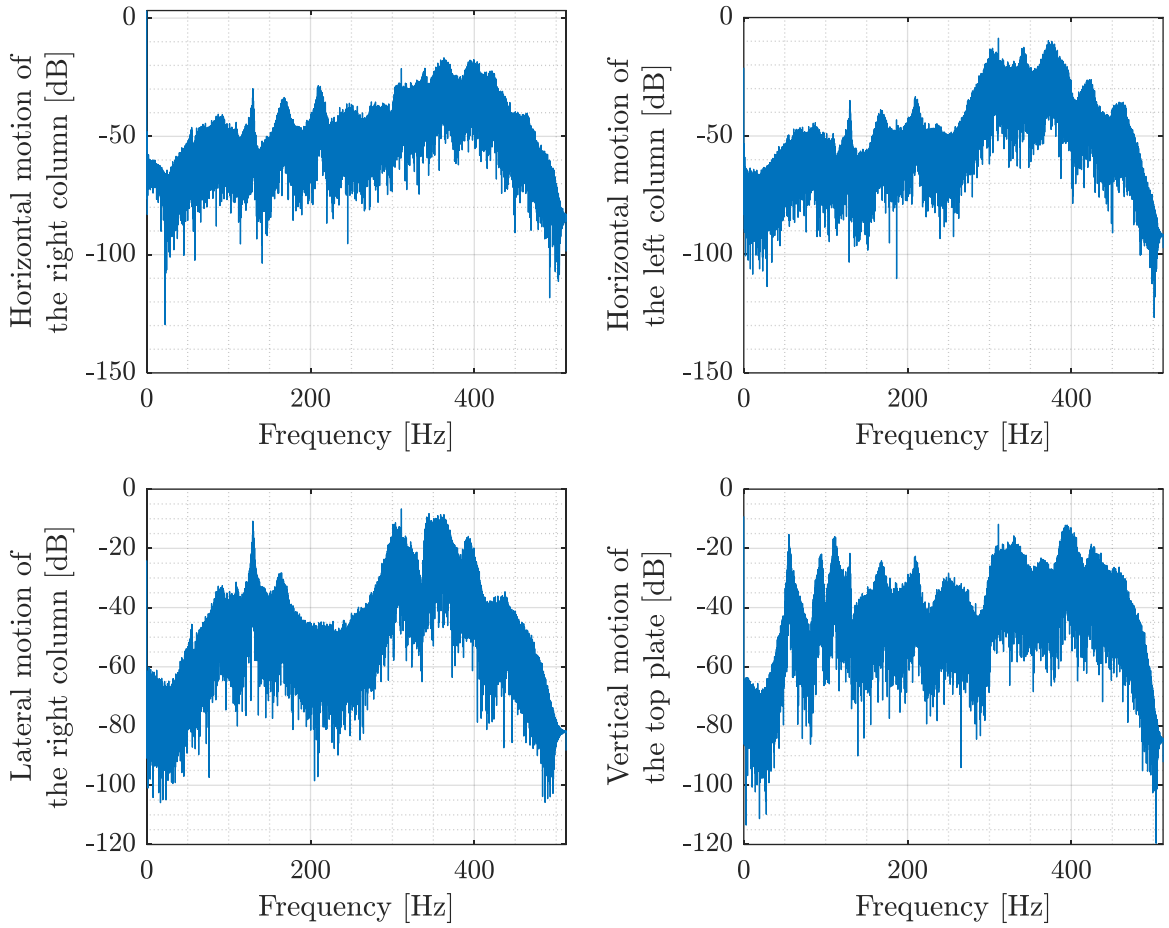

Figure 2.18. Spectrum showing the magnitude of a) the horizontal motion of the right column (top-left), b) the horizontal motion of the left column (top-right), c) the lateral motion of the right column (bottom- left), and d) the vertical motion of the top plate (bottom-right).

For lower frequency ranges, up to 40 Hz, there does not seem to be any mode that can be attributed to the motion of the frame. Some peaks could be identified at 12 Hz, 24 Hz, and 40 Hz with very small magnitudes relative to the ones described previously, but they are presumed to come from the servo-hydraulic system. In summary, the response spectrum shows that high-frequency content related to the motion of the setup is found above 50 Hz. Therefore, it is concluded that there is no significant frequency content due to the frame motion that could contaminate the low-frequency range of interest (up to 40 Hz).

The accelerometer attached to the sliding table, as shown in Figure 2.16, was used to capture the acceleration signal of the sliding table itself.

Two major causes of signal distortion, introduced by the sliding table, were observed in the response spectra obtained for open loop sinusoidal and BLWN input signals. The first type of distortion identified was a high-frequency component in the horizontal motion response when the table was both loaded and unloaded, occurring between around 50 Hz to 90 Hz. This distortion corresponds to the oil-column resonance effect and is shown in Figure 2.19a.

The oil-column inside an actuator can act as a spring that reacts to the mass of the sliding table, forming a mass-spring system. The frequency of this system is termed the oil-column resonant frequency (Qian, Ou, Maghareh, & Dyke, 2014) and was identified in our transfer system by sending a BLWN signal to the unloaded sliding table and estimating a transfer function between the desired displacement signal as the input and the measured force of the actuator as the output (Ozcelik, Conte, & Luco, 2021). Figure 2.19a shows an increase in gain around 71Hz, which corresponds to the oil-column resonant frequency.

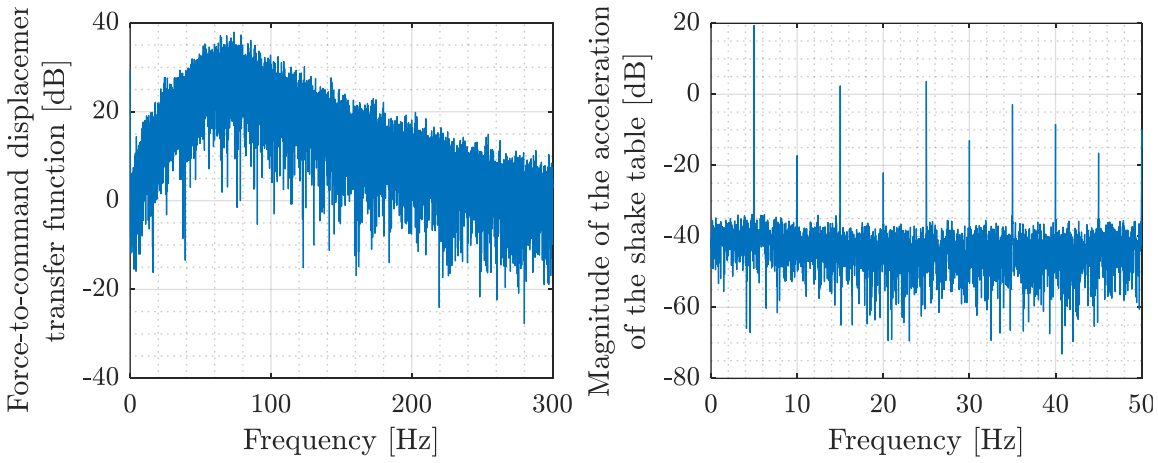

Figure 2.19. a) Estimated force-to-command displacement transfer function (left) and b) harmonic distortions (right)

When the sliding table was tested without any specimen, the second type of distortion was more evident under a sine wave input signal: even and odd harmonics of the exciting frequency were present in the measured signals, as shown in Figure 2.19b. These distortions can be attributed to the nonlinearities present in the servo-hydraulic system, such as a nonlinear flow-pressure relationship or a flow-gain nonlinearity (Ozcelik, Conte, & Luco, 2021).

Between these two types of signal distortions identified, the oil-column resonance has a greater influence on the real-time hybrid simulation; since it is fed back to the numerical substructure, its effect slips into the displacement signal that is sent to the actuator where it is amplified. The harmonic distortions are more noticeable in open loop tests and when the input signal is periodic in nature (Airouche, Aknouche, Bechtoula, Mezouer, & Kibboua, 2018; Yao, Hu, Fu, & Han, 2011).

3. EXPERIMENTAL CHARACTRIZATION AND MODELING OF THE SLIDING TABLE MECHANICAL SYSTEM

This chapter explains the mechanical model of the sliding table to have a better understating of the dynamics present in the system by means of analyzing the hysteresis curves for the displacement, velocity, and acceleration signals. The mechanical model formulated to simulate the behavior of the experimental setup is described in Section 3.2, while Section 3.3 presents the procedure followed for identification.

3.1 Testing program

A set of signals were sent to the bare sliding table to obtain enough observations to perform the subsequent identification analysis. The selection of the input signals in the program was based on the assumed range of amplitudes (up to 50 mm) and frequencies (up to 40Hz) that the sliding table is expected to be subjected to throughout the different tests. The signals measured for each of the tests are displacement of the sliding table, acceleration of the sliding table, and force exerted by the actuator. The list of signals is shown in Table 3.1.

Table 3.1. Signals that were part of the testing program.

Signal type	**Code**	**Max. abs. Displ. [mm]**	**Max. abs. Accel. [m/s^2]**	**Max. abs. Force [N]**	**Max. frequency [Hz]**	**Duration [s]**	**Displ. Standard dev. [mm]**
BLWN	WN1	12.28	197.05	13179.53	-	30.00	49.96
BLWN	WN2	0.22	2.60	30.59	-	30.00	5.00
BLWN	WN3	1.64	192.13	5369.53	-	30.00	5.00
BLWN	WN4	1.80	197.04	6012.20	-	120.00	5.00
BLWN	WN5	3.87	198.22	10071.72	-	120.00	10.01
CHIRP	CH1	10.28	166.73	10600.44	39.50	120.00	-
CHIRP	CH2	10.26	166.98	10498.05	39.50	120.00	-
CHIRP	CH3	10.26	165.96	10618.74	39.50	120.00	-
CHIRP	CH4	10.31	174.11	10460.78	39.50	120.00	-
SINE	SN1	9.25	1.99	209.15	0.25	60.00	-
SINE	SN2	9.37	5.20	212.04	0.25	60.00	-
SINE	SN3	10.37	4.74	198.12	0.25	60.00	-
SINE	SN4	45.83	11.47	484.99	0.25	60.00	-
SINE	SN5	40.81	14.47	525.74	0.25	60.00	-

Table 3.1. continued

Signal type	Code	Max. abs. Displ. [mm]	Max. abs. Accel. [m/s^2]	Max. abs. Force [N]	Max. frequency [Hz]	Duration [s]	Displ. Standard dev. [mm]
SINE	SN6	25.57	8.68	361.61	0.25	60.00	-
SINE	SN7	10.29	7.88	302.45	0.50	60.00	-
SINE	SN8	25.51	14.30	563.25	0.50	60.00	-
SINE	SN8	25.51	14.30	563.25	0.50	60.00	-
SINE	SN9	40.73	18.86	755.63	0.50	60.00	-
SINE	SN10	10.21	16.19	635.58	1.00	60.00	-
SINE	SN11	25.26	20.96	710.13	1.00	60.00	-
SINE	SN12	40.43	48.50	1128.69	1.00	60.00	-
SINE	SN13	9.65	23.58	998.80	3.00	60.00	-
SINE	SN14	24.25	141.09	2019.18	3.00	60.00	-
SINE	SN15	38.92	155.39	2751.61	3.00	60.00	-
SINE	SN16	9.14	33.60	1377.91	5.00	60.00	-
SINE	SN17	22.68	153.66	2871.04	5.00	60.00	-
SINE	SN18	7.67	68.94	2093.96	10.00	60.00	-
TRIANGULAR	TR1	10.18	4.75	207.13	0.25	60.00	-
TRIANGULAR	TR2	25.17	8.30	347.05	0.25	60.00	-
TRIANGULAR	TR3	40.18	9.98	447.18	0.25	60.00	-
TRIANGULAR	TR4	10.02	5.94	261.54	0.50	60.00	-
TRIANGULAR	TR5	24.79	8.89	363.59	0.50	60.00	-
TRIANGULAR	TR6	39.59	14.47	489.31	0.50	60.00	-
TRIANGULAR	TR7	9.73	7.41	329.94	1.00	60.00	-
TRIANGULAR	TR8	24.04	17.66	657.04	1.00	60.00	-
TRIANGULAR	TR9	38.65	40.10	1159.29	1.00	60.00	-
TRIANGULAR	TR10	8.68	35.88	713.88	3.00	60.00	-
TRIANGULAR	TR11	21.94	112.14	2469.22	3.00	60.00	-
TRIANGULAR	TR12	40.57	4.00	182.49	0.10	60.00	-
TRIANGULAR	TR13	10.27	3.64	160.08	0.10	60.00	-

3.2 Model formulation and characterization approach

The hysteresis curves for the measured displacement, calculated velocity, and measured acceleration were all plotted against the actuator's measured force and shown in Figure 3.1. These curves correspond to a 10 mm and 0.5 Hz sine wave that was sent to the sliding table as the input signal.

Figure 3.1a shows that there is a virtually constant opposing force when the plate is from the maximum to the minimum displacements with an approximate magnitude of 50 N. The possibility of relatively large elastic forces acting on the system is discarded since no relationship appears to

develop in either direction of motion. One particularity of this figure is the small bumps that appear when the plate is displacing around 5 mm, 0 mm, and -6 mm. The position at which these bumps occur varies depending on the amplitude of the exciting signal. These bumps are associated with the harmonic distortions that are present in the force measurement due to the nature of the input signal and the nonlinearities of the servo-hydraulic system since they disappear after the signal is filtered with a low-pass filter with a cut-off frequency close to the frequency of the input signal. Another feature of this curve are the relatively larger peaks when the actuator switches direction. These peaks are attributed to the friction coefficient changing at the beginning of each direction of motion from its static to its dynamic value (Ozcelik , 2008).

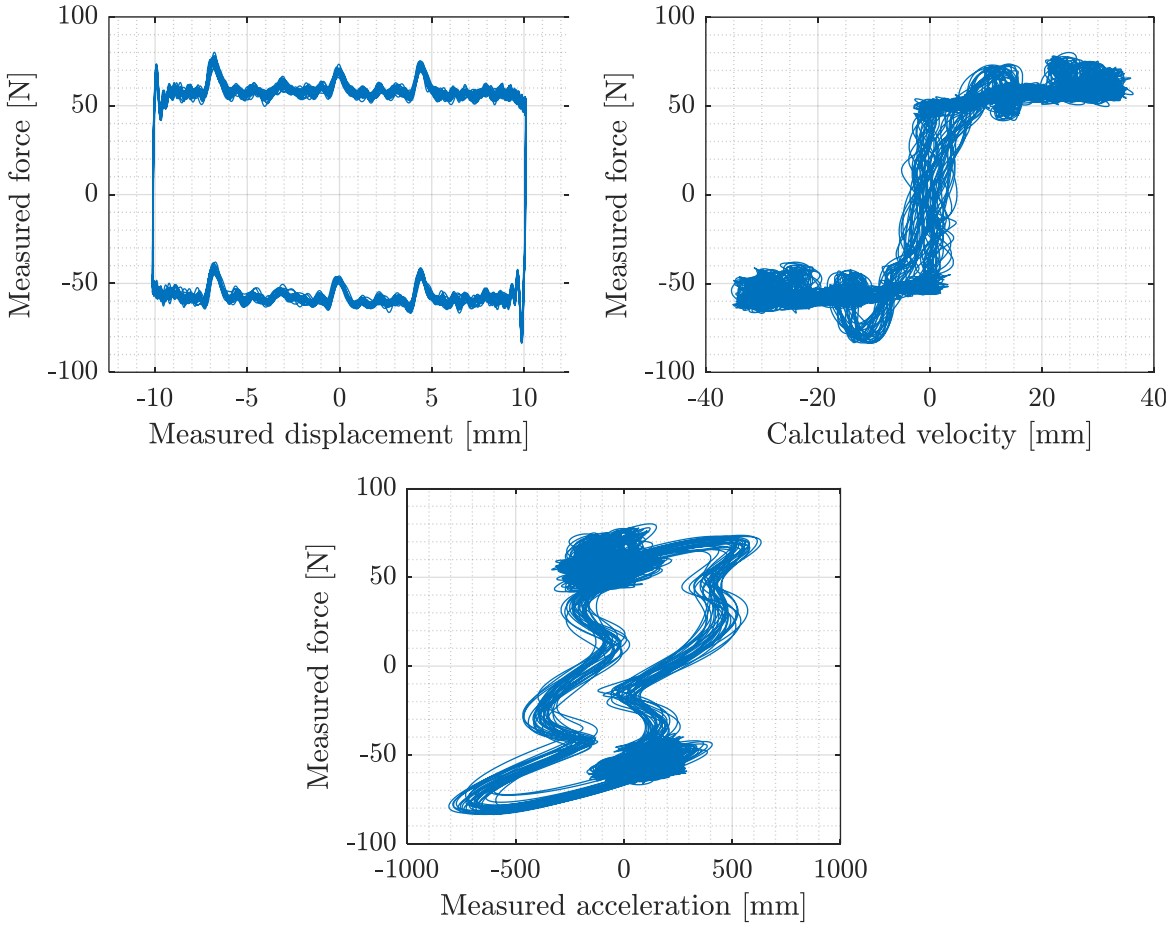

Figure 3.1. Hysteresis curves for a) actuator's measured force vs. measured displacement(top-left), b) measured force vs. computed velocity (top-right), and c) measured force vs. measured acceleration (bottom-center).

Figure 3.1b shows the relationship between the velocity (computed from the measured displacement) of the sliding table and the measured actuator's force. It can be considered as the result of two phases. The first relates to the overcoming of the Coulomb friction force by the actuator and occurs when the force raises to approximately 50 N in a very small time duration at the start of the motion. In the second phase, the relationship between the force and the velocity follows an approximately linear relationship and can be approximated as viscous damping.

The last hysteretic curve in Figure 3.1c shows how the measured force varies with the measured acceleration. For positive values of acceleration, there is a negative force that is almost constant at –50 N. For a negative acceleration, which corresponds to the moment when the plate is passing through the origin, there is a constant force of 50 N.

The previous analysis was carried out for different signals, and it was determined that the behavior is dependent on the frequency of the input signal. Figure 3.2a shows the variation of the actuator's force as a function of the measured displacement and the frequency of the input signal. A chirp with an amplitude of 10 mm and a frequency ranging from 0.001 Hz to 40 Hz was used as the input signal to generate this plot. The hysteretic curves corresponding to the selected chirp signal is shown in Figure 3.2.

Figure 3.2a shows that the measured force at low frequencies seems to be very small, and remain a constant value during the different direction of motion, as previously described in Figure 3.1a. The forces gradually increase with the increase of frequency, to depend almost linearly on the displacement. This dependency is associated with the increase of the inertial restoring force developed as the acceleration increases with frequency (Luco, Ozcelik, & Conte, 2010). Since the force plotted in Figure 3.2 are the total actuator force, the inertial effects are included in the hysteresis curve for displacement.

Figure 3.1c shows a more evident linear dependency between the force and the acceleration that occurs at higher frequencies, which is different from the one observed in Figure 3.1c when a low-frequency input signal was sent to the sliding table. The low-frequency input signals do not induce an acceleration greater enough for a significant inertial force to develop and appear as clearly as in Figure 3.2c. The nonlinearity observed in this curve is attributed to the damping in the system.

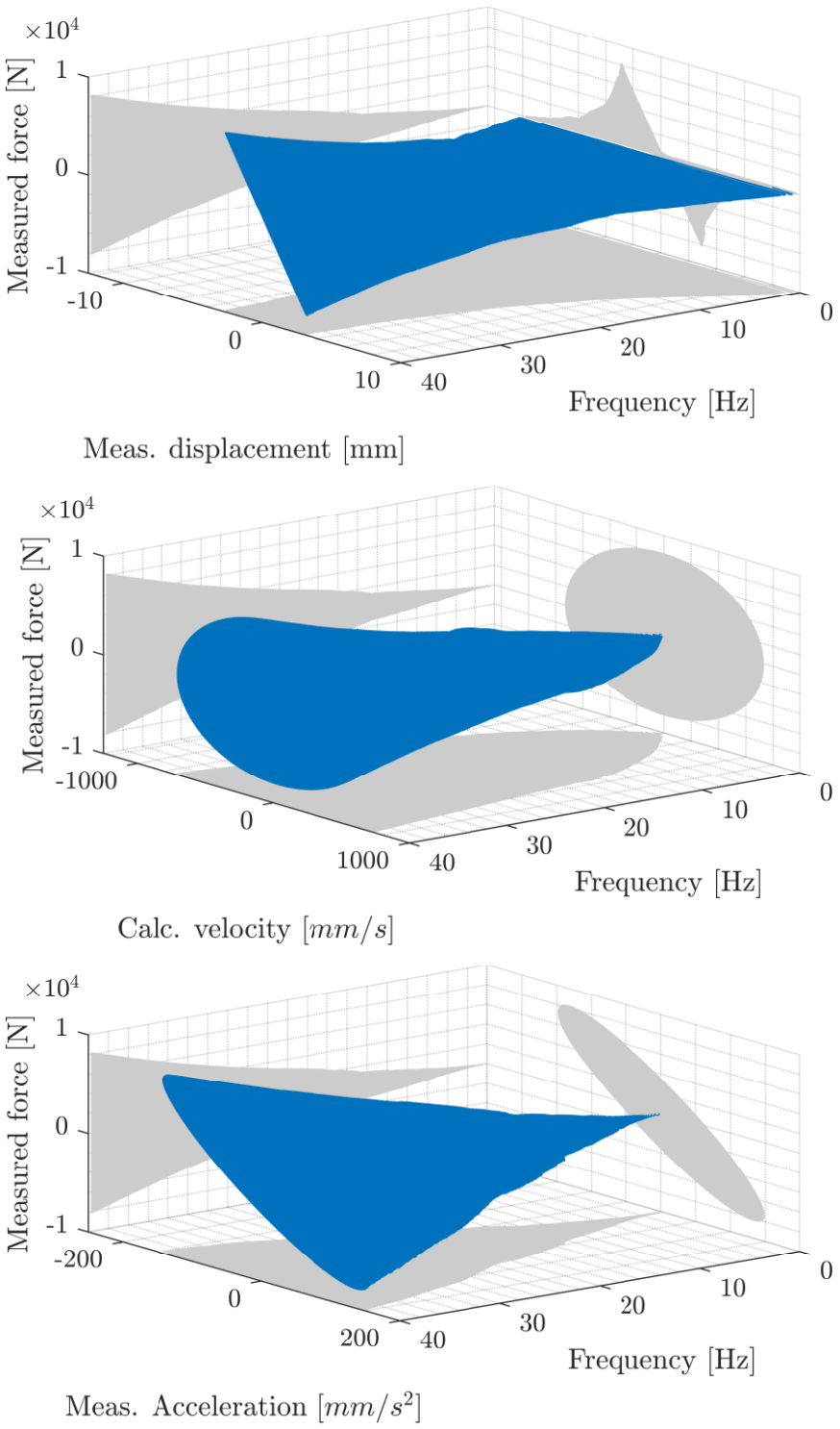

Figure 3.2. Hysteresis curves as a function of the frequency plotting the measured force vs. a) the measured displacement (top), b) the calculated velocity (center), and c) the measured acceleration (bottom).

Finally, Figure 3.2b seems to suggest that there is little dependency between the measured force and the calculated velocity. However, Figure 3.3a shows that the force-velocity relationship for the range of frequencies up to 2.5Hz, which resembles the one seen in Figure 3.1b. Beyond 2.5 Hz this behavior seems to attenuate and become less present in the signal, suggesting that the force-velocity relationship becomes less and less prominent in this hysteretic curve, as shown in Figure 3.3 for the frequency range between 2.5 Hz and 10 Hz.

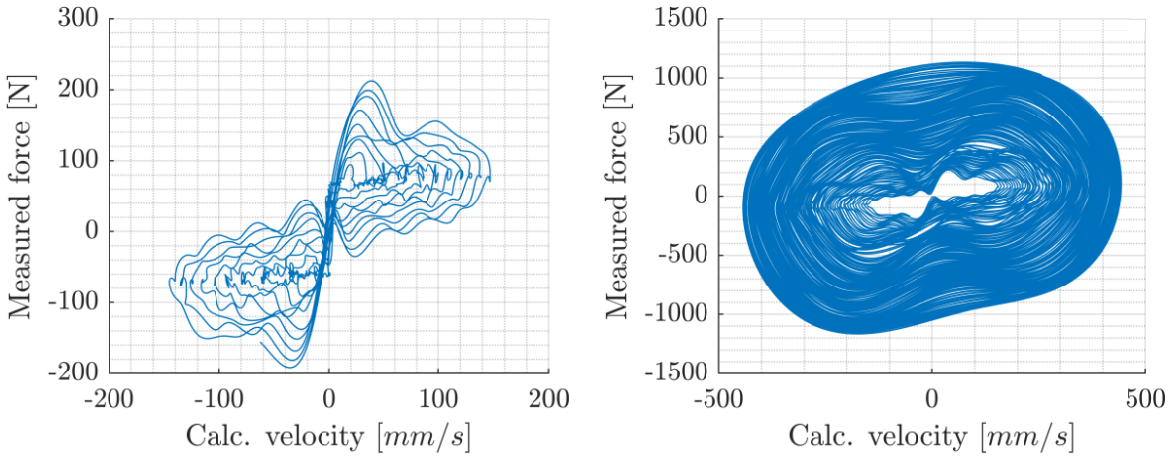

Figure 3.3. Hysteresis curves for measured force vs. computed velocity for the range of a) 0.001 Hz to 2.5 Hz (left) and b) 2.5 Hz and 10 Hz (right).

From the previous analysis of the hysteresis curves, we can conclude that a linear relationship exists between the measured sliding table acceleration and the measured actuator's force. There is no significant elastic restoring force in the system, so it can be considered to be insignificant in our analysis. There is a relationship between the velocity of the sliding table and the actuator force at low frequencies that can be associated with friction damping for a constant portion of the response and a viscous damping related to the linear portion of the response. At high frequencies, this relationship seems to be relatively small when compared to the inertial forces. Based on the analysis and previous conclusions, a mechanical model for the actuator's force (F_a) can be defined as:

$$F_a = m\ddot{x} + c\dot{x} + C_\mu \operatorname{sgn}(\dot{x}) \tag{3.1}$$

where m represents the mass of the sliding table, c is the viscous damping coefficient and $C_\mu$is the Coulomb friction force associated with the railing system which depends on the direction of the velocity of the sliding table.

3.3 Parameter estimation

The estimation of the parameters was done with a linear least squares error approach where the parameters in the mechanical model were estimated from the measured data obtained for the displacement, acceleration, and actuator force. The first parameter to be estimated is the effective mass of the system which subsequently will allow one to obtain the dissipative forces and their parameters from the model (Nilvetti, Pappalardo, & Guida, 2012).

3.3.1 Inertial force parameter estimation

The first parameter is to be identified is the effective mass present in the sliding table system since the inertial contribution $m\ddot{x}$ has a greater influence on the actuator's force signal above 10 Hz. The signals selected for this analysis correspond to the four chirp signals sent to the sliding table because they cover a larger range of frequencies. The estimation begins with the preparation of the signals for the analysis. First, the measured displacements, force, and acceleration signals are passed through a low-pass filter with a cutoff frequency of 50 Hz to eliminate the effect of the oil-column resonance in the signals. To ensure the signals do not contain any distortions due to the sudden start or end of the motion the first and last second of measurements are removed from the time histories. The signal is then broken down into multiple windows of approximately 2.5% of the total signal length and with overlaps of 25% of the window's length.

A linear least squares (LLS) approximation was defined to solve for the different unknown constants in Equation (3.1). The LLS formulation is defined as:

$$\varepsilon_i(F, \ddot{x}, \dot{x}) = f_{m_i}(t) - m\ddot{x}_i(t) + c\dot{x}_i(t) + C_\mu \,\mathrm{sng}[\dot{x}_i(t)] \tag{3.2}$$

where ε_i is the error between the estimated function (F_{a_i}) from Equation (3.1) and the measured force from the actuator (F_i). In matrix form:

$$\varepsilon_i(F, \ddot{x}, \dot{x}) = Y - X\beta \tag{3.3}$$

where Y is a $n \times 1$ vector that contains the measured force (F_i), n is the number of measurements, X is a $n \times 3$ matrix containing the measurement acceleration and calculated velocity data collected, and β is a 3×1 vector that contains the unknown constants. Symbolically:

$$\begin{aligned} Y &= F_i(t) \\ X &= [\ddot{x}_i(t) \quad \dot{x}_i(t) \quad \text{sng}[\dot{x}_i(t)]] \\ \beta &= [m \quad c \quad C_\mu]^T \end{aligned} \tag{3.4}$$

The sum of the squared errors, which is the function to be minimized is:

$$L(Y, X, \beta) = \sum_{i=1}^{n} (Y - X\beta)^2 \tag{3.5}$$

Finally, the linear least squares estimate of the actuator's force will be given by:

$$\hat{\beta} = (X^T X)^{-1} X^T Y \tag{3.6}$$

where $\hat{\beta}$ is the 3×1 vector with the minimizing values.

For this first estimation, the matrix X only contains the measured acceleration $\ddot{x}_i(t)$ since the mass of the system is the minimizing value that will be estimated.

The estimated actuator force is calculated by Equation (3.1) and using the minimizing values of m, c, and C_μ obtained in Equation (3.6). The root mean squared error (RMSE) was calculated between the estimated actuator force and the measured force, it is given by the equation:

$$RMSE = \sqrt{\frac{\sum_{i=1}^{n} [f_m(i) - F_a(i)]^2}{\sum_{i=1}^{n} [f_m(i)]^2}} \cdot 100\% \tag{3.7}$$

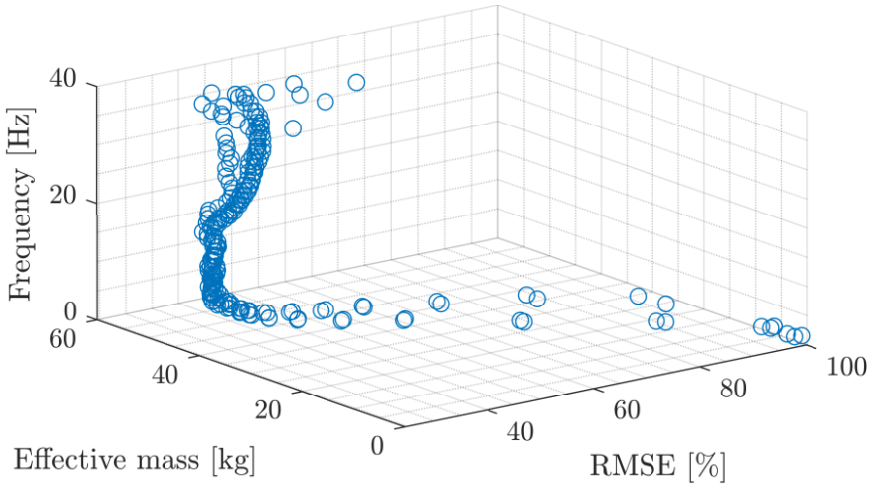

Figure 3.4. Effective mass and RMSE variation for different frequencies.

The LLS estimation procedure was performed for each window taken from the chirp signal, and an estimated mass and its corresponding RMSE value were obtained along with the maximum frequency value found in the window analyzed. The variation of the RMSE and mass for different frequencies is shown in Figure 3.4.

The effective mass, which corresponds to the one with the minimum RMSE was estimated to be 38.1 kg, and this value approximates the measured weight of the sliding table of 36.25 kg. The estimated value for the mass was used in the next section to estimate the dissipative forces.

3.3.2 Dissipative force parameter estimation

The first step in the estimation of the effective dissipative force parameters is taken as the value obtained by subtracting the inertial force from the total measured force of the actuator, symbolically:

$$F_d = F_a - m\ddot{x} = c\dot{x} + C_\mu \,\mathrm{sng}(\dot{x}). \tag{3.8}$$

Equation (3.8) computes the dissipative forces (F_d) that can be used to estimate the parameters of the mechanical model that corresponds to the friction and viscous damping.

The identification method described in the previous section was applied once again to identify the parameters. The variation of the effective viscous damping and the RMSE for different frequencies is shown in Figure 3.5.

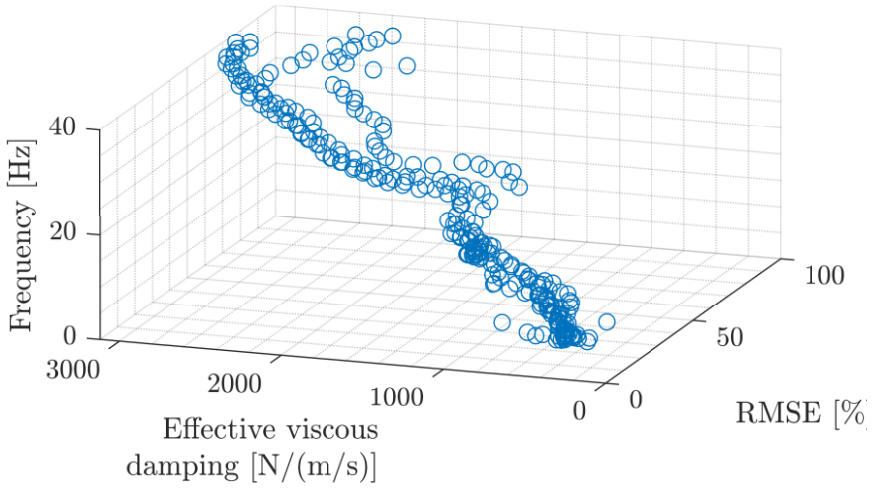

Figure 3.5. Effective viscous damping and RMSE variation for different frequencies.

The effective viscous damping, which corresponds to the value with the minimum RMSE, was estimated to be 415.5N/(m/s), and the effective Coulomb damping coefficient was estimated to be 38.2N. To verify the estimation of the Coulomb damping coefficient, the estimated viscous damping coefficient was held constant while iterating to find a value that would better fit each measured signal used in the analysis at low frequencies since this is the range where the friction damping behavior is more discernible as shown previously in Figure 3.3a. A better fit was found for each signal with an average value of 53.2 N, as shown in Figure 3.6. The final estimated values for the mass, viscous damping, and Coulomb damping are presented in Table 3.2.

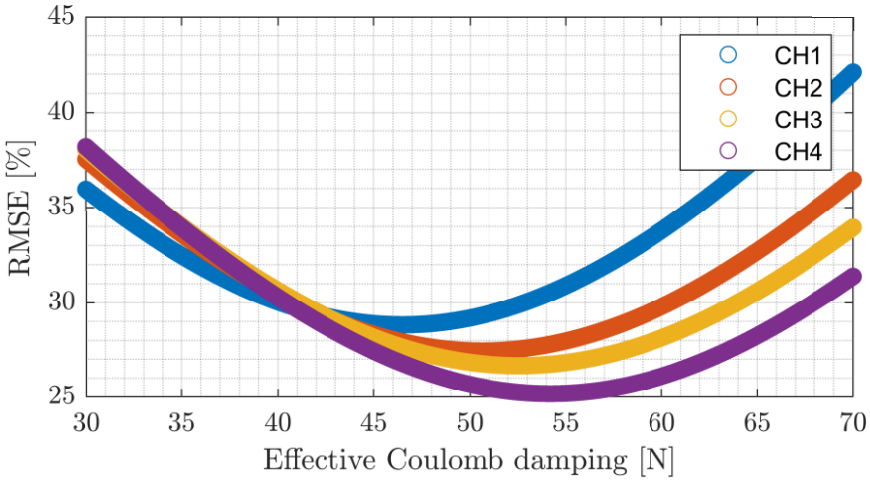

Figure 3.6. Estimated Coulomb damping and RMSE variation for each of the signal in the analysis.

Table 3.2. Estimated values for the mass, viscous linear damping, and Coulomb damping.

$m(kg)$	$c\ (N \cdot s/m)$	$C_\mu(N/m)$
38.06	415.58	50.74

3.3.3 Parametric model validation

The estimated actuator force was calculated with Equation (3.1), and the values from Table 3.2 and compared against the measured actuator force. The hysteresis curves of displacement, velocity, and acceleration for both, the measured and estimated forces are shown in Figure 3.7.

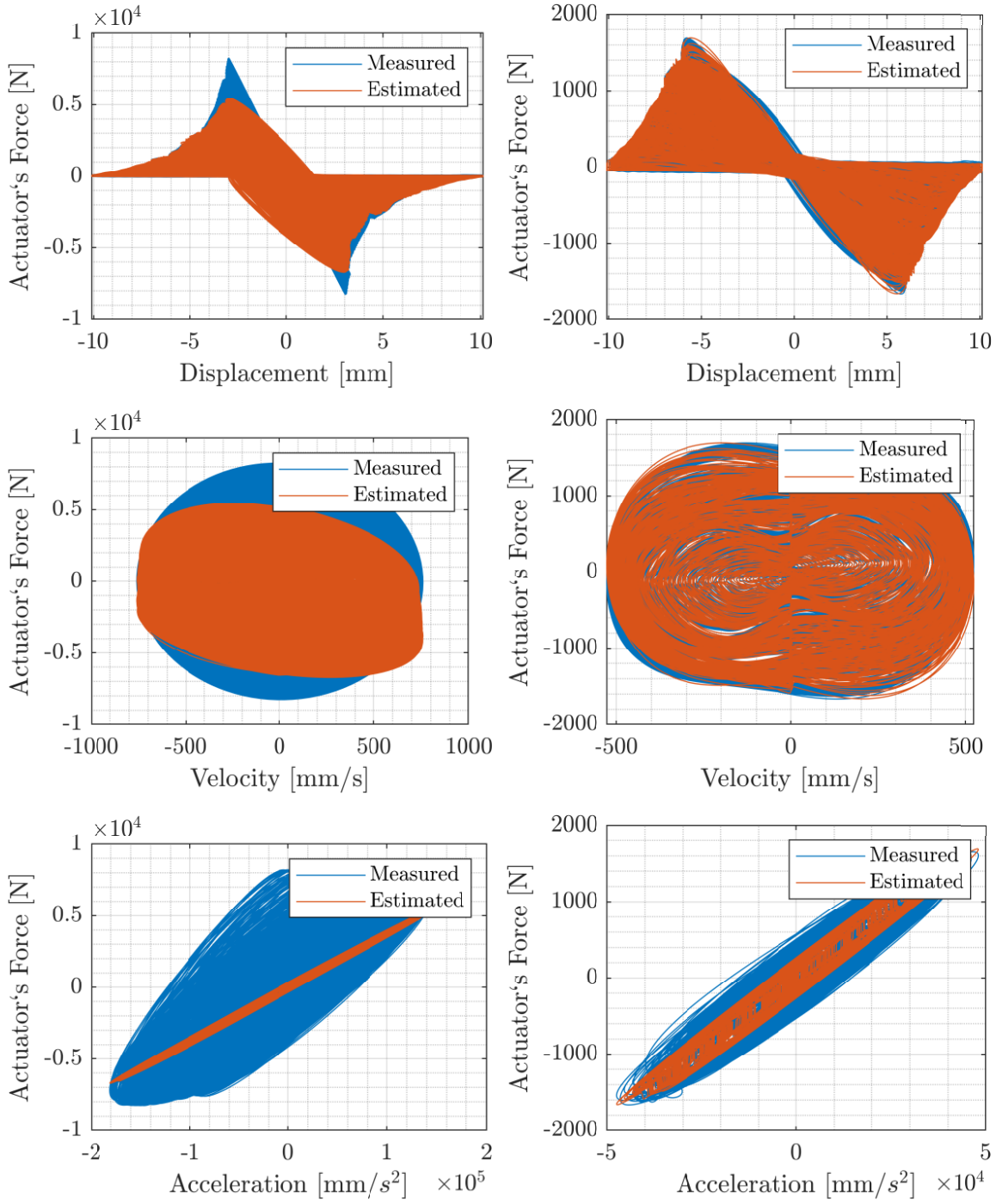

Figure 3.7. Measured and estimated hysteresis curves of a) force vs. displacement (top-left), b) force vs. velocity (top-center), c) force vs. acceleration (bottom-left) for a frequency range up to 39 Hz, d) force vs. displacement (top-left), e) force vs. velocity (top-center), f) force vs. acceleration (bottom-left) for a frequency range up to 13 Hz.

Figures 3.7a through 3.7c shows the discrepancies between the measured and estimated actuator response through the whole range of frequencies up to 39 Hz. Figure 3.7b suggests that these discrepancies are due to mainly the estimation of the dissipative forces since the mechanical model only includes a linear viscous damping approximation and the measured force suggest that there could be a nonlinear damping behavior at high frequencies. The proposed mechanical model fits better the measured data for a low frequency range as shown in Figures 3.7d through 3.7f which considers only the range of frequencies up to 13 Hz. The average RMSE obtained for the signals tested was 9.2%. Figure 3.8 shows that the model seems to approximate well the behavior of the actuator's force against the velocity for the frequency range up to 1.5 Hz

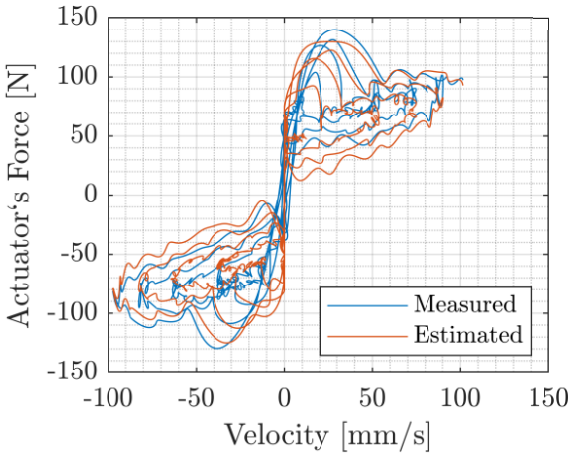

Figure 3.8. Measured and estimated hysteresis curves of the actuator's force vs. velocity for a frequency range up to 1.5 Hz.

4. MODELING AND IDENTIFICATION OF THE TRANSFER SYSTEM

The formulation and identification of a parametric model for the transfer system is explained in this chapter. Section 4.1 describe the theory behind the equations that describe the dynamics of the servo valve and actuator. Section 4.2 presents the procedure taken in the identification of the model's parameters.

4.1 Servo-hydraulic system

Throughout the years, many models have been proposed to represent the mechanics of a servo valve, some of these representations model the dynamics as a proportional gain (Dyke, Spencer, Quast, & Sain, 1995), as a linear model as a function of a proportional gain and a time constant to account for the speed at which the servo valve responds to the input (De Silva, 2015). Second and higher-order models exist in the literature. However, the modal analysis performed in Section 2.4.1 to the signal from the measurements of the bare sliding table response suggests that the system could be modeled as a first linear system with a static gain and a time constant. De Silva (2015) described a system with these characteristics, which are analogous to a tachometer.

The differential equation that describes the assumed behavior of the servo valve is:

$$\tau_v \dot{x}_v + x_v = k_v i_c \tag{4.1}$$

where i_c is the input command that is sent to the servo valve which produces a spool displacement x_v as the output, τ_v is the time constant and k_v is a static gain (Conte & Trombetti, 2000). The corresponding transfer function (G_v) will be:

$$G_v = \frac{k_v}{\tau_v s + 1}. \tag{4.2}$$

This representation of the dynamics of the servo valve is valid through a frequency range up to 50 Hz and it is under the assumption that it is operating without saturation and the servo valve flow-gain relationship is constant around the neutral position, which implies that the spool size is the same as the orifices of the servo valve and there is not over or under lap between them (Kusner, Rood, & Burton, 1992).

The internal servo valve pressure loss-flow relationship is described by considering the pressure loss in the internal chambers of the servo valve from the pressure and return lines due to the displacement of the spool, and the size of the valve orifices. This results in the following nonlinear square root function as a function of the spool displacement x_v:

$$Q_L = C_d \cdot w \cdot x_v \sqrt{\frac{1}{\rho}(P_S - \text{sgn}[P_L])} \tag{4.3}$$

where Q_L is the flow through the load that enters and exits the servo valve to and from the hydraulic actuator, C_d is the coefficient of discharge of the servo valve orifices, w is the rate of change of the opening of the valve orifices with respect to the spool displacement, ρ is the oil density, P_S is the supply pressure, and P_L is the pressure difference between the load entering one actuator chamber and the load exiting the other chamber. This equation can be linearized with respect to a specific operating point (the origin) (Merritt, 1991; Wei, 2009), where it becomes:

$$Q_L = K_{qq} x_v - K_{cc} P_L \tag{4.4}$$

where K_{qq} is the flow gain and K_{cc} is the flow-pressure coefficient, these valve coefficients vary depending on the operating point chosen.

The equations that govern the dynamic behavior of the hydraulic actuator is the flow continuity equation:

$$Q_L = A\dot{x}_m + C_l P_L + \frac{V}{4\beta}\dot{P}_L \tag{4.5}$$

where A is the area of the piston, C_l is the leakage coefficient, V is the total volume of the fluid under compression in both chambers of the actuator and β is the effective bulk modulus of the oil. For this study, the command displacement x_c is applied by a proportional controller with a gain K_p.

$$i_c = K_p(x_c - x_m) \tag{4.6}$$

The equilibrium equation for the sliding table is expressed as:

$$f = \frac{P_L}{A} = m\ddot{x}_m + c\dot{x}_m \tag{4.7}$$

where, m and c corresponds to the mass and damping identified for the sliding table. In this section a simple mass damper system was selected to represent the dynamics of the sliding table and to

simplify the calculations. The term corresponding to the Coulomb friction will be omitted since its contribution is very small when compared to the other parameters (Chase, Hudson, Lin, Elliot, & Aylwin, 2005). When combining Equations (4.4), (4.5), and (4.7) we get:

$$\dot{f} = \frac{4\beta}{V}\left(AK_{qq}x_v - A^2\dot{x}_m - (K_{cc} + C_l)\cdot f\right). \tag{4.8}$$

By defining the variable: $K_c = K_{cc} + C_l$, Equation (4.2), (4.6), and (4.8) can be represented in block diagram form as shown in Figure 4.1.

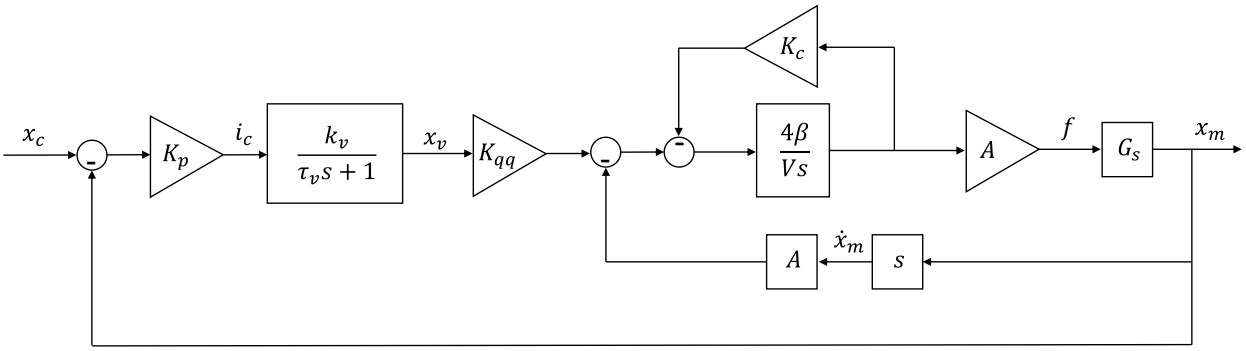

Figure 4.1. Block diagram of the plant.

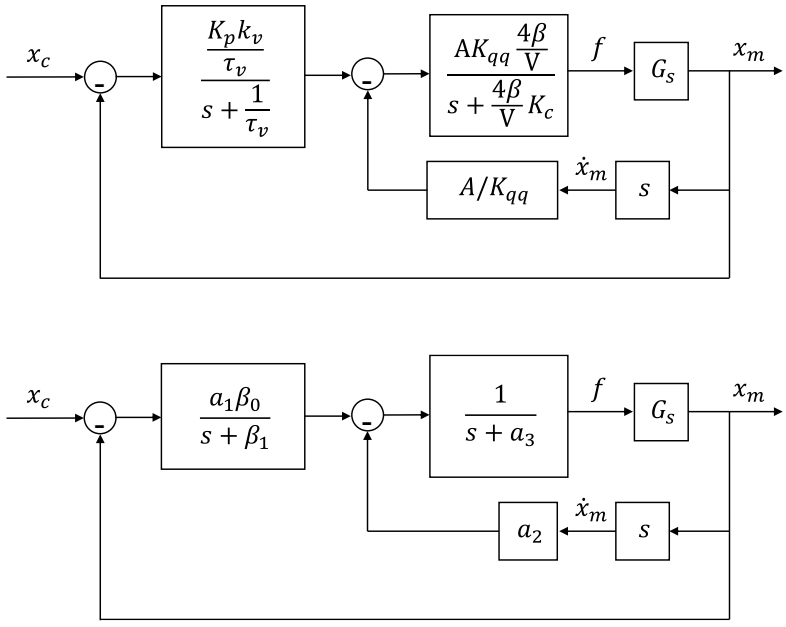

Figure 4.2. Condensation of the block diagram of the plant. a) Condensed block diagram (top) and b) variable change (bottom)

The plant shown in Figure 4.1 can be condensed though the process shown in Figure 4.2 where G_s represents the transfer function of the physical specimen (Maghareh, Silva, & Dyke, 2018) and new variables a_1, a_2, a_3, β_0, and β_1 are defined as follows:

$$a_1 = AK_{qq}\frac{4\beta}{V} \quad ; \quad a_2 = A^2\frac{4\beta}{V} \quad ; \quad a_3 = \frac{4\beta}{V}K_c$$
$$\beta_0 = \frac{K_p k_v}{\tau_v} \quad ; \quad \beta_1 = \frac{1}{\tau_v} \tag{4.9}$$

The condensed block diagram preserves the velocity feedback loop that exist between the specimen and sliding table, and the actuator dynamics due to the control structure interaction (Dyke, Spencer, Quast, & Sain, 1995). The variable a_2 represents the stiffness of the oil and if we divide this quantity by the mass of the shake stable and the specimen, we can determine the oil-column resonance of the actuator, symbolically:

$$f_{OCR} = \frac{1}{2\pi}\cdot\sqrt{\frac{A^2\frac{4\beta}{V}}{m}} \tag{4.10}$$

If we specify the physical specimen transfer function as:

$$G_s = m\ddot{x}_m + c\dot{x}_m \tag{4.11}$$

The condensed system in Figure 4.2 can be represented by a single transfer function, given by:

$$G_{m/c} = \frac{n_0}{d_4 s^4 + d_3 s^3 + d_2 s^2 + d_1 s + d_0} \tag{4.12}$$

where:

$$\begin{aligned} n_0 &= a_1\beta_0 \\ d_4 &= m \\ d_3 &= a_3 m + c + \beta_1 m \\ d_2 &= a_3 c + a_2 + \beta_1 a_3 m + \beta_1 c \\ d_1 &= \beta_1 a_3 c + \beta_1 a_2 \\ d_0 &= a_1\beta_0 \end{aligned} \tag{4.13}$$

4.2 Parametric model identification

The identification process starts with the estimation of a transfer function that takes the desired displacement sent to the system and outputs the measured displacement with the MATLAB

function `tfest`. The signals used to identify the plant were six BLWN signals. This signal was selected since it contains information on the oil-column resonant frequency and covers a larger range of frequencies when compared with a chirp or a triangular signal. This transfer function is set as a fourth-order function with four poles and no zeros (Maghareh, Silva, & Dyke, 2018). The relationships shown in Equation (4.13) are then used to compute the parameters $a_1\beta_0$, a_2, a_3, and β_1. These parameters are estimated through a nonlinear least squares estimation done with MATLAB.

The identified parameters were then inputted into a Simulink model of the block diagram in Figure 4.2 along with a chirp input signal of 10 mm of amplitude and spanning over a frequency range from 0.001 Hz to 40 Hz. The RMS error was calculated between the output signal of the Simulink model and the signal measured in the laboratory due to the same input signal. This process was repeated for each of the BLWN test signals, and the set of parameters with the least RMS error were selected as the final parameters that were used for the virtual model of the transfer system. The values for the parameters identified are presented in Table 4.1.

Table 4.1. Values identified for the parametric model of the transfer system.

$\boldsymbol{\beta_1(1/sec)}$	$\boldsymbol{a_1\beta_0(m\,Pa/sec^2)}$	$\boldsymbol{a_2(m\,Pa)}$	$\boldsymbol{a_3(1/sec)}$
$\mathbf{228.76}$	6.3208×10^{10}	5.5831×10^{6}	116.98

The frequency response functions of the virtual model of the transfer system are compared in Figure 4.3 against the estimated transfer function that was estimated from measured data. The frequency response functions were estimated from external command to measured sliding table displacement. The comparison between the measured displacement time histories is shown in Figure 4.4.

Figure 4.3 shows that the simulated model response gain variation with frequency and the test signal have an RMSE of 9.4%. The model can approximate the measured displacement with an average RMSE of 8.8% for all test signals for the full range of frequencies in the test signal (0.001Hz to 40Hz). The difference in gain that is shown in Figure 4.3 is attributed to the difference in the nature of the signal used for estimation (BLWN) and the ones used for validation (Chirp) for a comparison between signals of the same nature, the RMSE between the estimated and

simulated gain curves was observed to go as low as 4%. The model simulates the phase spectra of the test signals with an RMSE of 7% for the whole frequency range of interest.

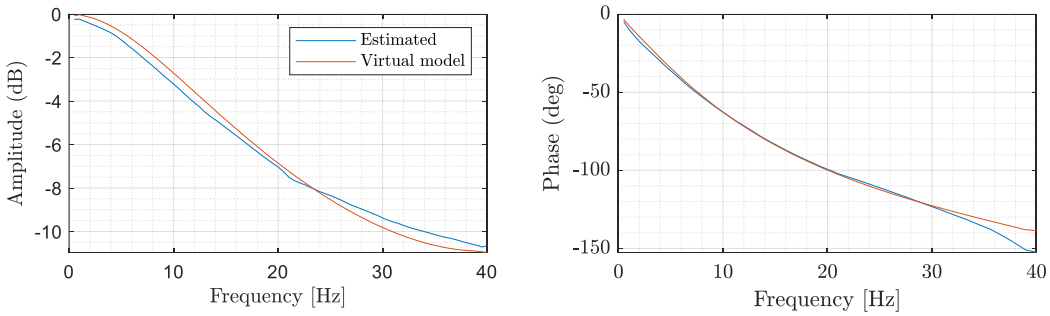

Figure 4.3. Amplitude (left) and phase spectra (right) of the virtual model and estimated transfer function of the transfer system.

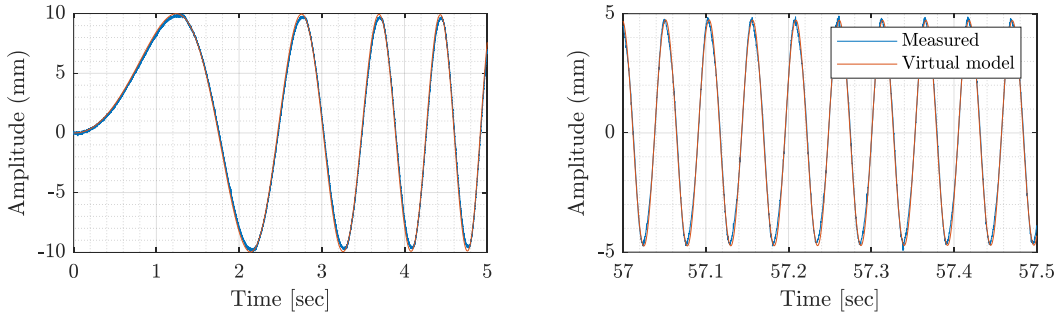

Figure 4.4. Displacement experimentally measured and obtained from the virtual model of the transfer system for a (left) frequency range from 0.001 to 2Hz and (right) at a frequency of 19 Hz.

The model, however, overestimates the forces generated for signals with lower amplitudes (5 mm) and underestimates them when the input signal has large amplitudes (10 mm). The oil-column frequency corresponding to the set of parameters chosen is 61 Hz which is similar to the 71 Hz identified through a transfer function estimation, with a difference of 14%. Even though this percentage is considerably high, the desired effect of the oil-column resonance is indeed captured in the model, which is a helpful feature when modeling a control system since it is imperative to model a controller that does not substantially intensify this resonance.

5. PARAMETRIC IDENTIFICATION AND MODELING OF THE SPECIMENS

The present chapter describes the models adopted to describe the hysteretic behavior of the isolators. Two Bouc-Wen models accounting for different levels of nonlinearities are described in Section 5.1 followed by the results of the identification process and the fitting of each model to the different types of isolators in Section 5.2.

5.1 Bouc-Wen model

The restoring force $f_m(t)$ measured from the isolators is a highly nonlinear quantity since it will depend on the nonlinear hyper elastic and viscoelastic material behavior of the rubber (Al-Azawi, Said, Almusaui, & Al-Zaidee, 2017), contact nonlinearities due to the characteristic unbonded nature of the isolator, and the composite interaction between the reinforcement fiber layers and the rubber layers.

The Bouc-Wen model is a method widely used to represent the hysteretic curve of various classes of nonlinear materials and structural members (Ikhouane & Rodellar, 2007). Many modifications have been implemented to the model to account for different types of nonlinearities such as softening, hardening (Manzoori & Toopchi-Nezhad, 2017), stiffness and strength degradation (Erlicher & Bursi, 2009), force asymmetry (Chen & Ahmadi, 1992), etc. The isolator restoring force can be captured through a Modified Bouc-Wen Model that accounts for the softening of the isolator at the beginning of the deformations and a hardening behavior that the isolator develops at very large deformations (when the vertical faces of the isolator come in total contact with the top and bottom plates). This behavior is observed in the hysteretic response of the isolator as inflection points. In the softening stage, the isolator experiences relatively greater displacement without a significant increase of the shear force and in the hardening stage, the shear force increases as the deformations increase. This behavior is more evident in isolators with natural rubber and carbon fiber reinforcement, while for isolators with natural or recycled rubber and polyester fiber reinforcement these nonlinearities are subtler. The original Bouc-Wen Model does not account for the variation in the stiffness or the force asymmetry since the total force in the model is the sum of a linear term and a hysteretic term. The linear term dictates the variation of

the stiffness in the model; thus, the slope of the overall hysteresis loops will remain linear due to this term. Manzoori & Toopchi-Nezhad (2017) proposed an extension to the Modified Bouc-Wen Model presented by Chen & Ahmadi (1992) (Chen & Ahmadi, 1992) which accounts for this nonlinear behavior by introducing a fifth order polynomial term that describes the variation of the stiffness with the lateral displacement (Manzoori & Toopchi-Nezhad, 2017). The isolator force that this model helps to predict, $f_{BW5}(t)$, is given by:

$$f_{BW}(t) = f_K(t) + f_C(t) \tag{5.1}$$

The elastic contribution, $f_K(t)$, is approximated as a 5th-order polynomial with five coefficients. The 3rd and 5th order terms in this polynomial will help account for the distinctive softening and subsequent hardening behavior of the isolators. The lateral force time history asymmetry with respect to the x-axis, can be modeled by including a 2nd and 4th-order terms shown in equation (5.2).

$$f_K(t) = a_1 x + a_2 x^2 + a_3 x^3 + a_4 x^4 + a_5 x^5 \tag{5.2}$$

The dissipative contribution, $f_C(t)$, will be given by a linear component proportional to the lateral velocity and the hysteretic component as a function of the hysteric variable $z(t)$, as given in equations (5.3) and (5.4), respectively.

$$f_C(t) = c_{bw}\dot{x} + b\left(1 - \frac{\beta}{A}|z|^n\right)z, \text{ and} \tag{5.3}$$

$$\dot{z}(t) = \frac{1}{Y}(A\dot{x} - \beta\dot{x}|z|^n - \gamma|\dot{x}||z|^{n-1}z). \tag{5.4}$$

In the previous equations z is the hysteretic variable that controls the hysteretic behavior of the isolator, c_{bw} is the viscous damping coefficient, and A, β, Y, b, and n are parameters that control the shape of the hysteresis loops.

Equation (5.2) is the elastic contribution to the restoring force and has a linear term $a_1 x$ that can be assumed as an initial stiffness that acts on the system in Equation (2.14) taking $k_1 = a_1$. This is done to ensure that K_n and C_n in Equation (2.13) are well-conditioned matrices, the same can be assumed for the damping contribution as $c_1 = c_{bw}$.

As explained in Section 2.3, certain isolators present a behavior where the softening and hardening effects are very subtle, for these isolators a Bouc-Wen model with a linear dependency on the average stiffness of the isolator was used, as given by:

$$f_{BW}(t) = \alpha k_0 x + (1-\alpha) k_0 z \tag{5.5}$$

$$\dot{z}(t) = \dot{x}[A - |z|^n(\gamma + \beta \text{sgn}(\dot{x}z))] \tag{5.6}$$

In the previous equations, k_0 is the initial stiffness, α is the ratio between the post yielding to pre yielding stiffness, and A, β, and n are parameters that control the shape of the hysteresis loops.

Two models were selected to serve as a comparison of how well each of these models match the behavior of the isolator measured both from the shear tests and from the RTHS tests with seismic loading.

5.2 Parameter estimation

The estimation of the parameters from the two models presented in Section 5.1 was done with the parameter estimation tool from Simulink, which performs the estimation by minimizing the sum of the squared errors.

The estimation procedure starts with the filtering of the displacement, acceleration, and force signals from high-frequency content to remove the effect of the oil-column frequency from the data, this objective is achieved through a low-pass filter with a cut-off frequency of 25 Hz. In this step, the velocity signal is also estimated from the displacement time history. The next step is to remove the inertial and dissipative forces introduced by the sliding table from the measured force signal so we can obtain the restoring force corresponding to the isolator, symbolically:

$$f_I(t) = f_m(t) - m\ddot{x}_m + c\dot{x}_m. \tag{5.7}$$

After the signals are prepared, the measured displacement, x_m, is set as the input signal in the simulation and the calculated isolator force, f_I, is set as the output. The parameter estimator tool from Simulink then performs the estimation until the change in the sum of the squares compared to its initial value is less than the default threshold value set of 1e-6. After the parameters have been collected, they are input back into the Bouc-Wen model and along with the measured displacement from each of the test signals selected for the estimation and are run through the model to obtain the estimated force, f_{BW}. The estimated force is compared with the measured force, f_I, and a RMSE value is calculated between these two signals. The set of parameters that yielded the least amount of error is selected as the final values of the estimation and are presented, for the

Bouc-Wen model presented in Equation (5.1), in Table 5.1 through 5.6, the visualization of the fitting of the model to the measured data is shown in Figures 5.1 through 5.6.

Table 5.1. Estimated values for the Bouc-Wen model with a fifth order polynomial for the Isolator NCA1.

A	n	γ	β	Y	c_{bw}
$\mathbf{6.2019e-01}$	$1.0015e+00$	$-5.0622e+00$	$-2.8707e+00$	$-7.8691e+00$	$9.0382e-14$
b	$a1$	$a2$	$a3$	$a4$	$a5$
$\mathbf{-6.0629e+02}$	$9.0447e+01$	$-3.6592e-01$	$-9.1027e-02$	$4.1912e-04$	$6.7086e-05$

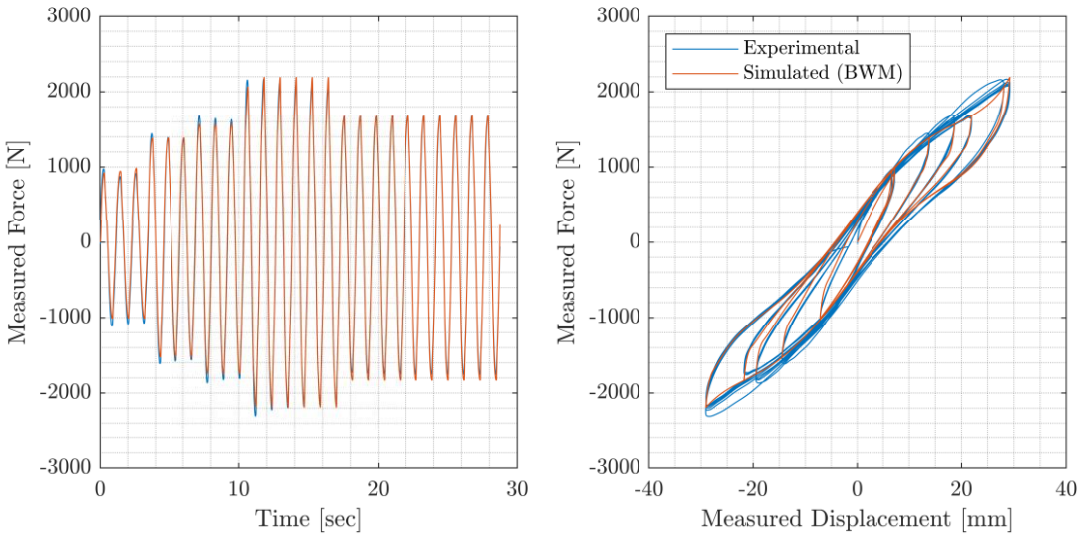

Figure 5.1. Fitting of the estimated Bouc-Wen model with a fifth order polynomial for the Isolator NCA1. a) Measured force time history and b) hysteresis curve.

Table 5.2. Estimated values for the Bouc-Wen model with a fifth order polynomial for the Isolator NPA1.

A	n	γ	β	Y	c_{bw}
$\mathbf{7.5080e-03}$	$2.3627e+00$	$-4.4791e-03$	$-2.5005e-03$	$-1.4494e-02$	$8.9387e-14$
b	$a1$	$a2$	$a3$	$a4$	$a5$
$\mathbf{-7.9702e+01}$	$6.0823e+01$	$-4.2709e-01$	$-5.1962e-02$	$3.1199e-04$	$3.9400e-05$

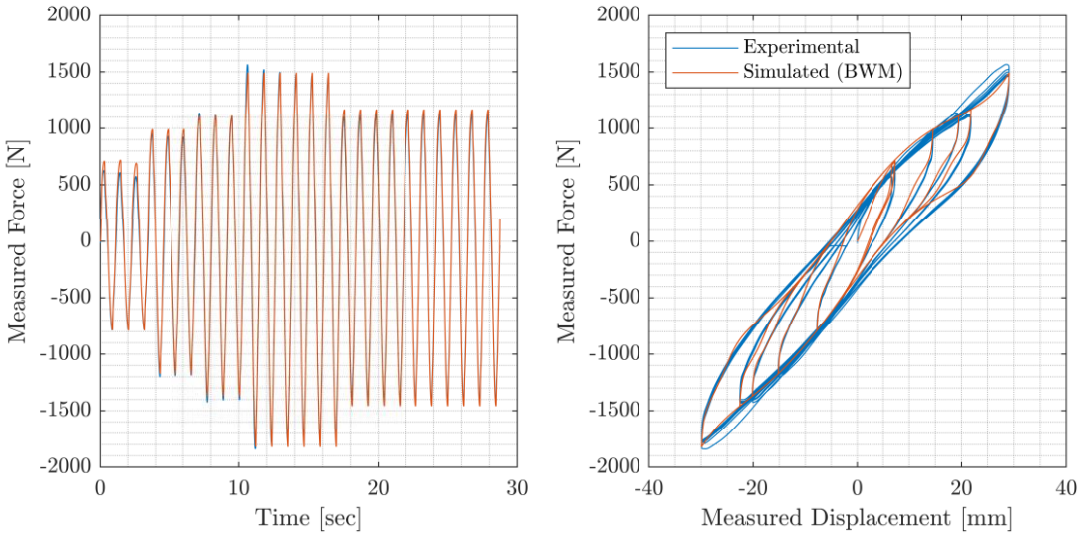

Figure 5.2. Fitting of the estimated Bouc-Wen model with a fifth order polynomial for the Isolator NPA1. a) Measured force time history and b) hysteresis curve.

Table 5.3. Estimated values for the Bouc-Wen model with a fifth order polynomial for the Isolator NPB8.

A	n	γ	β	Y	c_{bw}
$\mathbf{1.1924e+00}$	$2.9386e+00$	$-1.1047e+01$	$-2.7329e+00$	$-9.0858e+00$	$9.0381e-14$
b	$a1$	$a2$	$a3$	$a4$	$a5$
$\mathbf{-8.1703e+02}$	$9.4066e+01$	$-1.7597e+00$	$-1.9687e-01$	$2.5433e-03$	$1.6542e-04$

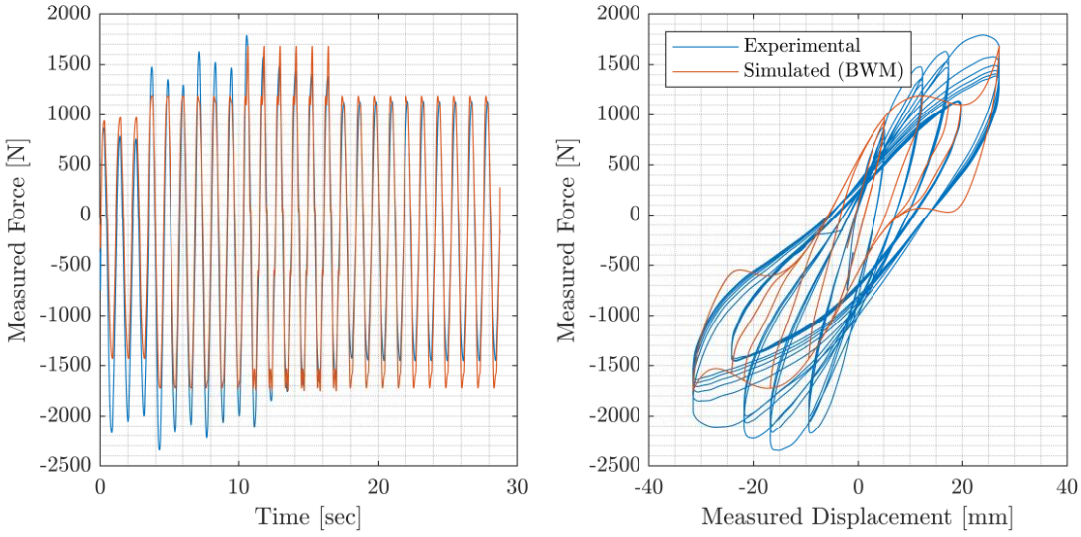

Figure 5.3. Fitting of the estimated Bouc-Wen model with a fifth order polynomial for the Isolator NPB8. a) Measured force time history and b) hysteresis curve.

Table 5.4. Estimated values for the Bouc-Wen model with a fifth order polynomial for the Isolator RPA1.

A	n	γ	β	Y	c_{bw}
$\mathbf{2.4312e-01}$	$1.0012e+00$	$-3.7507e+00$	$-3.1316e+00$	$-8.1565e+00$	$9.0382e-14$
b	$a1$	$a2$	$a3$	$a4$	$a5$
$\mathbf{-1.5338e+03}$	$1.2218e+02$	$-3.6421e-01$	$-8.0871e-02$	$4.2023e-04$	$7.1514e-05$

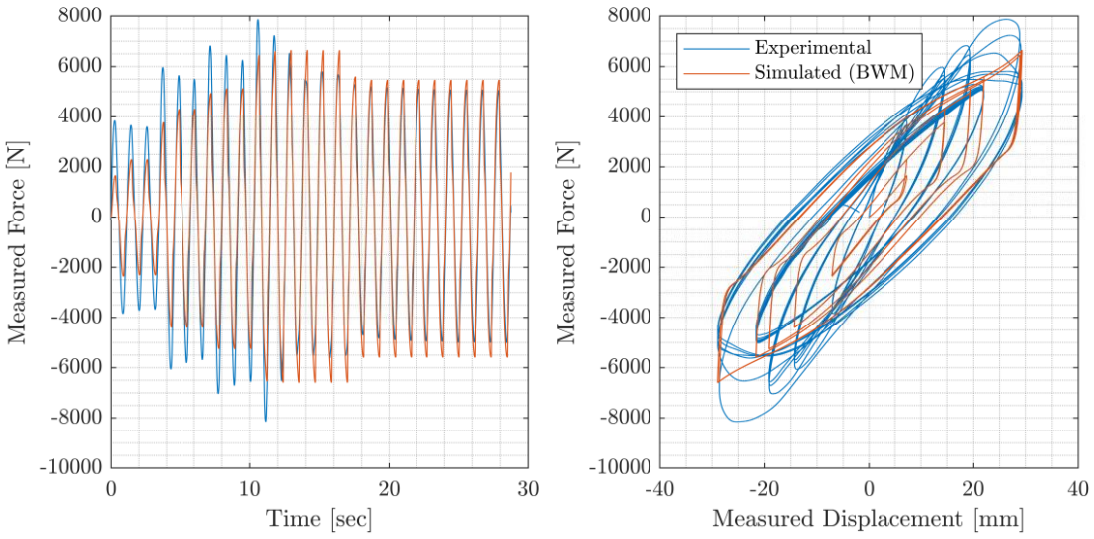

Figure 5.4. Fitting of the estimated Bouc-Wen model with a fifth order polynomial for the Isolator RPA1. a) Measured force time history and b) hysteresis curve.

Table 5.5. Estimated values for the Bouc-Wen model with a fifth order polynomial for the Isolator RPB2.

A	n	γ	β	Y	c_{bw}
$\mathbf{6.5241e-01}$	$1.0001e+00$	$-3.9769e+00$	$-3.2115e+00$	$-7.8646e+00$	$9.0382e-14$
b	$a1$	$a2$	$a3$	$a4$	$a5$
$\mathbf{-6.4081e+02}$	$9.7666e+01$	$-3.6547e-01$	$-8.8368e-02$	$4.1916e-04$	$6.8427e-05$

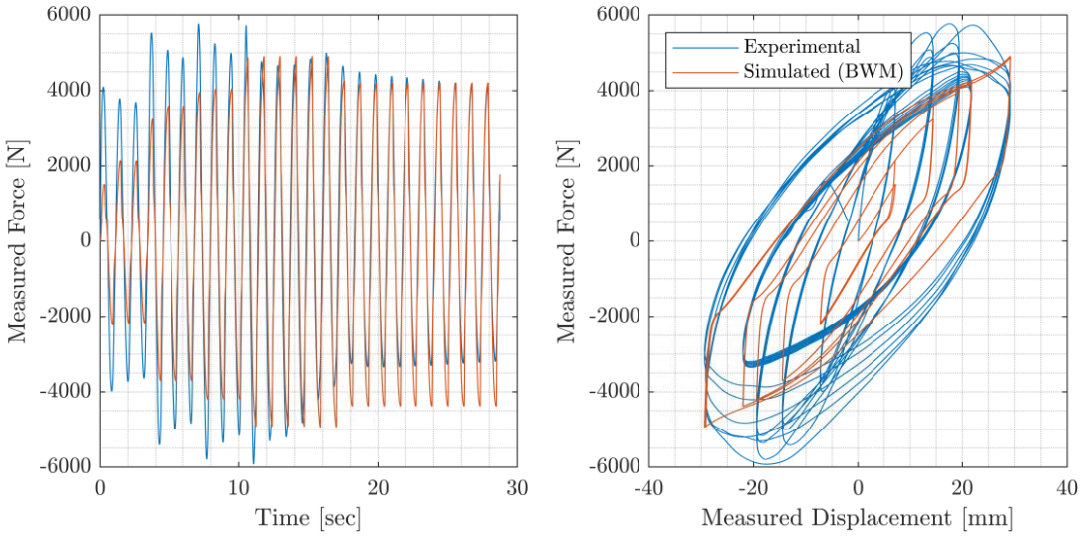

Figure 5.5. Fitting of the estimated Bouc-Wen model with a fifth order polynomial for the Isolator RPB2. a) Measured force time history and b) hysteresis curve.

Table 5.6. Estimated values for the Bouc-Wen model with a fifth order polynomial for the Isolator RPC9.

A	n	γ	β	Y	c_{bw}
$\mathbf{7.2527e-02}$	$1.0055e+00$	$-3.6824e+00$	$-3.2905e+00$	$-7.9241e+00$	$9.0381e-14$
b	$a1$	$a2$	$a3$	$a4$	$a5$
$\mathbf{-3.0709e+03}$	$1.0543e+02$	$-3.6553e-01$	$-8.4917e-02$	$4.1824e-04$	$7.0395e-05$

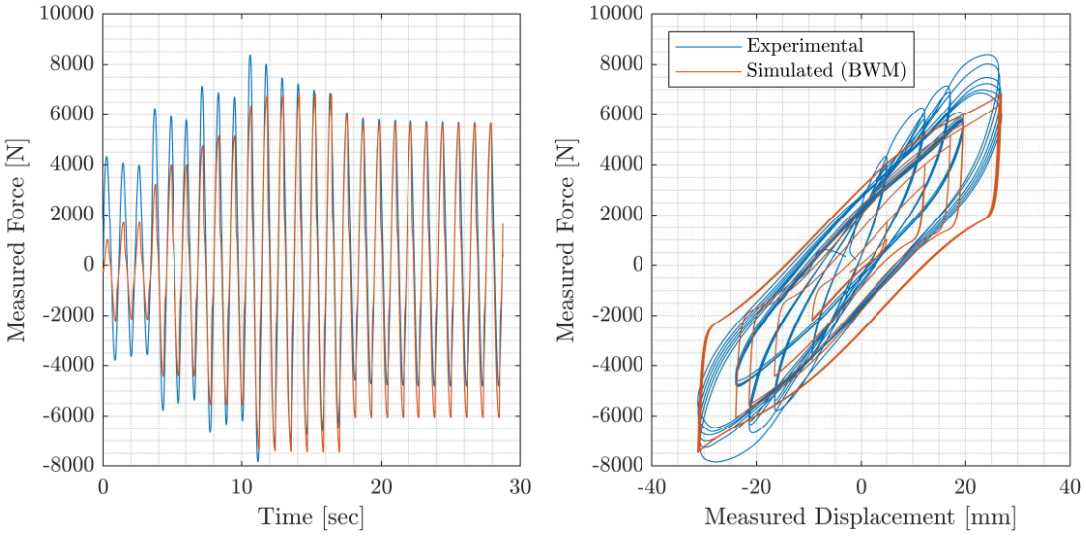

Figure 5.6. Fitting of the estimated Bouc-Wen model with a fifth order polynomial for the Isolator RPC9. a) Measured force time history and b) hysteresis curve.

The estimation procedure is repeated for the Bouc-Wen model that possesses a linear dependency on the average stiffness for all the previous specimens. The resulting set of parameters are presented in Table 5.7 through Table 5.12, the visualization of the fitting of the model to the measured data is shown in Figures 5.7 through 5.12.

Table 5.7. Estimated values for the Bouc-Wen model with a linear stiffness relationship for the Isolator NCA1.

A	n	γ	β	k_0	α
$\mathbf{2.8421e-01}$	$2.6581e+00$	$-4.0526e+07$	$4.1502e+07$	$1.8856e+05$	$3.4687e-01$

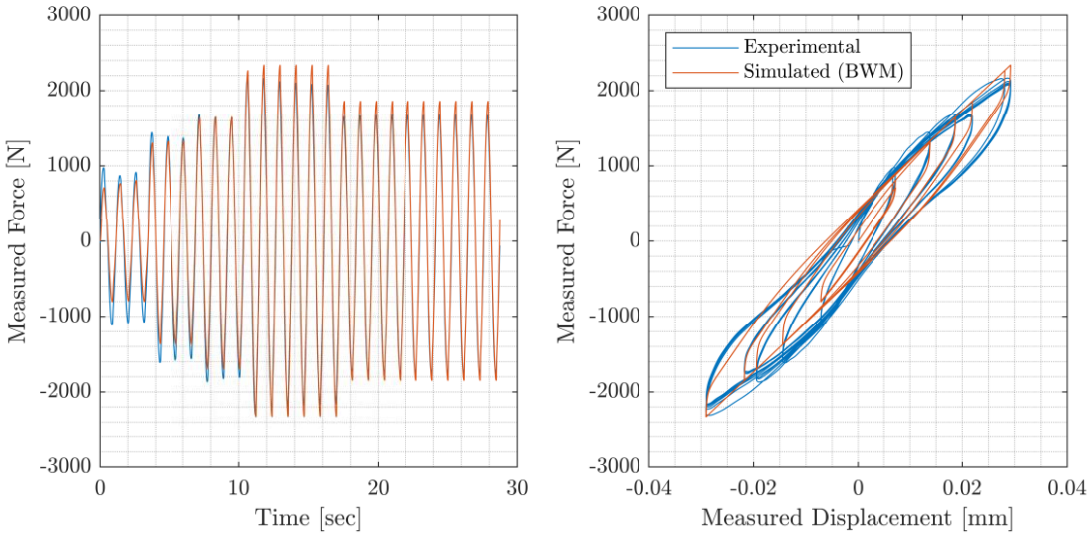

Figure 5.7. Fitting of the estimated Bouc-Wen model with a linear stiffness relationship for the Isolator NCA1. a) Measured force time history and b) hysteresis curve.

Table 5.8. Estimated values for the Bouc-Wen model with a linear stiffness relationship for the Isolator NPA1.

A	n	γ	β	k_0	α
$\mathbf{4.3129e-01}$	$1.5948e+00$	$-2.7968e+04$	$3.0449e+04$	$1.2854e+05$	$3.4830e-01$

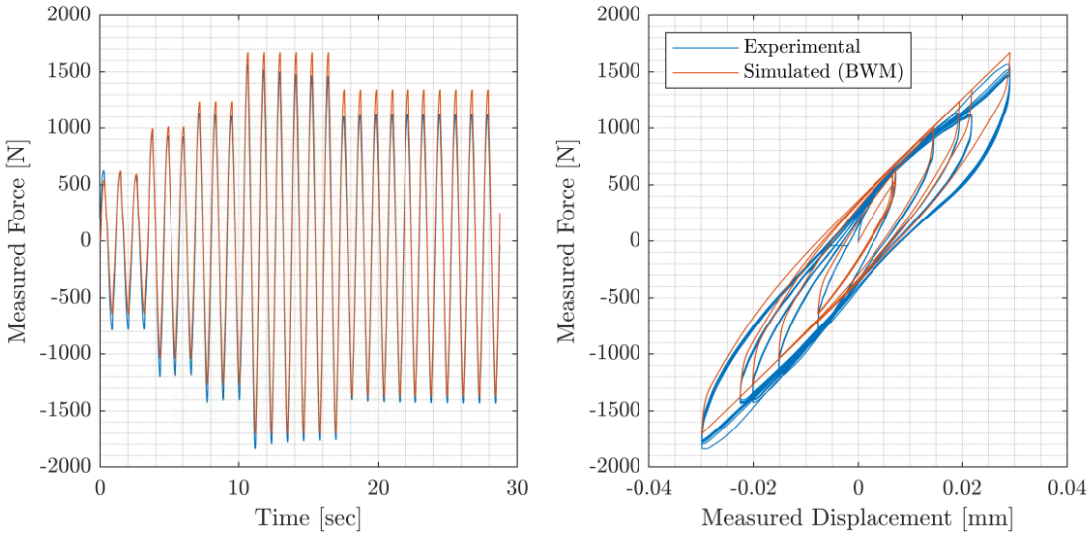

Figure 5.8. Fitting of the estimated Bouc-Wen model with a linear stiffness relationship the Isolator NPA1. a) Measured force time history and b) hysteresis curve.

Table 5.9. Estimated values for the Bouc-Wen model with a linear stiffness relationship for the Isolator NPB8.

A	n	γ	β	k_0	α
$\mathbf{1.1592e+00}$	$2.0756e+00$	$-9.1369e+04$	$1.2927e+05$	$1.3015e+05$	$3.5872e-01$

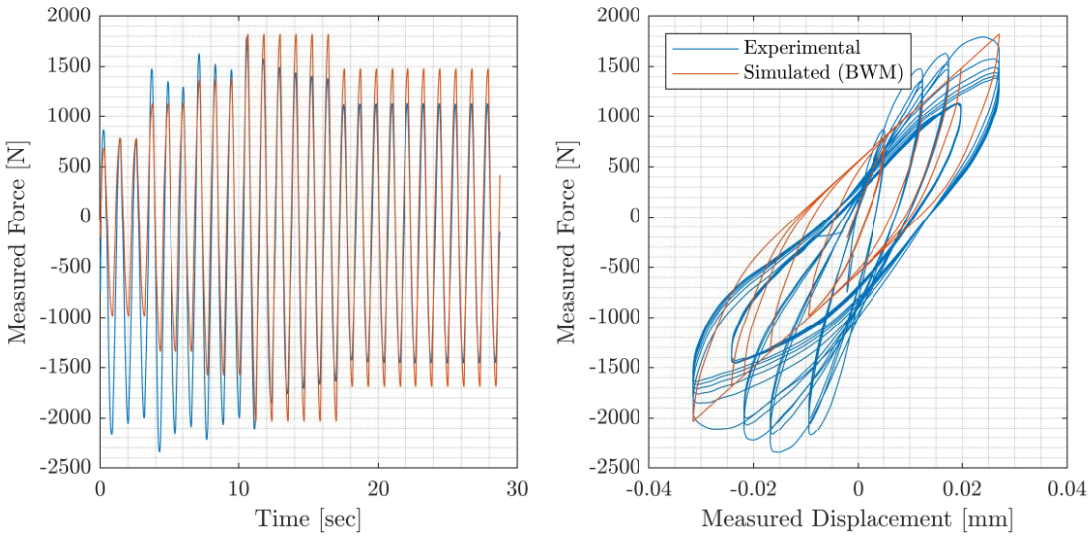

Figure 5.9. Fitting of the estimated Bouc-Wen model with a linear stiffness relationship for the Isolator NPB8. a) Measured force time history and b) hysteresis curve.

Table 5.10. Estimated values for the Bouc-Wen model with a linear stiffness relationship for the Isolator RPA1.

A	n	γ	β	k_0	α
$\mathbf{1.4977e+00}$	$2.9148e+00$	-4.3787e+05	$6.0062e+05$	$2.7228e+05$	$4.2926e-01$

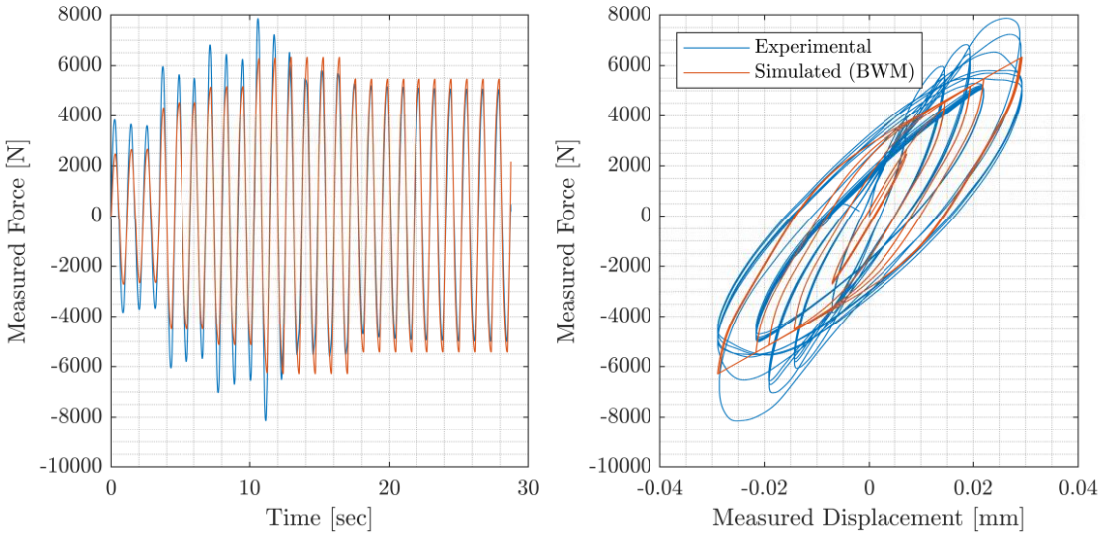

Figure 5.10. Fitting of the estimated Bouc-Wen model with a linear stiffness relationship for the Isolator RPA1. a) Measured force time history and b) hysteresis curve.

Table 5.11. Estimated values for the Bouc-Wen model with a linear stiffness relationship for the Isolator RPB2.

A	n	γ	β	k_0	α
$\mathbf{1.6803e+00}$	$2.6644e+00$	$-4.4816e+05$	$5.5680e+05$	$2.5172e+05$	$2.5229e-01$

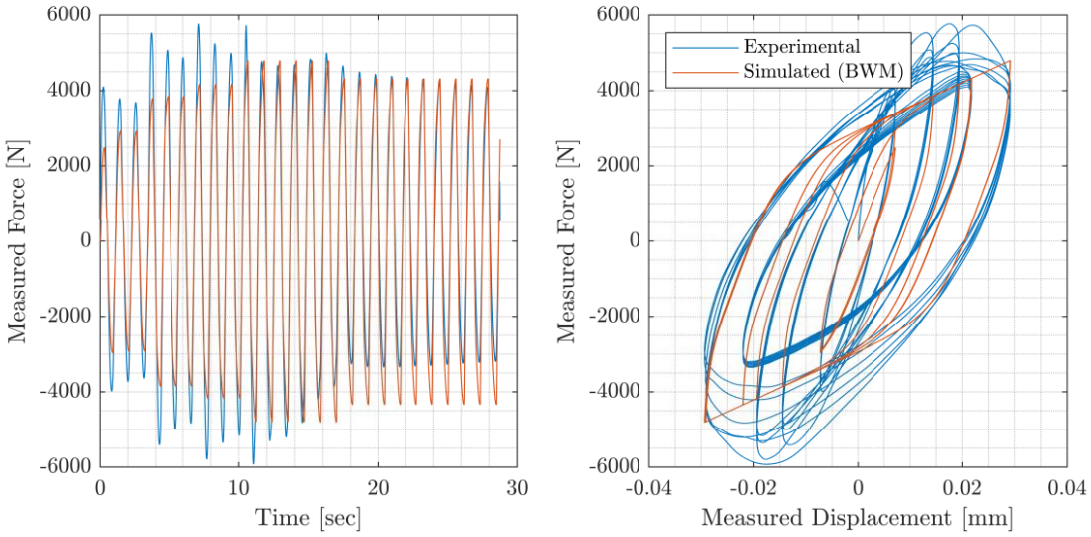

Figure 5.11. Fitting of the estimated Bouc-Wen model with a linear stiffness relationship for the Isolator RPB2. a) Measured force time history and b) hysteresis curve.

Table 5.12. Estimated values for the Bouc-Wen model with a linear stiffness relationship for the Isolator RPC9.

A	n	γ	β	k_0	α
$\mathbf{8.6362e-01}$	$2.5888e+00$	$-5.2228e+04$	$1.0058e+05$	$3.4588e+05$	$2.8531e-01$

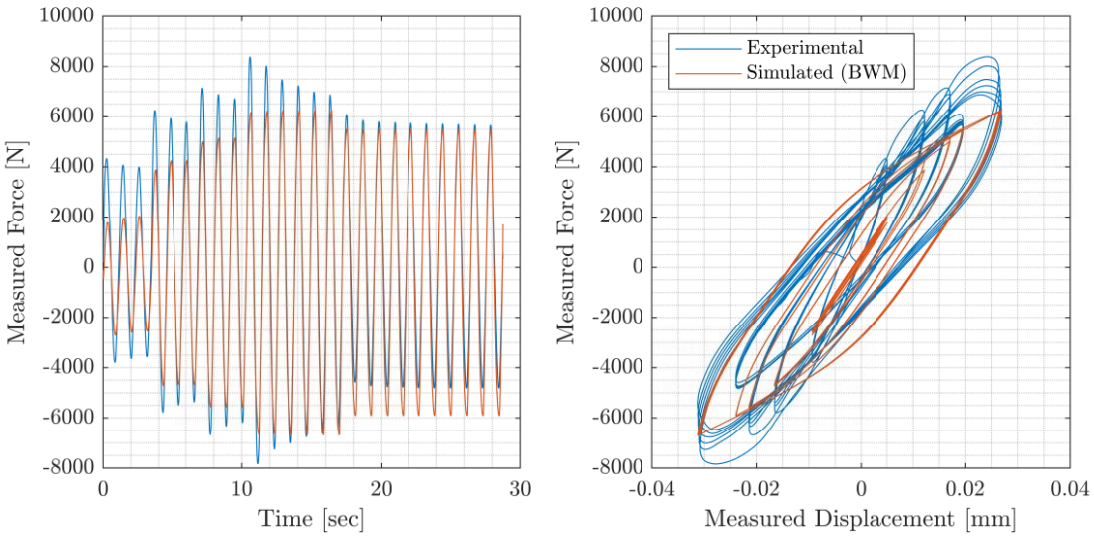

Figure 5.12. Fitting of the estimated Bouc-Wen model with a linear stiffness relationship for the Isolator RPC9. a) Measured force time history and b) hysteresis curve.

From the parameter estimation results, it is observed that the fifth-order polynomial model fits better the overall hysteretic behavior of the isolators than the model with a first-order polynomial. This result is due to the fact the fifth-order model accounts for the hardening and softening of the specimen and for the force asymmetry present in the isolator's response. The fifth-order model presented a better fit, particularly for the isolators NCA1 and NPA1. The hysteretic behavior for the rest of the isolators is highly nonlinear, varying from a phase with softening and hardening to a phase where these effects decrease in intensity and the dissipated area increases for the greater cycles. This change in behavior can be attributed to damage suffered by the isolator during the larger amplitude cycles. Some of the damages include the isolators breaking due to shear deformations or the outer layers of the isolators degrading due to friction. Since these isolators were stiffer than the NCA1 and NPA1, they were not able to withstand high deformations and deform to develop softening and hardening effects. For these reasons, the Bouc-Wen models of 5^{th} and 1^{st} orders for the isolators NCA1 and NPA1 were selected to be part of the virtual model of the plant that is going to aid in the design of a controller.

6. DESIGN OF THE CONTROL SYTSEM AND TRACKING PERFORMANCE

This chapter presents the steps taken to develop a controller for the RTHS system. Section 6.1 presents a preliminary assessment of the time delay in the signal caused by the inherent dynamics of the transfer system and Section 6.2 shows the experimental validation of the selected delay compensator. Lastly, Section 6.3 describes the tuning of a PI controller to account for amplitude differences in the tracking of the desired signal.

6.1 Preliminary assessment

Any signal that is sent to the transfer system gets distorted due to its inherent dynamics. Some of these distortions include amplitude changes, time delays, frequency distortions due to the oil-column resonance, and harmonic distortions due to the nonlinearities in the servo valve. The first two types of distortions are shown in the magnitude and phase response functions in Figure 4.3, which show the variation of the response of the transfer system for different frequencies. The last two types of distortions were addressed in Section 2.4.1.

The inherent delay present in the transfer system is of approximately 27 milliseconds for a sine wave of 1 Hz and 10 mm of amplitude, 86 ms at 3 Hz, and 72 ms at 10 Hz. As shown in Section 2.4.1 this delay is close to the critical time delay that would negatively affect the stability of the partition. Since the critical time delay is 35 ms, the transfer system will remain stable, although the delay will be reflected as a negative damping that is being added into the system, thus making the system develop greater amplitudes. This effect can be simulated in the model presented in Figure 2.5, where the displacement response of the base floor of the structure increases significantly for a delay of 35 ms as shown in Figure 6.1. The signal sent to the system corresponds to the Campano Lucano 290ya (CAM) ground motion (Calabrese, Spizzuoco, Serino, Della Corte, & Maddaloni, 2015) with an intensity of 50% which was one of the signals that were used to test the specimens at the University of Naples Federico II (Magliulo, et al., 2012), the acceleration time history and spectra of this ground motion is shown in Figure 6.2.

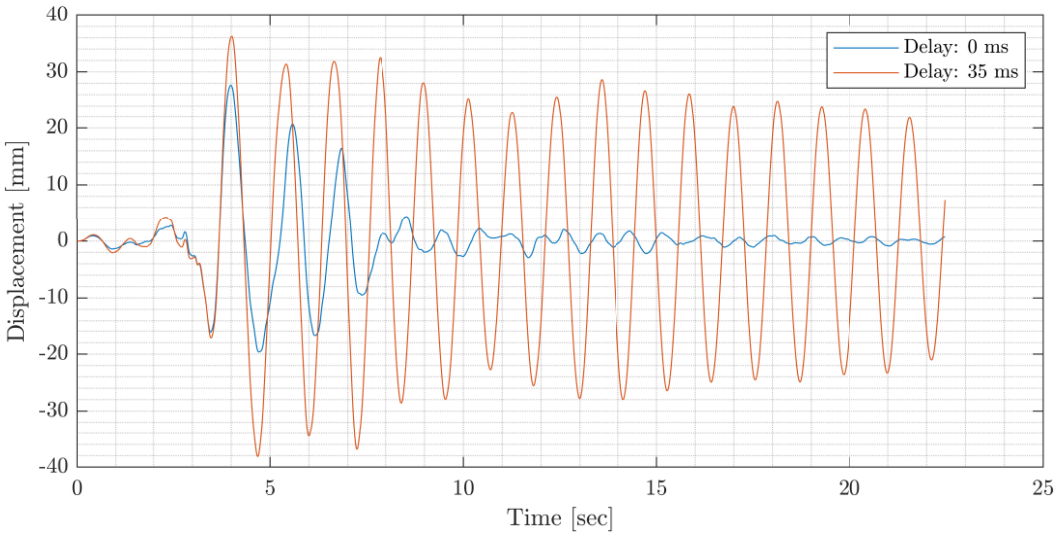

Figure 6.1. Increase in displacement due to the added delay.

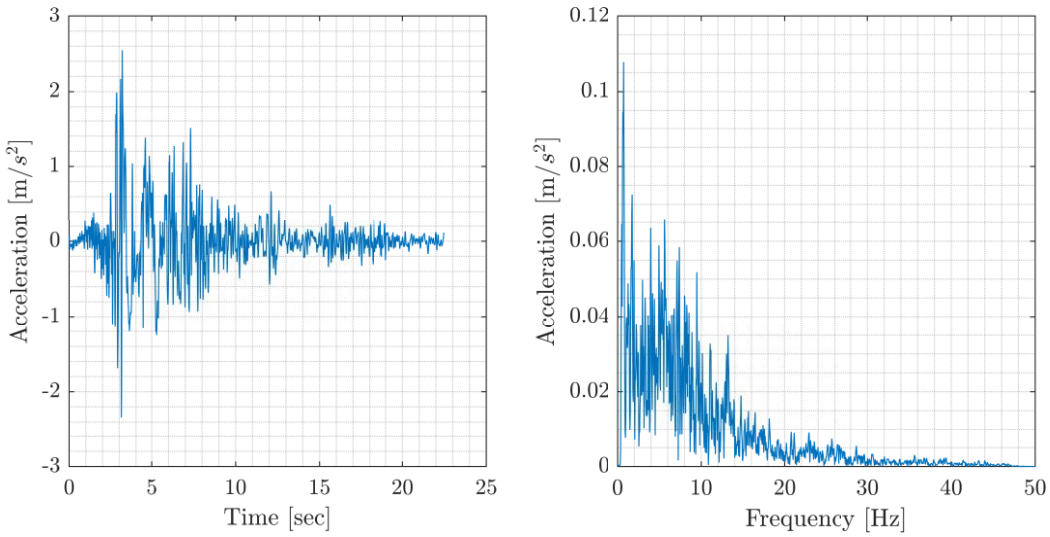

Figure 6.2. Campano Lucano 290ya (CAM) ground motion, a) acceleration time history (left) and b) spectra (right).

This effect can be experimentally demonstrated with the experimental setup shown in Section 2.4, given that the partition remains stable with delays that the transfer system exhibited at increasing frequencies. Figure 6.3 shows the same ground motion sent to the numerical substructure shown in Figure 2.5, but this time delay will be dictated by the delay in the transfer system and the experimental substructure will be represented by the isolators itself. This response

was controlled to remain within the operational limits of the setup by reducing the intensity of the ground motion to 33% and amplifying feedback restoring force from the isolation layer 2.5 times the measured force. It is observed in Figure 6.3 that this response is similar to the delayed signal shown in Figure 6.1 when representing the transfer system as a pure time delay system. Therefore, the first step to be taken to control the RTHS system is to compensate for the delay in the system.

Many delay compensation techniques have been developed over the years (Carrion, Spencer, & Spencer, 2007), and some of them model the transfer system as if it only introduces a time delay to the signal sent to the transfer system (Chen & Ricles, 2009). Others have developed adaptive techniques to account for cases where the delay is not constant through the simulation (Chae, Kazemibidokhti, & Ricles, 2013).

The inverse compensation (IC) technique (Chen & Ricles, 2009) assumes a simplified first-order discrete transfer function to represent the dynamics of the servo-hydraulics system. In that sense, the measured displacement will be equal to:

$$d_m^i = d_m^{i-1} + \frac{1}{\alpha \cdot \delta t}\left(d_c^i - d_m^{i-1}\right) \cdot \delta t. \tag{6.1}$$

Here, the measured displacement of the current step (d_m^i) will be extrapolated with a slope equal to the difference between the current displacement that was sent to the transfer system (d_c^i) and the measured displacement of the previous step (d_m^{i-1}) divided by the time that it takes for the measured displacement to be fed back the integration algorithm ($\alpha\delta t$). The variable α is an integer greater than one and δt is the time step increment that takes the value of 1/4096 sec throughout our experiment. By applying the discrete z-transform to Equation (6.1) we obtain a transfer function that takes the command displacement sent to the transfer system and outputs the measured displacement:

$$\frac{X_m(z)}{X_c(z)} = \frac{z}{\alpha \cdot z - (\alpha - 1)} \tag{6.2}$$

where $X_m(z)$ is the discrete z-transform of d_m^i and $X_c(z)$ is the discrete transform of d_c^i. Applying the inverse model principle to Equation (6.2) leads to the following transfer function:

$$\frac{X_p(z)}{X_c(z)} = \frac{\alpha \cdot z - (\alpha - 1)}{z} \tag{6.3}$$

where $X_p(z)$ is the discrete z-transform of the predicted (or compensated) displacement that is going to be sent to the transfer system. The time domain form of Equation (6.3) can be obtained by applying the inverse discrete z-transform on it, symbolically:

$$d_p^i = \alpha \cdot d_c^i - (\alpha - 1) \cdot d_c^{i-1}. \tag{6.4}$$

The variable α in Equation (6.4) represents the delay in the system that the function will compensate, this parameter is tuned in accordance with the amount of delay that the system exhibits. The delay in milliseconds will be the product of α and the time step δt.

The phase lead compensator (PLC) is a compensator that takes on the same definition expressed in Equation (6.1), but calculates the weighted average of the command (d_{avg_c}) and measured displacements (d_{avg_m}) to calculate the slope for the extrapolation (Chen & Tsai, 2013), as given by:

$$d_m^i = d_m^{i-1} + \frac{1}{\alpha \cdot \delta t}\left(d_{avg\_c}^i - d_{avg\_m}^{i-1}\right) \cdot \delta t \tag{6.5}$$

where:

$$d_{avg\_c}^i = \frac{W_1 \cdot d_c^i + W_2 \cdot d_c^{i-1} + d_c^{i-2}}{W_1 + W_2 + 1} \tag{6.6}$$

and

$$d_{avg\_m}^i = \frac{W_1 \cdot d_m^i + W_2 \cdot d_m^{i-1} + d_m^{i-2}}{W_1 + W_2 + 1} \tag{6.7}$$

In the previous expressions, d_m^{i-2} and d_c^{i-2} are the measured and commanded displacements at the $(i-2)$th step. W_1 and W_2 are the averaging weights that need to be calibrated for each application. By substituting Equation (6.7) and (6.6) into Equation (6.5) and taking the discrete z-transform we obtain the following transfer function that relates the measured and the command displacements:

$$\frac{X_m(z)}{X_c(z)} = \frac{W_1 \cdot z^2 + W_2 \cdot z + 1}{[W_1 + (W_1 + W_2 + 1)\alpha] \cdot z^2 + [W_2 - (W_1 + W_2 + 1)\alpha] \cdot z + 1} \tag{6.8}$$

Applying the inverse model principle on Equation (6.8) leads to the following transfer function:

$$\frac{X_p(z)}{X_c(z)} = \frac{[W_1 + (W_1 + W_2 + 1) \cdot \alpha] \cdot z^2 + [W_2 - (W_1 + W_2 + 1) \cdot \alpha] \cdot z + 1}{W_1 \cdot z^2 + W_2 \cdot z + 1} \tag{6.9}$$

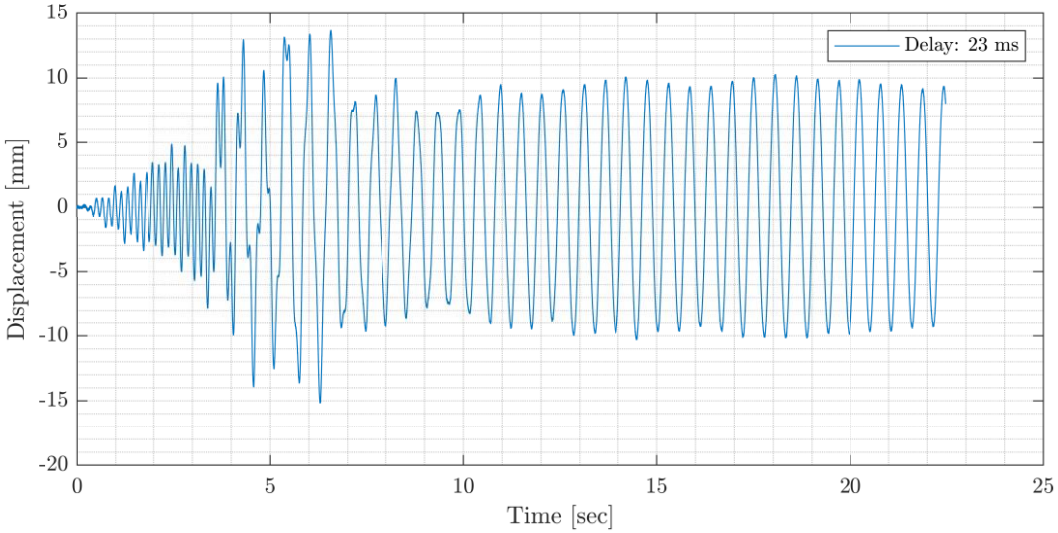

Figure 6.3. Base plate displacement due to the CAM ground motion and with transfer system delay.

6.2 Experimental validation

The PLC delay compensator was tested experimentally on a series of open loop tests with the bare plate with an input sine wave of 5 mm at 1 Hz with a duration of 30 seconds.

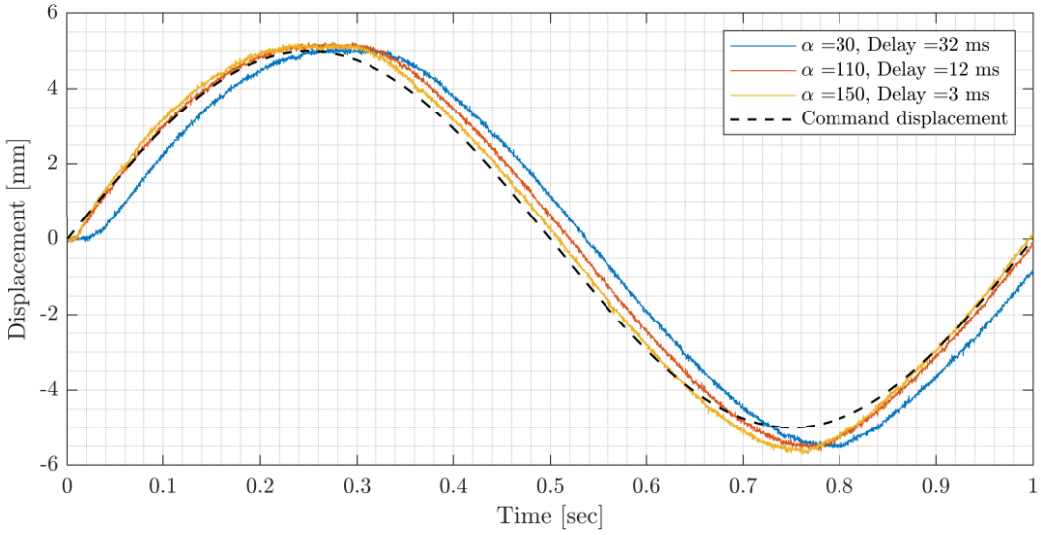

Figure 6.4. Measured displacement with PLC delay compensation technique.

Figure 6.4 shows the positive effect of the delay compensator on the measured signal. The PLC compensated approximately 36 ms leaving the signal with only 3 ms of delay. As is clear from the figure, the compensation of the delay is not linear as the delay in the system increases with the compensation parameter α. The figure also exhibits an increase of amplitudes as the delay increase, this change is also evidenced in Figure 6.5 where the average slope of the curves starts to decrease as the compensation increases.

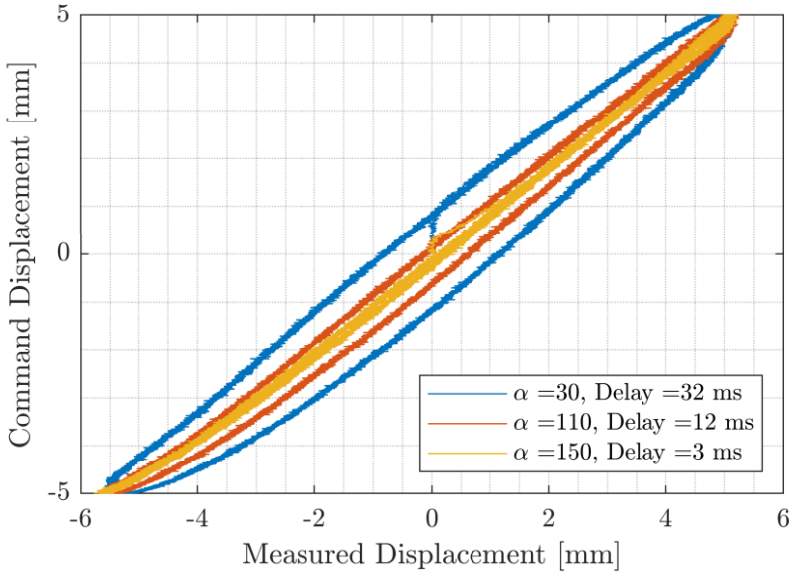

Figure 6.5. Measured displacement vs command displacement with PLC delay compensation technique.

A detrimental effect of the filter on the measured signal and on the system is shown in Figure 6.6, where the measured force shows a high amplitude force at the beginning of the measurement. These amplitudes and oscillations seem to increase with the compensation parameter α and the high amplitude force signal seems to belong to a high-frequency range. After a low-pass filter with a cutoff frequency of 60 Hz was applied to the force signals, these high-frequency and high-amplitude forces were removed, and the force time histories looked similar in magnitude relative to each other. These measurements suggests that the PLC was exacerbating the oil-column resonance of the system. The spectra for the force signals with the compensator show these frequencies with higher magnitudes than the ones for the uncompensated signal.

The PLC delay compensator computes the predicted displacement at the current time step from the averages of the command and predicted signal from the n^{th} , $(n-1)^{th}$, and $(n-2)^{th}$ time steps, therefore the noise that the command signal could contain will be intensified and sent to the transfer system where it will resonate with the oil-column frequency of the system. If the input signal is not contaminated with any high-frequency noise, this identification will not happen. However, in an RTHS there is a high probability that the command displacement sent to the transfer system would be contaminated with high-frequency noise contained in the measured force that is feedback to the numerical substructure. In some cases, the numerical substructure would act as a low-pass filter and decrease the intensity of this high-frequency noise. However, this will depend on the ability of the numerical substructure to act as a low-pass filter.

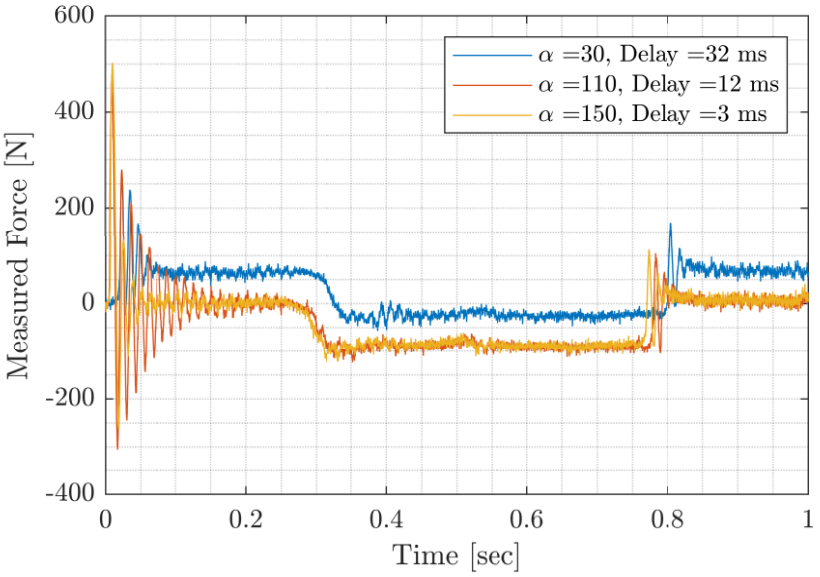

Figure 6.6. Measured force time history with PLC delay compensation technique.

The IC technique was implemented on a series of sinusoidal open loop tests on the bare plate with an input sine wave of 10 mm at 1 Hz with a duration of 30 seconds. The compensator parameter, α, was incremented from 0 to 110 and a section of the time history of the measured displacement is shown in Figure 6.7. There is an incremental reduction on the delay between the measured and the command signal with a better delay compensation than the one achieved with the PLC. Figure 6.7 shows that the measured displacement signal is moving left as the parameter α increases. When comparing the commanded signal and the measured signals for $\alpha = 0$ and $\alpha =$

110, it is observed that the compensation effectively reduces the delay between the command signal (black dashed line) and the measured signal (yellow line). The difference in amplitude between the uncompensated signal and the command displacement is less than the one between the compensated signal and the commanded signal, where the uncompensated signal maximum displacement was 10.16 mm and for the compensated signal was 10.38 mm. This result suggests that the IC technique had an influence on the amplitude of the command displacement. Without the delay compensator, the measured amplitude was more similar to the command signal but with a significant delay. However, with delay compensation, the difference between the command and measured signals amplitudes had a smaller increase, but now with a very small delay.

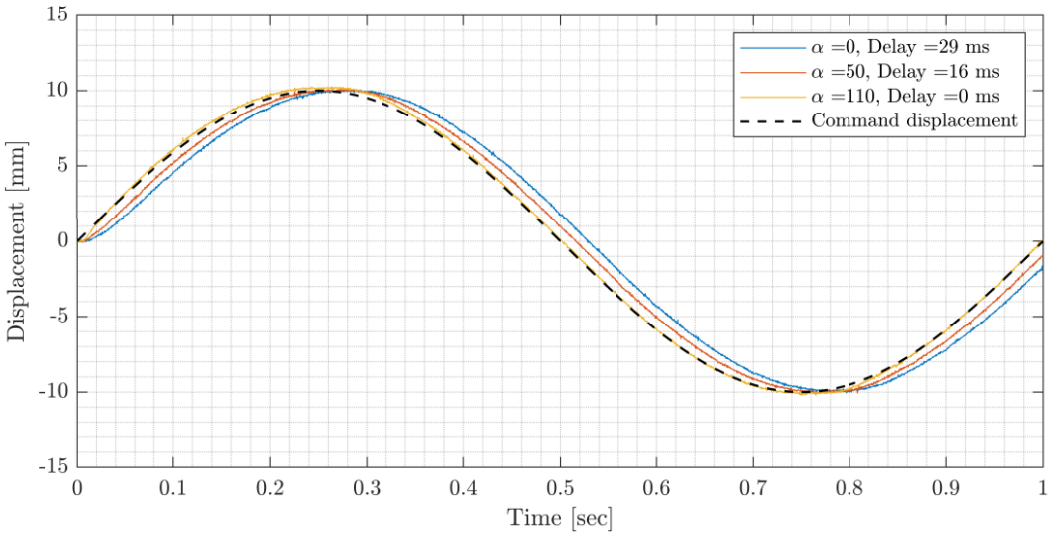

Figure 6.7. Measured displacement with IC delay compensation technique.

Figure 6.8 shows the measured displacement plotted against the command displacement. This figure shows the graph transitions form an oval shape to a linear relationship when the delay was compensated. It is also observed that the slope of the compensated signal is relatively smaller than the average slope of the uncompensated graph, this represents the slight amplitude change due to the implementation of the delay compensator.

The spectra of the measured displacement signal confirm the increase in amplitude, and it also exhibits an amplification in the noise amplitude. However, the noise base level seems lower than the spectra for the uncompensated displacement signal. Harmonic distortion is still present

for both spectra, and particularly at lower frequencies where peaks appear every 1 Hz up to 20Hz and after 20 Hz, they appear every 10 Hz. These harmonic distortions are more prominent in the force spectra since it depends on the acceleration, the same can be say for the oil-column resonance.

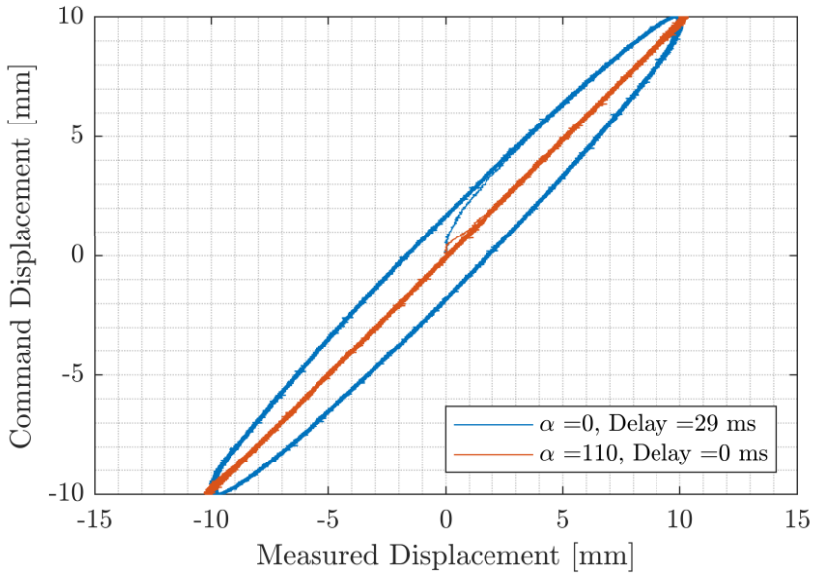

Figure 6.8. Measured displacement vs command displacement with IC delay compensation technique.

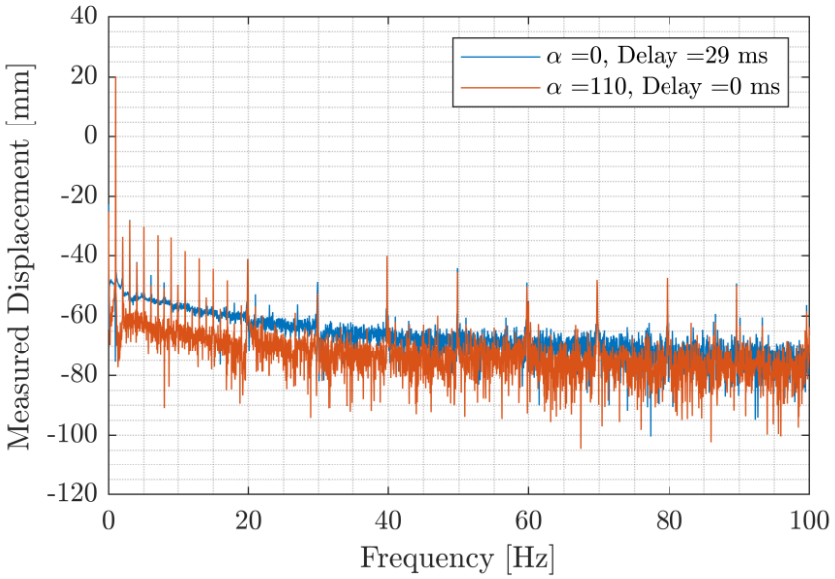

Figure 6.9. Spectra of the measured displacement with and without delay compensation.

The force time history shown in Figure 6.10 still shows signs of high forces being developed at the beginning of the signal as seen in Figure 6.6, but with fewer oscillations.

The IC technique showed a better compensation with a lesser effect on the measured displacement and force signals when compared to the PLC technique. Therefore the IC technique will be used to compensate for the delay in the transfer system.

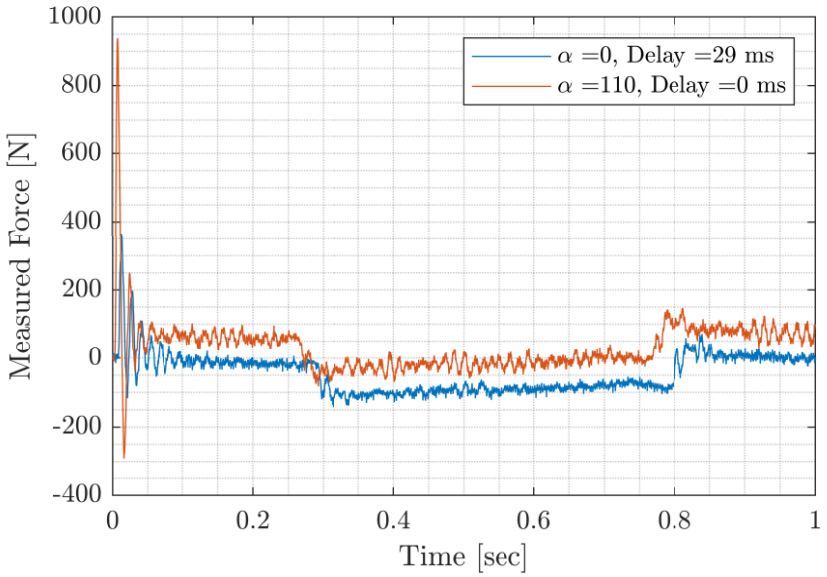

Figure 6.10. Measured force time history with IC delay compensation technique.

6.3 PI controller tuning

Since the difference between the command and measured displacements is small, the compensation was performed by tuning a proportional and integral tracking controller, a derivative function was excluded to minimize the intensification of the high-frequency noise from the force feedback loop.

The tuning process starts with the assembly of the reference case that is assumed as analogous to the ideal behavior of the isolated structure presented in Figure 2.2, when subjected to a ground motion. The numerical substructure model corresponds to the substructuring, and state space model described in Section 2.1.1. The physical substructure corresponds to the isolation layer represented by the Bouc-Wen model of first-order estimated for the isolator NPA1 in Section 5.2. The excitation sent to the system corresponds to the Campano Lucano 290ya (CAM)

ground motion with an intensity of 50%. A block diagram of the reference model is shown in Figure 6.11. Once the measured displacements for the upper and lower slabs, and the measured shear force at the level of the isolation layer have been recorded from the reference case, the RTHS case is implemented.

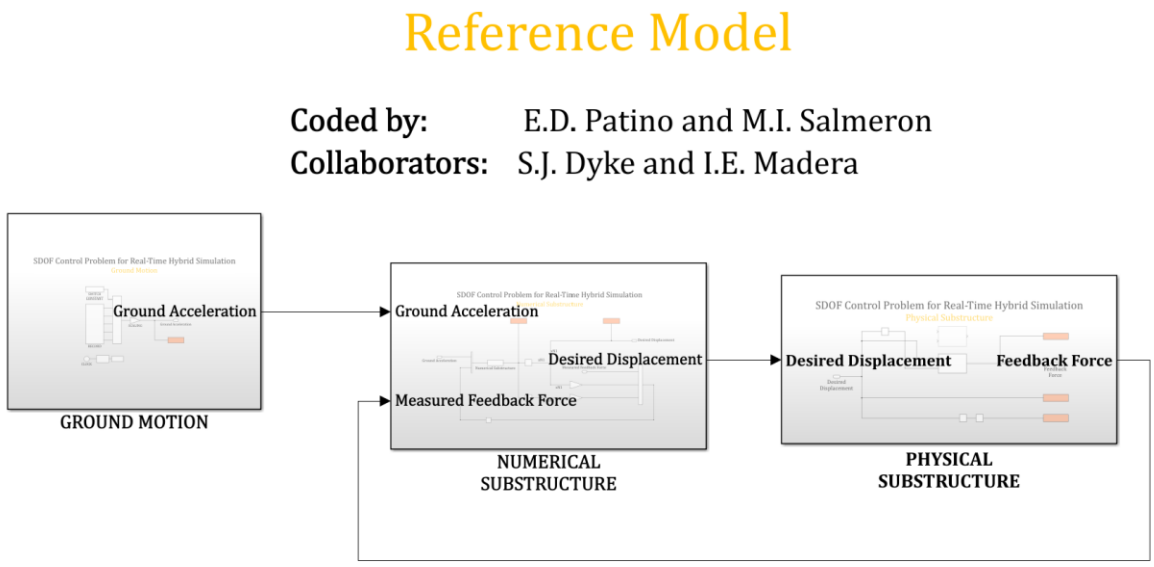

Figure 6.11. Block diagram of the reference case for the base isolated structure presented Figure 2.2.

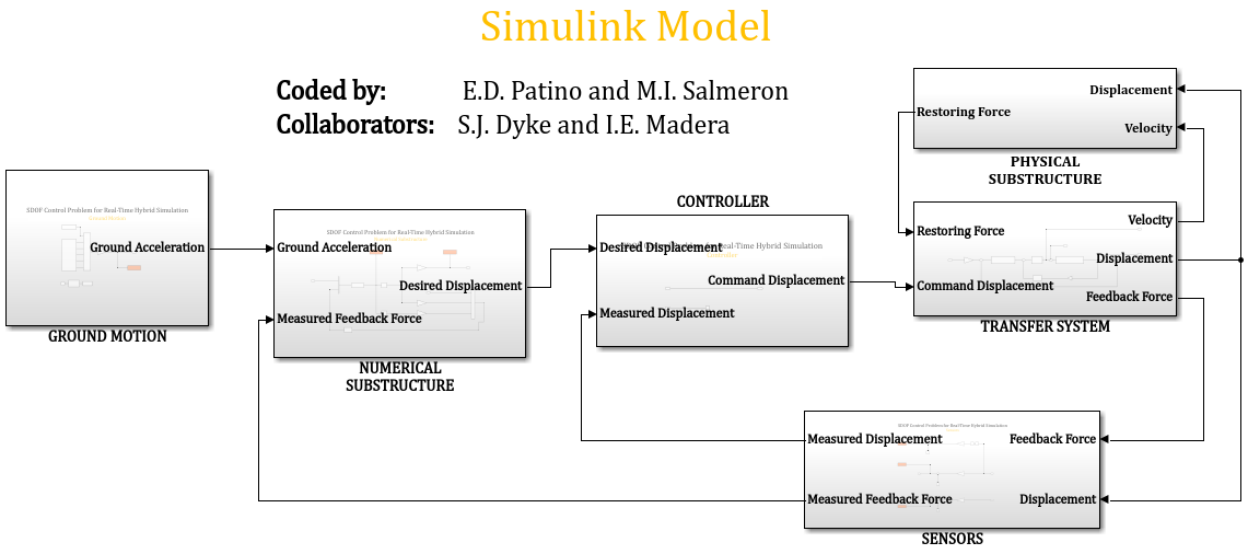

Figure 6.12. Block diagram of the RTHS case for the base isolated structure presented Figure 2.2.

The control and transfer systems are added to the block diagram in Figure 6.11, as shown in Figure 6.12. The transfer system block contains the model described in Section 4.2. The proportional and integral gains were tuned by running the simulation with different gain values and selecting the gains that produced the lowest RMSE between the measured and reference displacement signals. The result of this analysis is presented in Figure 6.13, and the final tuned values for the P-gain and I-gain are given in Table 6.1. During the tuning process, it was observed that the time delay decreased when the integral gain increased, thus, to help the tunning of the PI controller gains, the parameter alpha was set at $\alpha = 30$ which was enough to compensate for the time delay of the virtual transfer system which had a value of 86 milliseconds down to 0.5 milliseconds. The base floor displacement tracking and measured shear force at the floor level are plotted in Figure 6.14 and Figure 6.15, respectively. The RMSE shows a good tracking was achieved with the tuned gains, as shown in Figure 6.14. The shear force is the most affected due to its sensitivity to high-frequency noise and the oil-column resonance influence that is amplified by the delay compensator. Figures 6.16 through 6.18 show the response of the virtual simulation for different ground motion input signals, the most evident characteristic shown in these figures is that the partitioned system seems to better adjust to the unpartitioned system for small displacement. However, at large displacements the RMSE between the two signal increases.

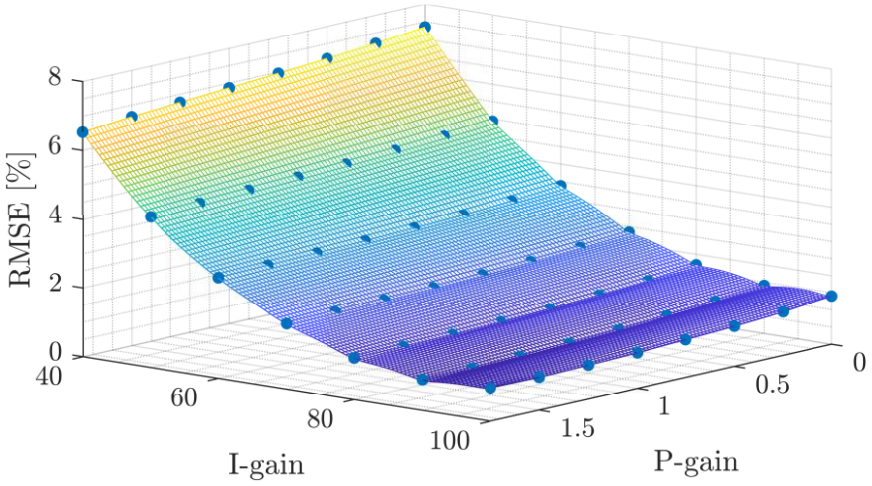

Figure 6.13. Tuning process of the gains for the PI controller.

Table 6.1. Tuned values for the PI controller and delay compensator.

P	I	α	$RMSE$	$Delay$
1.75	90	30	0.9%	0.5 ms

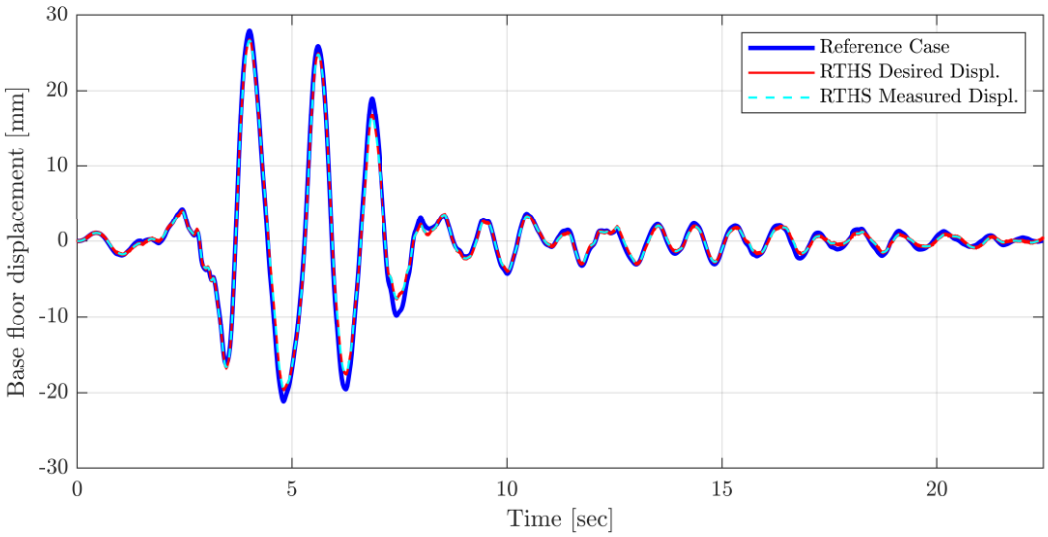

Figure 6.14. Base floor displacement comparing the reference unpartitioned case and the controlled partitioned case.

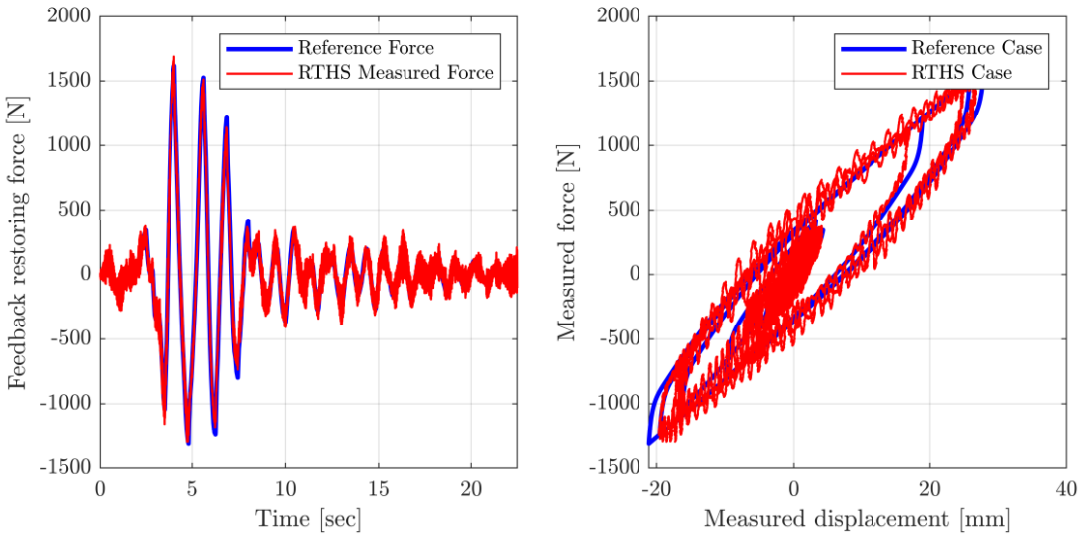

Figure 6.15. Shear force at the base floor level comparing the reference unpartitioned case and the controlled partitioned case.

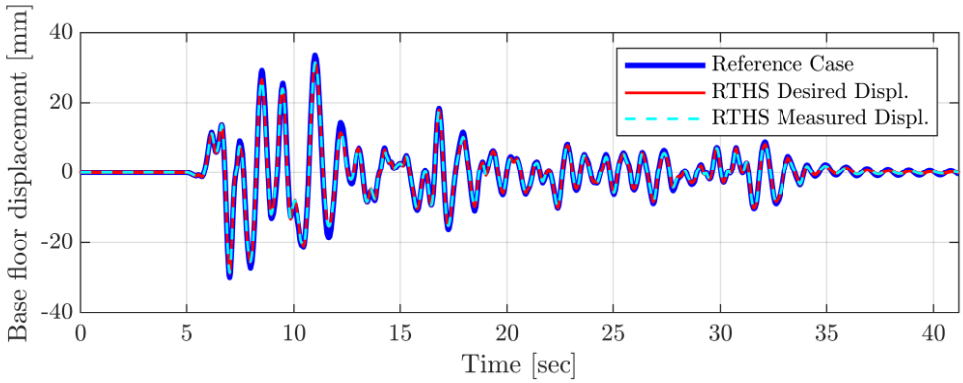

Figure 6.16. Base floor displacement comparing the reference unpartitioned case and the controlled partitioned case for El Centro 1940 ground motion.

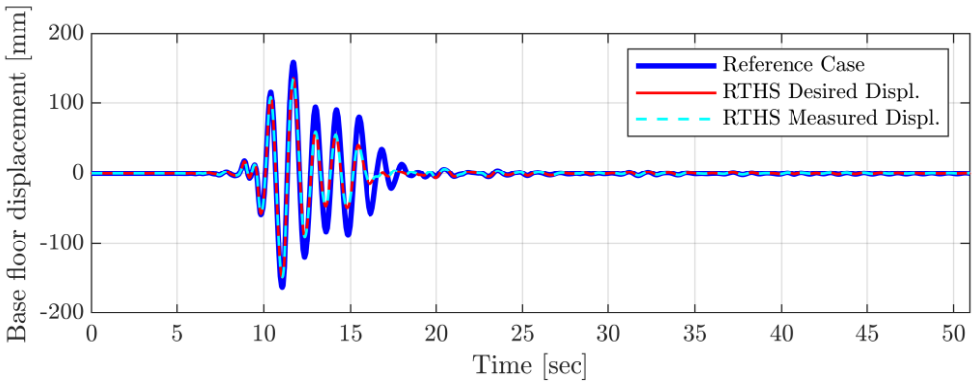

Figure 6.17. Base floor displacement comparing the reference unpartitioned case and the controlled partitioned case for Kobe 2005 ground motion.

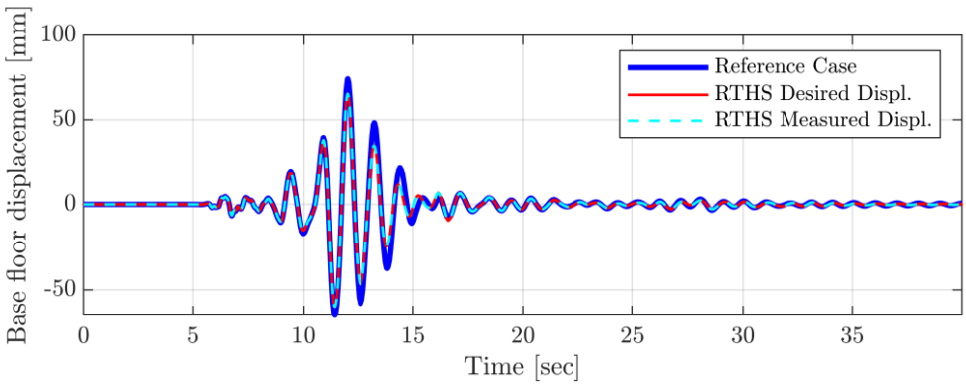

Figure 6.18. Base floor displacement comparing the reference unpartitioned case and the controlled partitioned case for Morgan Hill 1984 ground motion.

7. VIRTUAL MODEL OF THE RTHS SYSTEM

A code package was created for all students and users interested in learning the applications of RTHS of a base-isolated structure with a nonlinear component as it is a rubber isolator. This package contains the models presented in this work as well as selected experimental data that was collected in the laboratory. This package offers the possibility for the user to implement different types of models either for the controller, transfer system, or to model the complex nonlinear behavior of the specimens. The numerical structure as presented in Section 2.1.1 could also be modified to include more stories and the Simulink model can include filters or introduce uncertainties into the simulation.

This code package is prepared for new members in the RTHS community, or anyone interested to learn the first steps taken to structure an RTHS experiment and the different considerations that must be taken to account for common issues that may emerge during an RHTS. The following sections in this chapter describe the files and details of this code package.

7.1 Simulation tool

The code package consists of three folders that contain the materials and experimental data that are available to run the virtual model of the RTHS experiment, namely, '01_Documentation', '02_SimulationTool' and '03_Data'. In this section, the contents of the provided materials are described below:

- 01_GroundMotions: contains a set of five unscaled acceleration time history data available to run the simulation: El Centro 1940, Kobe 2005, Morgan Hill 1984, Campano Lucano 1980 (CAM), and a sine input signal for verification purposes.
- 02_Models: contains the actuator-servo-hydraulics, shake plate, and specimen model parameters that will be used in the simulation.
- 03_Results: contains the simulation results as .mat files.
- SDOF_vRTHS.m: MATLAB script that computes the simulation and model parameters, numerical matrices, and the state-space matrices of the numerical substructure.
- SDOF_vRTHS_SIMULINK.slx: Simulink file for the simulation.

- SDOF_vRTHS_REFERENCE.m: MATLAB script that computes the output signals corresponding to the reference model which will serve as a baseline for comparison.
- SDOF_vRTHS_REFERENCE_SIMULINK.slx: Simulink file for the reference model.
- SDOF_vRTHS_EXAMPLE_SIMULINK.slx: Simulink file for a controller implementation example.

A series of constraints were adopted based on the physical limitations of the experimental hardware and software used in the laboratory and used in the Simulink model.

The simulation tool, `SDOF_vRTHS.m`, is a MATLAB script that computes the transfer system, control, and specimen model parameters as well as the reference and numerical structure parameters needed for the simulation. This script calls the Simulink model, `SDOF_vRTHS_SIMULINK.slx`, to execute the simulation, which is shown in Figure 7.1. When the simulation is completed, the results are plotted on the main script and the evaluation criteria are calculated.

The MATLAB script, `SDOF_vRTHS_REFERENCE.m`, creates the reference system by computing the superstructure and isolation layer parameters and calls the Simulink model, `SDOF_vRTHS_REFERENCE_SIMULINK.slx`, to run the simulation. This subroutine is run by the main script, `SDOF_vRTHS.m`, and the results are stored in the '03_Results' folder.

The Simulink model, `SDOF_vRTHS_SIMULINK.slx`, consists of a series of simulation blocks with a similar arrangement as the flow diagram presented in Figure 2.3, and described in Section 2.2.1. The ***ground acceleration*** block prepares the type and intensity of the input signal that is sent to the numerical substructure. The ***numerical substructure*** block contains the state-space representation presented in Section 2.1.1, where the desired displacement of the base slab is computed. The desired displacement is sent to the ***control system*** block, where the controller calculates the command displacement. The servo-hydraulic system will receive this commanded displacement and, along with the actuator dynamics and the properties of the specimen, exert a force on the sliding table and a displacement will occur. The force and displacement signals will be measured by the corresponding transducers where sensor noise contamination can occur, represented by the ***sensors*** block, before feeding back to the numerical substructure block and the control system block, respectively.

An example of a controller implementation is provided in the file `SDOF_vRTHS_EXAMPLE_SIMULINK.slx`. The user can execute this model by setting the `model_choice` variable to 2. If such variable is left as 1 (default), then the uncontrolled case model, `SDOF_vRTHS_SIMULINK.slx`, is executed. Users can modify this model with their own controllers.

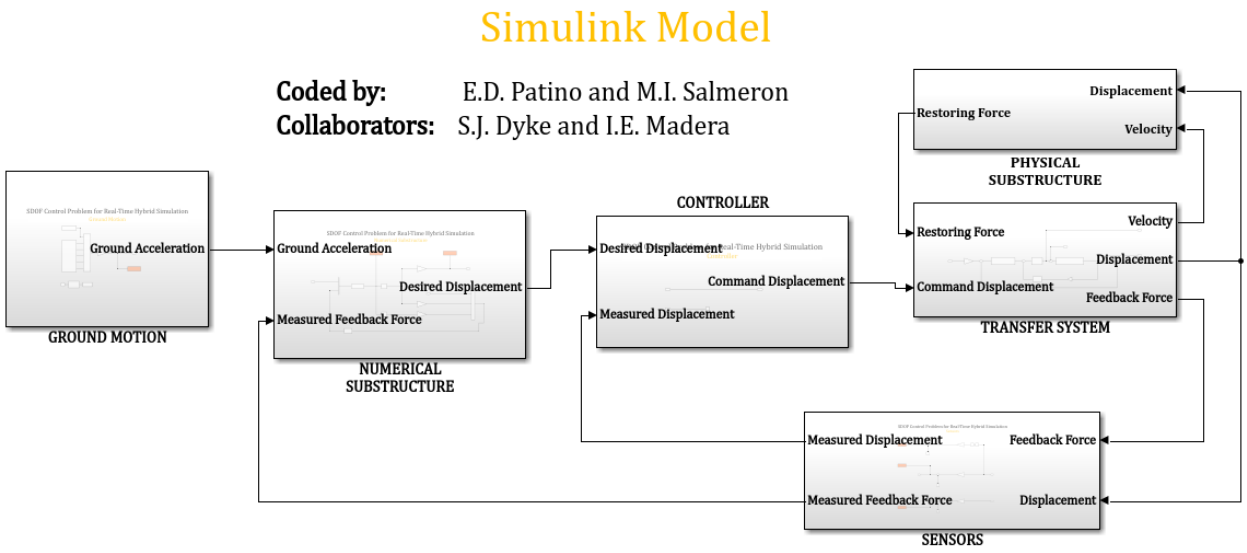

Figure 7.1. Simulink file '`SDOF_vRTHS_SIMULINK.slx`' that runs the simulation.

7.2 Experimental data

A set of experimental data is provided as MATLAB .mat files in the folder '03_Data' for those users who aim to model the physical substructure or transfer system through an alternative approach.

The isolators that were selected to be the focus of this code package are the **NCA1** (**N**atural rubber with a **C**arbon fiber reinforcement) and the **NCA1** (**N**atural rubber with a **P**olyester fiber reinforcement) isolators. The suffix A1 refers to a naming convention adopted for recordkeeping purposes.

These signals were sent to the sliding table in an open loop without any control system. The '03_Data' folder includes:

- **01_BarePlate:** includes a set of BLWN, chirp, and sinusoidal signals for the sliding table without a specimen.

- **02_SpecimenNCA1:** includes a set of ramp, step, sine, and shear test protocol (ASCE 7-16 SEC. 17.8.2.2-2.a) signals sent to the sliding table with the specimen NCA1 on it.
- **03_SpecimenNPA1:** contains the same type of signals as for '02_SpecimenNCA1', but in this case for the specimen NPA1.

The variable names in the .mat files as described as follows:

- **am**: acceleration signal measured at the sliding table in mm/s^2.
- **dd**: desired displacement, $x_n^{(1)}$, sent to the sliding table in mm.
- **dm**: measured displacement, x_m, of the sliding table in mm.
- **fm**: measured force, f_m, exerted by the actuator in N.
- **dt**: simulation time increment in sec.
- **t**: time vector in sec.

7.3 Implementation constraints

A series of constraints were adopted based on the physical limitations of the experimental hardware and software used in the laboratory and used in the Simulink model.

1) The sampling frequency of the simulation, f_s, is 4096 Hz.
2) The MATLAB script and the Simulink model were written in version R2022a.
3) The time delay associated with the design of the controller should be of less than 10 ms, or less than the critical time delay for it not to hinder the stability of the partition.
4) The motion of the actuator throughout the virtual experiment should not exceed the physical capacities of the setup, i.e., the actuator should not surpass neither a maximum stroke of ±60 mm, a maximum force of 8800 N, nor a maximum velocity of 300 mm/s.
5) The measurement noise is modeled as a normally distributed random number with a correlation time equal to the sampling period. The noise power (RMS) was estimated from experimental data.

8. RTHS OF A BASE ISOLATED STRUCTURE

This chapter is devoted to describing the implementation of the RTHS experiment in the laboratory. Section 8.1 describes the evaluation criteria adopted to assess the tracking accuracy and overall RTHS performance. Section 8.2 presents the results obtained from the simulation.

8.1 Evaluation criteria for control

Evaluation criteria are established in this section to assess the suitability and tracking control performance of the control system (Silva, Gomez, Maghareh, Dyke, & Spencer, 2020). The evaluation is determined by a set of seven indicators that compare the measured, desired, and reference displacements. In this study, the real displacement records of the full-scale specimen are not provided. Thus, the reference model described in Section 2.1 will serve as the reference case. This comparison will give insight into how a purely numerical-parametric model of a structure can compare to a real-time hybrid simulation. The first three evaluation indicators measure how well the control system tracks the desired response of the numerical substructure. The last four indicators measure how well the measured response compares to the reference model.

The first evaluation indicator (J_1), determines the tracking time delay between the desired signal and the measured signal through cross-correlation by finding the amount of simulation time steps that the measured signal needs to be shifted to yield a maximum correlation between the two signals. A time step is the inverse of the sampling rate. The indicator is defined as:

$$J_1 = \arg\max_k \left(\sum_{i=1}^{n} x_n^{(1)}(i) x_m(i-k) \right) \tag{8.1}$$

It is implemented with the MATLAB function `finddelay` and reported in number of samples.

The second evaluation indicator (J_2), is the normalized root mean square (RMS) of the tracking error. Its value represents the difference between the desired and measured displacements, and it is given by:

$$J_2 = \sqrt{\frac{\sum_{i=1}^{n} \left[x_m(i) - x_n^{(1)}(i) \right]^2}{\sum_{i=1}^{n} \left[x_n^{(1)}(i) \right]^2}} \cdot 100\% \tag{8.2}$$

The third indicator (J_3), is the peak tracking error and its value is the maximum instantaneous error between the measured and desired displacements, and it was normalized by the maximum desired displacement. This indicator is defined as:

$$J_3 = \frac{\max\left|x_m(i) - x_n^{(1)}(i)\right|}{x_d^{(1)}(i)} \cdot 100\% \tag{8.3}$$

The fourth indicator (J_4), is the normalized root mean square error between the measured displacement and the displacement of the reference model measured at the base slab and it is given by:

$$J_4 = \sqrt{\frac{\sum_{i=1}^{n}\left[x_m(i) - x_r^{(1)}(i)\right]^2}{\sum_{i=1}^{n}\left[x_r^{(1)}(i)\right]^2}} \cdot 100\% \tag{8.4}$$

The fifth indicator (J_5), is the normalized peak tracking error found between the measured displacement and the displacement of the reference model at the base slab. This indicator is given by:

$$J_5 = \frac{\max\left|x_m(i) - x_r^{(1)}(i)\right|}{x_r^{(1)}(i)} \cdot 100\% \tag{8.5}$$

The sixth indicator (J_6), is the normalized root mean square error between the numerical displacement of the top slab obtained from the simulation and the top slab displacement of the reference model. This indicator is defined as:

$$J_6 = \sqrt{\frac{\sum_{i=1}^{n}\left[x_n^{(2)}(i) - x_r^{(2)}(i)\right]^2}{\sum_{i=1}^{n}\left[x_r^{(2)}(i)\right]^2}} \cdot 100\% \tag{8.6}$$

The seventh indicator (J_7), is the normalized peak tracking error between the numerical displacement of the top slab obtained from the simulation and the top slab displacement of the reference model measured. This indicator is given by:

$$J_7 = \frac{\max\left|x_n^{(2)}(i) - x_r^{(2)}(i)\right|}{x_r^{(2)}(i)} \cdot 100\% \tag{8.7}$$

In the previous expressions, the superscripts $[\dots]^{(1)}$ and $[\dots]^{(2)}$ indicate the DOF for the lower and upper floors, respectively. The subscripts $[\dots]_n$ and $[\dots]_r$ specify that the variable corresponds to a signal from the numerical or reference structure, and the subscript $[\dots]_m$ indicate that the variable corresponds to a signal measured experimentally.

These indicators use the response of the reference model presented in Figure 6.11 thus, intrinsic errors due to the underlying assumptions listed earlier are accounted for when analyzing the results.

8.2 RTHS performance

A real-time hybrid simulation was performed experimentally to test the response of the isolator under the loading it would experience in a large-scale test. The computational part of the simulation is formed by the Ground Motion, Numerical Substructure, and Controller blocks shown in the Simulink diagram in Figure 7.1. The transfer system is the experimental setup described in Section 2.4 and the experimental substructure is the isolator NPA1 which behavior is shown in Section 2.3. The acceleration time history sent to the system corresponds to the Campano Lucano 290ya (CAM) ground motion with an intensity of 50%. The same Simulink model shown in Figure 6.11 is used to compute a theoretical case where the numerical substructure and the behavior of the specimens are represented by the models developed in previous chapters of this work.

Both the 1st and 5th-order Bouc-Wen models estimated for the isolator NCA1 were selected to serve as the physical substructure in the virtual RTHS. The experimental parameters for the controller were tuned heuristically prior to the tests due to the uncertainties and nonlinearities not accounted for in the models that were developed but taking the estimated values in Chapter 6 as a starting point. The experimentally updated parameters are shown in Table 8.1.

Table 8.1. Experimentally updated gains for the PI controller and delay compensator.

Parameter:	P	I	α
Value:	1.90	70	41
Difference:	7.9%	22.2%	26.8%

The displacement and shear force were measured at the base floor level and compared between the RTHS case and the theoretical case, the seven evaluation criteria are calculated

between these two models and are shown in the displacement time history are presented in Figure 8.1.

Table 8.2. Evaluation criteria for the experimental RTHS and a virtual RTHS with a Bouc-Wen model of 5th order (isolator NPA1).

$J_1(ms)$	$J_2(\%)$	$J_3(\%)$	$J_4(\%)$	$J_5(\%)$	$J_6(\%)$	$J_7(\%)$
0	1.08	1.27	43.76	40.05	43.94	39.14

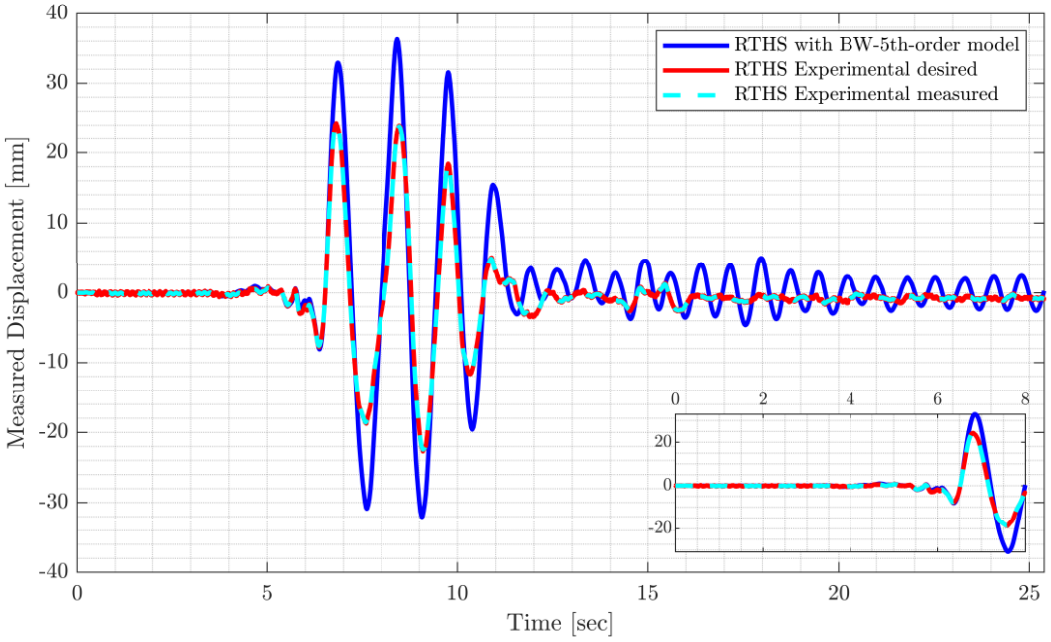

Figure 8.1. Measured base floor displacement comparison against a virtual RTHS with a Bouc-Wen model of 5th order (isolator NPA1).

Figure 8.1 shows a good tracking control between the measured and desired displacement signals with an RMSE of 1.08%, and this suggests that the control system performance is good. The experimental measurements show a greater difference in amplitude when it is compared against the RTHS experiment with the Bouc-Wen model of 5th order. This overestimation of the isolator response could indicate that the physical structure is stiffer, thus restricting the displacement of the base floor. After the 12-second mark, the virtual RTHS experiment shows higher displacements which were identified to be strongly related to the first mode of the structure. By applying the FFT to that portion of the signal, however, in the measured response from the experimental RTHS, these amplitudes are more related to the second mode of the structure. This

comparison suggest that the Bouc-Wen model drives the structure to respond mainly in its first vibrational mode, but in an RTHS there is certain influence from the second mode in the base floor displacement.

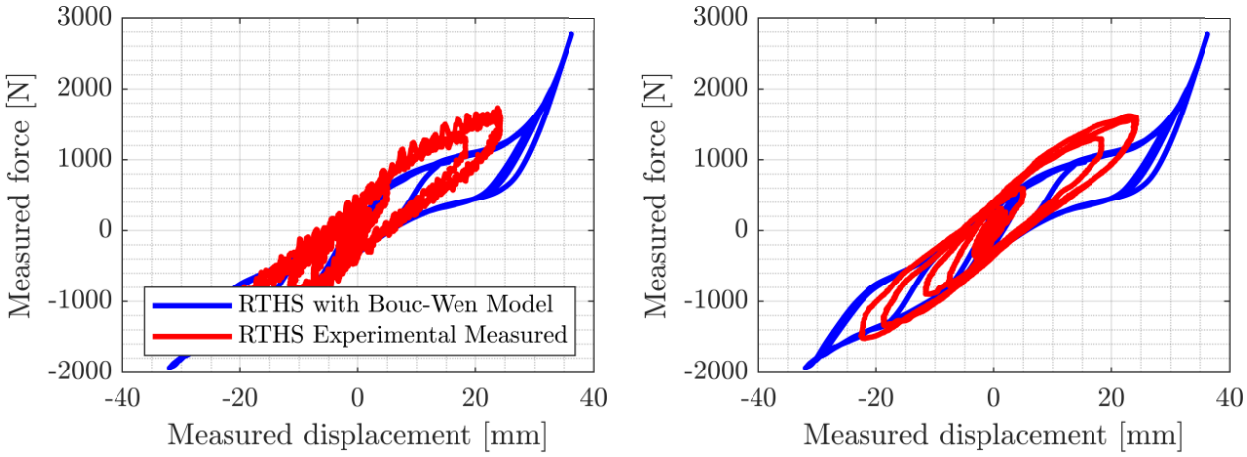

Figure 8.2. Measured shear force comparison with a virtual RTHS with a Bouc-Wen model of 5th order (isolator NPA1). a) unfiltered measured signal (left), filtered measured signal (right).

The experimental hysteretic behavior of the isolator is shown in Figure 8.2, where it is compared with the theoretical behavior given by the Bouc-Wen model of 5th order. The model is good at capturing the pinching effect around the origin that it is produced due to the softening (presented at around the +10 mm mark) and hardening (presented at around the +20 mm mark) of the isolator under small and large displacements, respectively. However, the model tends to overestimate the restoring forces at large displacements.

The comparison between the experimental RTHS against the virtual RTHS with a 1st order Bouc-Wen model is shown in Figure 8.3 and Figure 8.4. The response of the virtual RTHS approximates better the experimental response with smaller displacements. However, the forces developed differ from the experimental around the origin since this model does not account for changes in the tangent stiffness of the specimen. However, as shown in Table 8.3, the evaluation criteria did not worsen significantly due to the use of a Bouc-Wen model that does not account for different types of nonlinearities. On the contrary it seems to improve the evaluation criteria. We speculate that under an RTHS, the isolator is behaving more with fewer changes in its tangent stiffness that a simpler Bouc-Wen model is enough to represent the behavior of the isolator and will better predict the restoring forces of the isolator at the maximum displacements. The better

prediction of the forces generated at maximum displacement from this model seems to influence in a greater way the overall accuracy of the virtual RTHS when compared to its experimental counterpart, and the variations in the tangent stiffness, when perceived as softening or hardening of the material, do not affect the behavior significantly when their effects are not significantly pronounced in the hysteretic response of the isolators as shown in Section 5.2.

Table 8.3. Evaluation criteria for the experimental RTHS and a virtual RTHS with a Bouc-Wen model of 1st order (isolator NPA1).

$J_1(ms)$	$J_2(\%)$	$J_3(\%)$	$J_4(\%)$	$J_5(\%)$	$J_6(\%)$	$J_7(\%)$
0	1.08	1.27	33.37	32.75	33.57	32.44

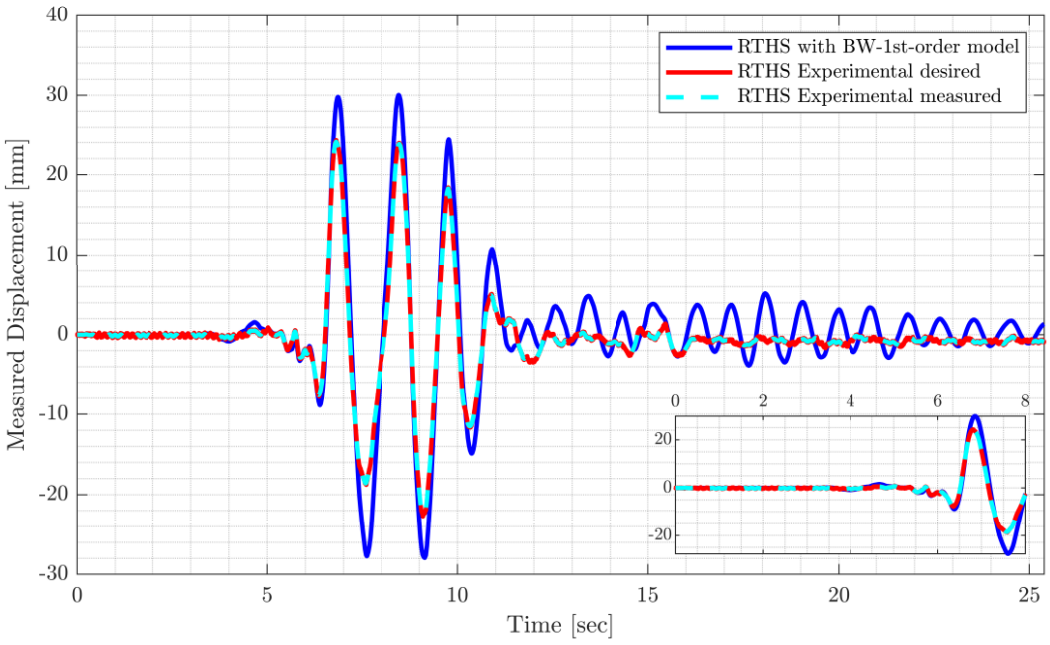

Figure 8.3. Measured base floor displacement comparison against a virtual RTHS with a Bouc-Wen model of 1st order (isolator NPA1).

The oil-column resonance distortion is strongly present in the measured force signal, similar to that seen for the virtual RTHS shown in Figure 6.15. This distortion could affect the response of the numerical substructure since it is part of the feedback signal. Figure 8.2a shows that the frequency content of the experimental displacement sent to the transfer system is contaminated with noise that came from the feedback-restoring force and was not filtered out by the numerical

substructure. Delay compensators such as the PLC or a derivative action from a PID controller can magnify this distortion, causing the sliding table to vibrate close to its resonant frequency, which could be detrimental to the integrity of the experimental setup and the simulation.

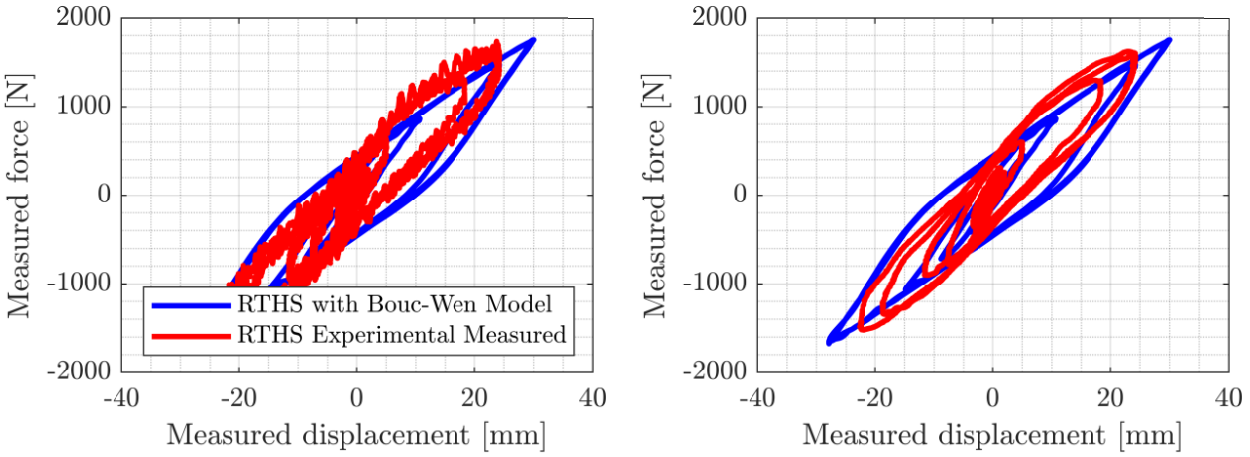

Figure 8.4. Measured shear force comparison with a virtual RTHS with a Bouc-Wen model of 1st order (isolator NPA1). a) unfiltered measured signal (left), filtered measured signal (right).

By applying a low-pass filter with a cutoff frequency of 25 Hz to the force signal, the effect of this distortion is removed and can be better compared with the theoretical response. Figure 8.2b shows the filtered measured force signal. The Bouc-Wen model can capture the force asymmetry and match the group of loops at the beginning of the signal and the loops that branched out upwards for the larger amplitudes.

A series of RTHS were performed to assess the delay compensator performance with an increase in the compensation factor α. Figure 8.5 shows that the base floor displacements of the structure decreased when the compensation factor increased. It is worth noting that the feedback force was amplified 2.5 times for these simulations. That way the response of the system would not surpass the stroke of the actuator.

By plotting the uncompensated signal against the compensated signal, it is better observed that there is a decrease of 54.35% in the maximum measured displacement. The commanded displacements plotted against the measured displacements show the graph to go from a nonlinear to a linear dependency between these signals and the amplitude decrease.

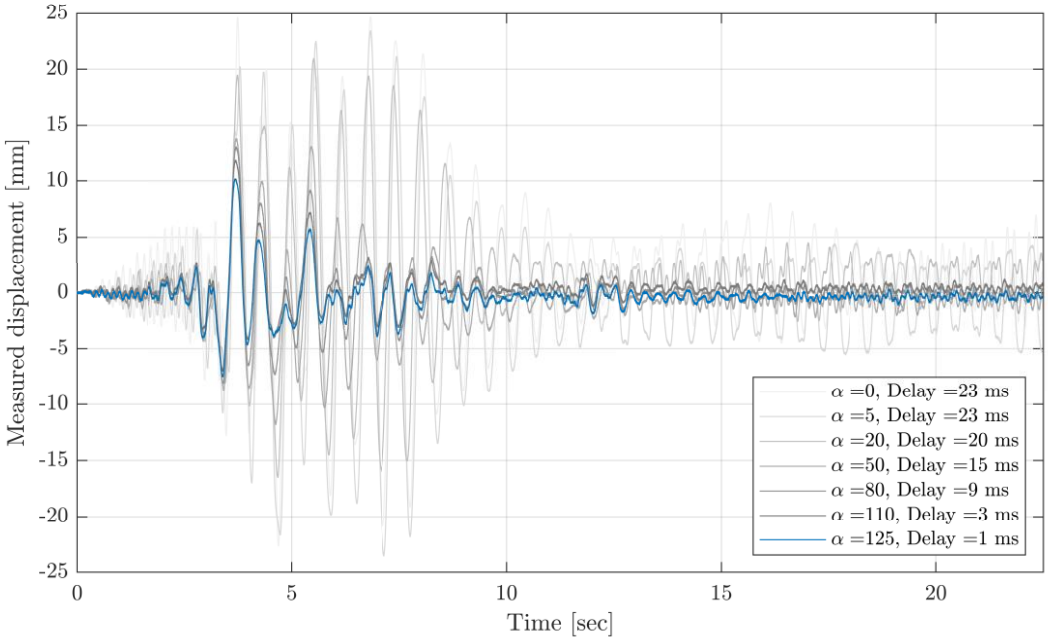

Figure 8.5. Effect of delay compensation in the response of the system.

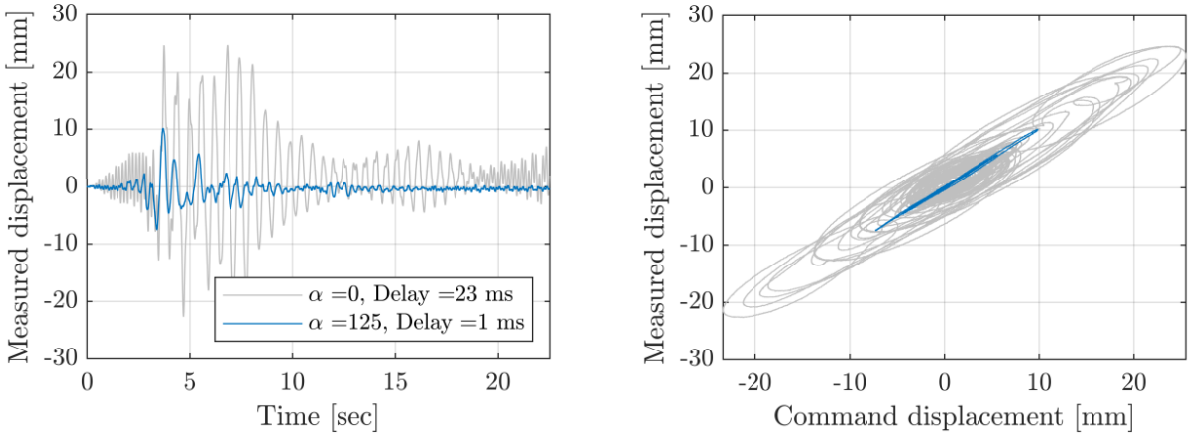

Figure 8.6. Comparison between the compensated signal and the compensated signal. A) time history (left) and b) measured versus command displacement (right).

A closer look at the compensated signal in Figure 8.6b reveals that there are some sections in the graph where there seems to exist a small delay, which can be attributed to the nonlinearities of the physical specimen that introduces a varying delay during the experimental simulation which the inverse compensator cannot compensate. The fitting of a linear function to the compensated

graph reveals that the amplitude tracking by the transfer system is not significantly distorted due to the compensator.

The comparison between the full-scale response, the theoretical 1st order Bouc-Wen of model response, and the RTHS experimental response are shown in Figure 8.7, where the RMSE error is lower for the experimental response than for the theoretical response. The theoretical response, as discussed before, possesses a strong influence from the first mode of the structure which dominates throughout the signal, as it is shown in Figure 8.8 where the most prominent peak corresponds to the first mode, while the full-scale and the RTHS responses present a strong presence of the first and mode during the large displacements of the structure and a small contribution of the second structural model in the last portion of the signal at around 6.8 Hz, as shown in Figure 8.8b. The experimental response simulates the behavior of the full-scale response, especially for small displacements. At large displacements, it underestimates the full-scale response.

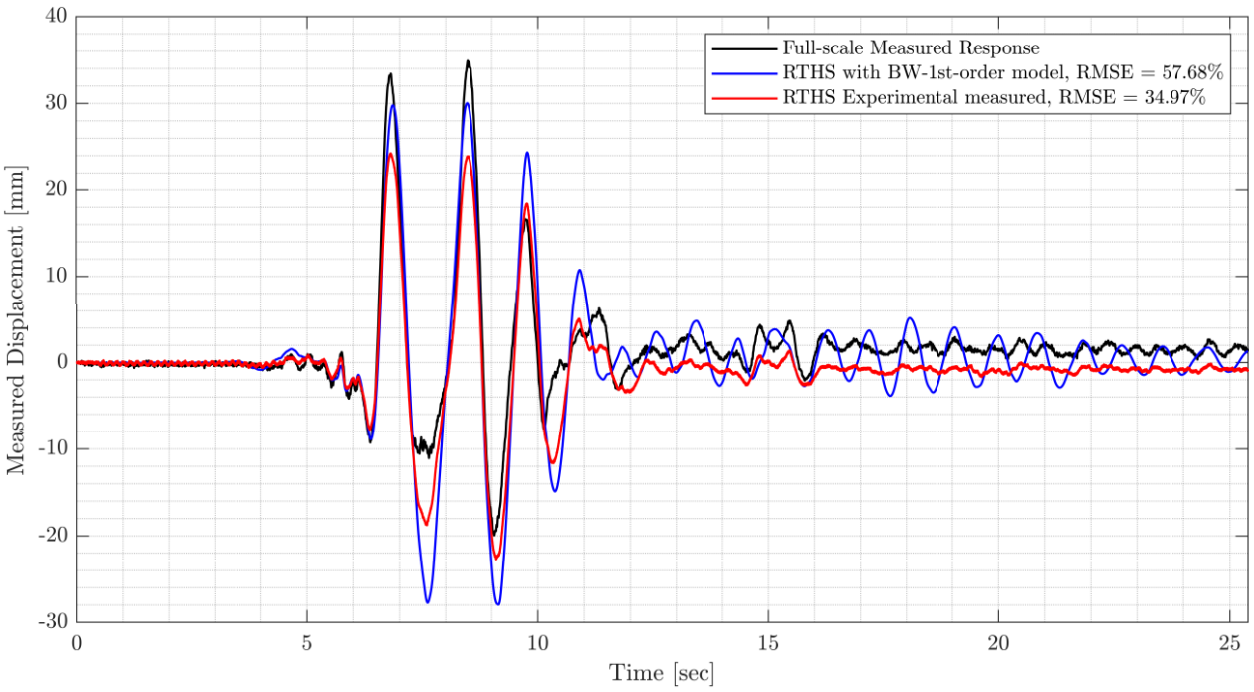

Figure 8.7. Measured base level displacement between the full scale, theoretical response, and experimental responses (isolator NPA1).

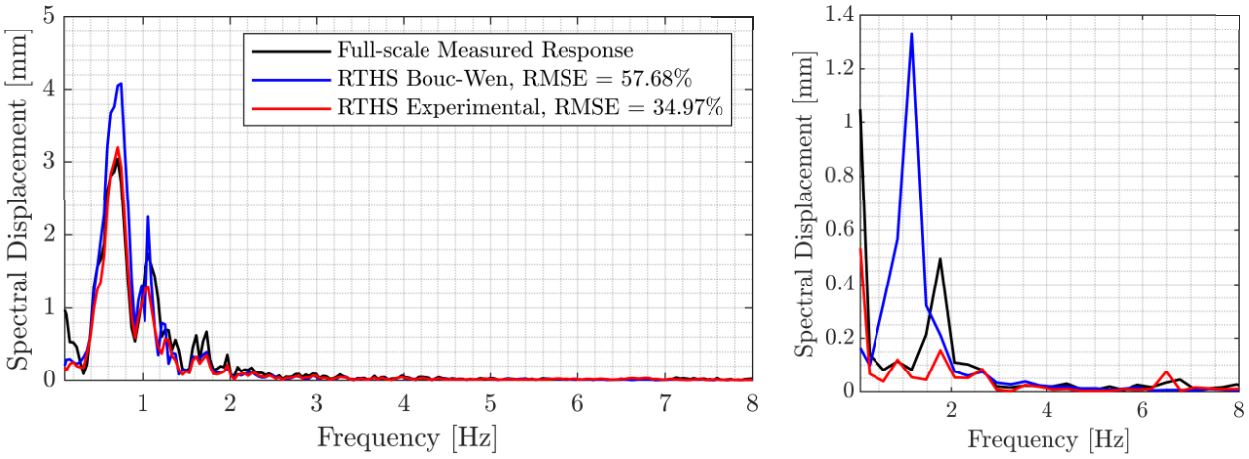

Figure 8.8. Displacement spectra for a) the entire response (left) and b) the last 4 second of the response (right) (isolator NPA1).

9. CONCLUSIONS AND FUTURE WORK

A summary of major findings, contributions, and conclusions from this study are summarized in Sections 9.1 through 9.3, respectively. Recommendations and ideas suggested for future work are presented in Sections 9.4 and 9.5, respectively.

9.1 Summary of major findings

A testing instrument was designed and constructed to apply a uniaxial compressive force up to 22kN and a shear force of 8kN simultaneously to a test specimen. Over 20 different unbonded fiber-reinforced elastomeric isolators have been tested to obtain their effective horizontal stiffness and their effective damping ratio.

Two Bouc-Wen models were implemented to model the behavior of the UFREIs, one model includes a linear relationship with the lateral displacement (stiffness relationship), and the second model includes a fifth-order polynomial relationship. The curve fitting of both models shows that for the shear tests, the fifth-order model better fits the behavior of the UFREI made of natural rubber, polyester, and carbon fiber since it can capture the change in tangent stiffness because of the softening and hardening effects. Isolators made of recycled rubber were found to be stiffer and more porous, making them susceptible to damage during testing. Therefore, they present other nonlinear behaviors which could not be captured accurately by either of the two models; we speculate that this difference in behavior stems from differences in their composition and manufacturing process when compared to the specimens with natural rubber.

A series of tests were performed on the transfer system without a specimen to assess its frequency content and the distortions that it could introduce in the measured signals. For lower frequency ranges, up to 40 Hz, there does not seem to be any mode that can be attributed to the motion of the frame. The major sources of signal distortion, however, were identified as coming from the servo-hydraulic system. Common types of distortions correspond to the amplitude and phase decrease with the frequency that affects the measured displacements by modifying its amplitude and introducing a time delay. Transfer systems have inherent dynamics and delays, thus taking time between the moment the numerical displacement is sent to the transfer system for it to execute this displacement. With a time delay of approximately 25 ms for a 1 Hz signal, the time

delay was the main cause of distortion from the transfer system in the measured displacements for the uncontrolled system.

The next most significant of these distortions corresponds to the oil-column resonance, which occurs when the oil inside the actuator acts as a spring and, along with the sliding table, forms a spring-mass system, the frequency of this system is 71 Hz and is present in the measured displacements accelerations and forces. The next type of distortion corresponds to harmonic peaks found in the Fourier spectra of the measured signals. These distortions can be attributed to the nonlinearities present in the servo-hydraulic system, such as a nonlinear flow-pressure relationship or a flow-gain nonlinearity.

To study the dynamics of the transfer system, a mechanics-based model was developed to understand better the distortions that the sliding table can introduce to the measured signals. The model accounts for the inertial forces generated because of the acceleration of the mass of the plate and dissipative forces, which were modeled as a viscous damping component and a Coulomb friction component associated with the railing system. The model seems to match well for a frequency range up to 15 Hz but fails to model the dissipative forces accurately at higher frequencies since this force does not seem to hold a linear relationship with the velocity at higher frequencies.

9.2 Contributions

A numerical substructure, the transfer system model, and selected Bouc-Wen models were assembled into a virtual model of the RTHS system, which was then used to design a control system that could compensate for the distortions that the dynamics of the transfer system introduced to the measured signals. The control system is comprised of a delay compensator, which computes the predicted displacement as a linear extrapolation between the previous and current desired displacements, and a Proportional-Integral controller, which accounts for the amplitude difference between the measured and the desired displacements.

The virtual model of the RTHS is part of a code package which was created for users interested in learning the applications of RTHS of a base-isolated structure with a nonlinear component as it is a rubber isolator. This package contains the models presented in this work as well as selected experimental data that was collected in the laboratory.

The control system was deployed at the IISL in an RTHS experiment where it presented a good performance at reducing the delay and amplitude differences. However, it increased the effect of the oil-column resonance in the measured signals. The simulation seems to capture the behavior of the isolated structure for small displacements. However, it tends to underestimate the displacement of the full-scale specimen for large displacements.

9.3 Conclusions

The hysteretic response of the UFREIs made of natural rubber and reinforced with either carbon or polyester fibers presents three major types of nonlinearities, namely: softening due to the loss in contact at the start of the deformation, hardening effect due to the increase in contact area because of the rollover of the isolator at large deformations, and asymmetry in the measured force. Isolators made of recycled rubber present wider hysteresis loops because of the loss of integrity of the specimen during the test. This loss of integrity is attributed to their higher rigidity attained from their brittle rubber matrix composition and manufacturing processes which do not allow for the isolator to endure large deformations.

A Bouc-Wen model with a 5th-order polynomial relationship with the lateral displacement can capture the hysteretic behavior of UFREIs made of natural rubber and reinforced with either carbon or polyester fibers. The 3rd and 5th-order terms in the model help to account for the softening and hardening behaviors. The 2nd and 4th-order terms help account for the force asymmetry observed in the hysteretic loops of the UFREIs.

Large transfer systems used to perform large-scale tests are more likely to possess an oil-column resonant frequency in the lower range of frequencies than those designed for high-velocity rates and with lighter masses attached. Proper online filtering procedures must be selected to remove distortions from the measured signals, ensure that the test specimen modal information is preserved, and not introduce any additional delay into the system.

Transfer systems with a delay for low-frequency input signals of about 30 ms could drive the system to develop high displacement that could make the simulation unstable. A good understanding of the stability of the partition for delays in the restoring forces coming from the experimental part is essential to avoid compromising the integrity of the test. Depending on the critical time delay identified in a stability analysis, the time delay could render the system unstable or drive the isolated system to develop amplitudes beyond the capabilities of the transfer system.

For transfer systems that present a low RMSE between the measured and desired displacements (above 90%) and a significant delay (above 25 ms) for a low-frequency range of input signals, a PI controller should suffice for proper amplitude tracking through the frequency range. A delay compensator can effectively decrease the delay in the simulation; however, it can take a toll on the displacement signal amplitude by reducing it if the value of the compensation parameter is overestimated. Thus, a well-tuned delay compensator should be part of the control system that could appropriately predict the displacements in the system without intensifying high-frequency noise.

An RTHS is an efficient, cost-effective, and versatile approach to testing the behavior of a base-isolated structure where the isolation system is comprised of UFREIs. These types of simulations can capture dynamics and rate effects under similar loads that it would experience in a full-scale test that the approximation made by a virtual system with a Bouc-Wen model cannot capture.

In the virtual RTHS the Bouc-Wen with a first-order stiffness parameter seems to approximate the behavior of the isolator in a similar manner than the fifth-order model, which shows that even though the isolator behavior in a shear test presents different nonlinearities, under the RTHS performed, its hysteretic behavior presented fewer variations in the tangent stiffness, thus being able to be simulated by a simpler Bouc-Wen model.

9.4 Recommendations

The Bouc-Wen model with a 5th order relationship is recommended for studying the hysteretic force-displacement relationship of a UFREI made of rubber and carbon and polyester fiber. Special attention needs to be given to the proper preparation of the signals used for the parameter identification so that the nonlinearities in the force response are captured by the model.

It is recommended that the partitioned system be subjected to a stability analysis to assess its stability restrictions and to ensure that it is well-conditioned. The critical time delay is an important parameter to compute from this analysis since it will define whether the system will remain stable or not during the simulation. A from such analysis can be also obtained the maximum mass, damping and stiffness variations that the numerical substructure can resist while remaining stable. Therefore, an optimum combination from these parameters could be obtained and implemented to ensure a stable partition.

A modal analysis is recommended to be carried out for any transfer system that is selected for an RTHS before designing the simulation to identify the causes of distortions that it could introduce to the measured signals and that could have a damaging effect on the transfer system and on the simulation. An analysis of the hysteresis loops is a useful procedure that could give a better understanding of the behavior of the transfer system especially if its variation with frequency is also included in the analysis.

In literature there are multiple types of delay compensators, thus a proper selection of a delay compensator is recommended such that it can adjust well to the other parts of the control system and to the transfer system. Some of these compensators rely on past inputs or measured signal thus they could exacerbate the high-frequency noise that these signals can include.

Before executing an RTHS it is recommended to try different models similar to the isolated system studied here but with small modifications that would make it inherently stable. These modifications should ensure to drive the system to develop displacements and forces with magnitudes that remain within the physical and operational capabilities of the transfer system. These systems can subsequently be modified to transition to the isolated system studied here in an RTHS. This is a slower implementation process, but that can ensure that the integrity of the transfer system will be maintained and provide a good understanding of how changes in the model alters its dynamic behavior.

9.5 Ideas suggested for future work

Regarding the numerical substructure, many other types of configurations can be tested in this RTHS facility, such as adding more stories, or including rotational dynamics or mass eccentricities in the building. Other devices such as MR dampers or actuators could be included in the RTHS along with the isolators to study different type of seismic protection techniques.

A more detailed mechanics model of the transfer system could be designed to account for the nonlinear behavior of the dissipative forces at higher frequencies or to account for uncertainties in the restoring forces coming from the sliding table.

Different methods to model the isolators could be implemented, such as Bouc-Wen models that account for softening, hardening, stiffness degrading, and force asymmetry with different functions aside from the polynomial function presented in this work. Machine learning and deep learning techniques could be applied to model the hysteretic behavior of the isolators learning from

different shear tests or RTHS. Uncertainty identification and quantification could be explored to account for the small differences in behavior of the isolators for the same test.

The transfer system can be modeled by including more complex servo-hydraulics dynamics, thus increasing the order of the plant's transfer function.

Different control techniques could also be implemented to diminish the effect of the oil-column resonance and harmonic distortion, such as active harmonic cancelation or filtering techniques. More complex controllers, such as a Linear-Quadratic Gaussian controller, and adaptive controllers, could be implemented to support other applications; Neural network techniques are another option for a controller, which could be applied to control the RTHS experiment by running multiple simulations in the virtual model of the RTHS before deploying them experimentally. Delay compensators that could account for the nonlinear behavior in the system could be implemented to best suit other types of controllers, such as active delay compensation or polynomial extrapolation techniques.

REFERENCES

Airouche, A., Aknouche, H., Bechtoula, H., Mezouer, N., & Kibboua, A. (2018). Performance of the CGS six DOF Shaking Table on the Harmonic Signal Reproduction. *Periodica Polytechnica Civil Engineering, 62*, 102–111. doi:10.3311/PPci.9033

Al-Anany, Y. M., Moustafa, M. A., & Tait, M. J. (2018). Modeling and Evaluation of a Seismically Isolated Bridge Using Unbonded Fiber-Reinforced Elastomeric Isolators. *Earthquake Spectra, 34*, 145-168. doi:10.1193/072416EQS118M

Al-Azawi, T., Said, A., Almusaui, S., & Al-Zaidee, S. (2017, July). Modeling of Base Isolator as Structural Element. *4*. doi:10.5281/zenodo.836621

Aloisio, A., Alaggio, R., Köhler, J., & Fragiacomo, M. (2020). Extension of Generalized Bouc-Wen Hysteresis Modeling of Wood Joints and Structural Systems. *Journal of Engineering Mechanics, 146*, 04020001. doi:10.1061/(ASCE)EM.1943-7889.0001722

Asai, T., Chang, C.-M., & Spencer, B. F. (2015). Real-Time Hybrid Simulation of a Smart Base-Isolated Building. *Journal of Engineering Mechanics, 141*, 04014128. doi:10.1061/(ASCE)EM.1943-7889.0000844

Calabrese, A., Spizzuoco, M., Serino, G., Della Corte, G., & Maddaloni, G. (2015). Shaking table investigation of a novel, low-cost, base isolation technology using recycled rubber. *Structural Control and Health Monitoring, 22*, 107-122. doi:https://doi.org/10.1002/stc.1663

Carrion, J., Spencer, & Spencer, B. (2007, January). Model-based Strategies for Real-time Hybrid Testing.

Chae, Y., Kazemibidokhti, K., & Ricles, J. M. (2013). Adaptive time series compensator for delay compensation of servo-hydraulic actuator systems for real-time hybrid simulation. *Earthquake Engineering & Structural Dynamics, 42*, 1697-1715. doi:https://doi.org/10.1002/eqe.2294

Chase, J., Hudson, N., Lin, J., Elliot, R., & Aylwin, S. (2005, July). Nonlinear shake table identification and control for near-field earthquake testing. *Journal of Earthquake Engineering - J EARTHQU ENG, 9*, 461-482. doi:10.1080/13632460509350551

Chen, C., & Ricles, J. M. (2008). Development of Direct Integration Algorithms for Structural Dynamics Using Discrete Control Theory. *Journal of Engineering Mechanics, 134*, 676-683. doi:10.1061/(ASCE)0733-9399(2008)134:8(676)

Chen, C., & Ricles, J. M. (2009). Analysis of actuator delay compensation methods for real-time testing. *Engineering Structures, 31*, 2643-2655. doi:https://doi.org/10.1016/j.engstruct.2009.06.012

Chen, P.-C., & Tsai, K.-C. (2013). Dual compensation strategy for real-time hybrid testing. *Earthquake Engineering & Structural Dynamics, 42*, 1-23. doi:https://doi.org/10.1002/eqe.2189

Chen, P.-C., Dong, M.-W., Chen, P.-C., & Nakata, N. (2020). Stability Analysis and Verification of Real-Time Hybrid Simulation Using a Shake Table for Building Mass Damper Systems. *Frontiers in Built Environment, 6*. doi:10.3389/fbuil.2020.00109

Chen, Y., & Ahmadi, G. (1992). Wind Effects on Base-Isolated Structures. *Journal of Engineering Mechanics, 118*, 1708-1727. doi:10.1061/(ASCE)0733-9399(1992)118:8(1708)

Cheng, F. Y. (2008). *Smart structures: innovative systems for seismic response control.* CRC press.

Conte, J. P., & Trombetti, T. L. (2000). Linear dynamic modeling of a uni-axial servo-hydraulic shaking table system. *Earthquake Engineering & Structural Dynamics, 29*, 1375-1404. doi:https://doi.org/10.1002/1096-9845(200009)29:9<1375::AID-EQE975>3.0.CO;2-3

De Silva, C. W. (2015). *Sensors and Actuators: Engineering System Instrumentation, Second Edition.* CRC Press. Retrieved from https://books.google.com/books?id=ukZOCgAAQBAJ

Dyke, S. J., Spencer, B. F., Quast, P., & Sain, M. K. (1995). Role of Control-Structure Interaction in Protective System Design. *Journal of Engineering Mechanics, 121*, 322-338. doi:10.1061/(ASCE)0733-9399(1995)121:2(322)

Eem, S. H., Jung, H. J., & Koo, J. H. (2013, March). Seismic performance evaluation of an MR elastomer-based smart base isolation system using real-time hybrid simulation. *Smart Materials and Structures, 22*, 055003. doi:10.1088/0964-1726/22/5/055003

Erlicher, S., & Bursi, O. (2009, February). Bouc–Wen-Type Models with Stiffness Degradation: Thermodynamic Analysis and Applications. *Journal of Engineering Mechanics, 134*. doi:10.1061/(ASCE)0733-9399(2008)134:10(843)

Gan, J., & Zhang, X. (2019). Nonlinear Hysteresis Modeling of Piezoelectric Actuators Using a Generalized Bouc–Wen Model. *Micromachines, 10*. doi:10.3390/mi10030183

Habieb, A. B., Milani, G., Tavio, T., & Milani, F. (2017). Numerical Model of Low Cost Rubber Isolators for Masonry Housing in High Seismic Regions. *International Journal of Civil and Environmental Engineering, 11*(5), 664-670. doi:doi.org/10.5281/zenodo.1130579

Han, Q., Dong, H., Du, X.-l., Sun, D., & Huang, C. (2014). Hysteresis behavior of reinforced concrete bridge piers considering strength and stiffness degradation and pinching effect. *Journal of Vibroengineering, 16*, 1151-1161.

Horiuchi, T., Inoue, M., & Konno, T. (2000). Development of a real - time hybrid experimental system using a shaking table.

Horiuchi, T., Inoue, M., Konno, T., & Namita, Y. (1999). Real-time hybrid experimental system with actuator delay compensation and its application to a piping system with energy absorber. *Earthquake Engineering & Structural Dynamics, 28*, 1121-1141. doi:https://doi.org/10.1002/(SICI)1096-9845(199910)28:10<1121::AID-EQE858>3.0.CO;2-O

Huang, L., Guo, T., Chen, C., & Chen, M. (2018, October 01). Restoring force correction based on online discrete tangent stiffness estimation method for real-time hybrid simulation. *Earthquake Engineering and Engineering Vibration, 17*, 805-820. doi:10.1007/s11803-018-0477-2

Ikhouane, F., & Rodellar, J. (2007, September). Systems with Hysteresis: Analysis, Identification and Control Using the Bouc-Wen Model. *Systems with Hysteresis: Analysis, Identification and Control using the Bouc-Wen Model*. doi:10.1002/9780470513200

Kusner, D. A., Rood, J. D., & Burton, G. W. (1992). Signal reproduction fidelity of servohydraulic testing equipment. *Proc., 10th World Conf. on Earthquake Engineering*, (pp. 2683–2688).

Losanno, D., Sierra, I. E., Spizzuoco, M., Marulanda, J., & Thomson, P. (2019). Experimental assessment and analytical modeling of novel fiber-reinforced isolators in unbounded configuration. *Composite Structures, 212*, 66-82. doi:https://doi.org/10.1016/j.compstruct.2019.01.026

Losanno, D., Sierra, I. E., Spizzuoco, M., Marulanda, J., & Thomson, P. (2020). Experimental performance of unbonded polyester and carbon fiber reinforced elastomeric isolators under bidirectional seismic excitation. *Engineering Structures, 209*, 110003. doi:https://doi.org/10.1016/j.engstruct.2019.110003

Luco, J. E., Ozcelik, O., & Conte, J. P. (2010). Acceleration Tracking Performance of the UCSD-NEES Shake Table. *Journal of Structural Engineering, 136*, 481-490. doi:10.1061/(ASCE)ST.1943-541X.0000137

Maghareh, A., Dyke, S., Rabieniaharatbar, S., & Prakash, A. (2017). Predictive stability indicator: a novel approach to configuring a real-time hybrid simulation. *Earthquake Engineering & Structural Dynamics, 46*, 95-116. doi:https://doi.org/10.1002/eqe.2775

Maghareh, A., Silva, C. E., & Dyke, S. J. (2018). Parametric model of servo-hydraulic actuator coupled with a nonlinear system: Experimental validation. *Mechanical Systems and Signal Processing, 104*, 663-672. doi:https://doi.org/10.1016/j.ymssp.2017.11.009

Maghareh, A., Silva, C. E., & Dyke, S. J. (2018). Servo-hydraulic actuator in controllable canonical form: Identification and experimental validation. *Mechanical Systems and Signal Processing, 100*, 398-414. doi:https://doi.org/10.1016/j.ymssp.2017.07.022

Magliulo, G., Petrone, C., Capozzi, V., Maddaloni, G., Lopez, P., Talamonti, R., & Manfredi, G. (2012, October). Shake Table Tests on Infill Plasterboard Partitions. *The Open Construction and Building Technology Journal, 6*, 155-163. doi:10.2174/1874836801206010155

Manzoori, A., & Toopchi-Nezhad, H. (2017). Application of an Extended Bouc-Wen Model in Seismic Response Prediction of Unbonded Fiber-Reinforced Isolators. *Journal of Earthquake Engineering, 21*, 87-104. doi:10.1080/13632469.2016.1138166

Merritt, H. E. (1991). *Hydraulic Control Systems.* Wiley. Retrieved from https://books.google.com/books?id=Imu-v-6lzwYC

Mitu, A.-M., Sireteanu, T., & Daniel, B. (2010, January). On the Efficiency of a Base Isolation System. *Analele Universităţii Eftimie Murgu Reşiţa. Fascicula de Inginerie, XVII*.

Nilvetti, F., Pappalardo, C., & Guida, D. (2012, January). Mass, Stiffness and Damping Identification of a Two-Story Building Model. *1*, 19-35.

Ou, G., Ozdagli, A. I., Dyke, S. J., & Wu, B. (2015). Robust integrated actuator control: experimental verification and real-time hybrid-simulation implementation. *Earthquake Engineering & Structural Dynamics, 44*, 441-460. doi:https://doi.org/10.1002/eqe.2479

Ou, G., Yang, G., Dyke, S., & Wu, B. (2020). Investigation of Hybrid Simulation With Model Updating Compared to an Experimental Shake Table Test. *Frontiers in Built Environment, 6*. doi:10.3389/fbuil.2020.00103

Ozcelik , O. (2008). A Mechanics-based Virtual Model of NEES-UCSD Shake Table: Theoretical Development and Experimental Validation. San Diego, California, United States of America: University of California San Diego.

Ozcelik, O., Conte, J. P., & Luco, J. E. (2021). Comprehensive mechanics-based virtual model of NHERI@UCSD shake table—Uniaxial configuration and bare table condition. *Earthquake Engineering & Structural Dynamics, 50*, 3288-3310. doi:https://doi.org/10.1002/eqe.3510

Pelliciari, M., Marano, G. C., Cuoghi, T., Briseghella, B., Lavorato, D., & Tarantino, A. M. (2018). Parameter identification of degrading and pinched hysteretic systems using a modified Bouc–Wen model. *Structure and Infrastructure Engineering, 14*, 1573-1585. doi:10.1080/15732479.2018.1469652

Qian, Y., Ou, G., Maghareh, A., & Dyke, S. J. (2014). Parametric identification of a servo-hydraulic actuator for real-time hybrid simulation. *Mechanical Systems and Signal Processing, 48*, 260-273. doi:https://doi.org/10.1016/j.ymssp.2014.03.001

Rabiee, R., & Chae, Y. (2022). Real-time hybrid simulation for a base-isolated building with the transmissibility-based semi-active controller. *Journal of Intelligent Material Systems and Structures, 33*, 2228-2240. doi:10.1177/1045389X221079680

Scheaua, F. (2020, September). Improvement of structures seismic response based on pendulum systems with double sliding surface. *IOP Conference Series: Materials Science and Engineering, 916*, 012102. doi:10.1088/1757-899X/916/1/012102

Schellenberg, A. H., Becker, T. C., & Mahin, S. A. (2017). Hybrid shake table testing method: Theory, implementation and application to midlevel isolation. *Structural Control and Health Monitoring, 24*, e1915. doi:https://doi.org/10.1002/stc.1915

Silva, C. E., Gomez, D., Maghareh, A., Dyke, S. J., & Spencer, B. F. (2020). Benchmark control problem for real-time hybrid simulation. *Mechanical Systems and Signal Processing, 135*, 106381. doi:https://doi.org/10.1016/j.ymssp.2019.106381

Toopchi-Nezhad, H., Tait, M. J., & Drysdale, R. G. (2009). Simplified analysis of a low-rise building seismically isolated with stable unbonded fiber reinforced elastomeric isolators. *Canadian Journal of Civil Engineering, 36*, 1182-1194. doi:10.1139/L09-056

Wang, Q., Wang, J., Jin, F., Chi, F.-D., & Zhang, C.-H. (2011, December). Soil-structure interaction analysis by real-time dynamic hybrid testing. *Soil Dynamics and Earthquake Engineering - SOIL DYNAM EARTHQUAKE ENG, 31*, 1690-1702. doi:10.1016/j.soildyn.2011.07.004

Warn, G. P., & Ryan, K. L. (2012). A Review of Seismic Isolation for Buildings: Historical Development and Research Needs. *Buildings, 2*, 300–325. doi:10.3390/buildings2030300

Wei, Z. (2009, June). Reducing Harmonic Distortion on Vibrators at Low Frequencies - Servo-valve Flow Linearization. doi:10.3997/2214-4609.201400272

Xu, G., Wang, Z., Bao, Y., Yang, G., & Wu, B. (2020). Shaking Table Substructure Testing Based on Three-Variable Control Method with Velocity Positive Feedback. *Applied Sciences, 10*. doi:10.3390/app10165414

Yao, J.-J., Hu, S.-H., Fu, W., & Han, J.-W. (2011). Impact of excitation signal upon the acceleration harmonic distortion of an electro-hydraulic shaking table. *Journal of Vibration and Control, 17*, 1106-1111. doi:10.1177/1077546310366579

Zhang, R., Phillips, B. M., Taniguchi, S., Ikenaga, M., & Ikago, K. (2017). Shake table real-time hybrid simulation techniques for the performance evaluation of buildings with inter-story isolation. *Structural Control and Health Monitoring, 24*, e1971. doi:https://doi.org/10.1002/stc.1971

Zhang, Z., Tian, X., & Ge, X. (2021). Dynamic Characteristics of the Bouc–Wen Nonlinear Isolation System. *Applied Sciences, 11*. doi:10.3390/app11136106